Novel gold intermetallics with unique properties and bonding patterns

by

Christopher Ranger Celania

A dissertation submitted to the graduate faculty

in partial fulfillment of the requirements for the degree of

DOCTOR OF PHILOSOPHY

Major: Materials Science and Engineering

Program of Study Committee:
Gordon Miller, Co-Major Professor
Vitalij Pecharsky, Co-Major Professor
Alan Russell
Scott Chumbley
Gerd Meyer

The student author, whose presentation of the scholarship herein was approved by the program of study committee, is solely responsible for the content of this dissertation. The Graduate College will ensure this dissertation is globally accessible and will not permit alterations after a degree is conferred.

Iowa State University

Ames, Iowa

2017

TABLE OF CONTENTS

Page

NOMENCLATURE iv

ACKNOWLEDGMENTS v

ABSTRACT..... vi

CHAPTER 1 GENERAL INTRODUCTION..... 1

Dissertation Organization 1
Motivation and Background 1
Experimental Procedures 3

CHAPTER 2 R_3Au_9Pn (R = Y, Gd-Ho; Pn = Sb, Bi): A LINK BETWEEN $Cu_{10}Sn_3$ AND $Gd_{14}Ag_{51}$..... 8

Abstract 9
Introduction..... 9
Experimental Section..... 11
Results and Discussion 16
Summary..... 24
Tables and Figures..... 26
Additional Information 34
References..... 36

CHAPTER 3 CRYSTAL STRUCTURES AND NEW PERSPECTIVES ON Y_3Au_4 AND $Y_{14}Au_{51}$ 41

Abstract 41
Introduction..... 42
Experimental Procedure..... 43
Results and Discussion 44
Tables and Figures..... 48
Additional Information 52
References..... 53

CHAPTER 4 R_{14}(Au, M)$_{51}$ (R = Y, La-Nd, Sm-Tb, Ho, Er, Yb, Lu; M = Al, Ga, Ge, In, Sn, Sb, Bi): STABILITY RANGES AND SITE PREFERENCE IN THE $Gd_{14}Ag_{51}$ STRUCTURE TYPE 54

Abstract 54
Introduction 55
Experimental Section 57
Results and Discussion 60
Summary 65
Tables and Figures 67
Additional Information 73
References 75

CHAPTER 5 BRINGING ORDER TO LARGE SCALE DISORDERED COMPLEX METAL ALLOYS: Gd_2(Au, Sb)$_{15}$ AND Ba(Au, Ga)$_{12}$ 78

Abstract 78
Introduction 79
Experimental Section 81
Results and Discussion 83
Summary 89
Tables and Figures 91
Additional Information 98
References 100

CHAPTER 6 GENERAL CONCLUSION 103

Conclusion 103
Proposed Future Work 104

REFERENCES 107

APPENDIX: SUPPLEMENTARY TABLES AND FIGURES 110

NOMENCLATURE

REEs	Rare Earth Elements
PXRD	Powder X-Ray Diffraction
DTA	Differential Thermal Analysis
OM	Optical Microscope
SEM	Scanning Electron Microscope
EDS	Energy Dispersive X-ray Spectroscopy
TB-LMTO	Tight-Binding Linear-Muffin-Tin-Orbital
ASA	Atomic Sphere Approximations
WS	Wigner-Seitz Spheres
ES	Empty Spheres
TG-DTA	Thermo-Gravimetric, Differential Thermal Analysis
DSC	Differential Scanning Calorimetry
DC	Direct Current
MPMS	Magnetic Property Measurement System
SQUID	Superconducting Quantum Interference Device
FC	Field Cooled
ZFC	Zero Field Cooled
AFM	Antiferromagnetic
COHP	Crystal Orbital Hamilton Population
DOS	Density of States

ACKNOWLEDGMENTS

I would like to give thanks and my utmost respect to my co-major professors, Dr. Vitalij Pecharsky, and Dr. Gordon Miller, as well as my other committee members, Dr. Alan Russell, Dr. Scott Chumbley, and Dr. Gerd Meyer, for their leadership and support throughout this research. I cannot continue without also thanking Dr. Anja-Verena Mudring for her inspiration, support, and all of the opportunities she has provided by believing in me.

Additionally, I would also like to thank my colleagues, the department faculty and staff for making my time at Iowa State University a wonderful experience. I have had longer than most to take in all that Iowa State has to offer, and those relationships were critical in making the very positive choice to stay. I would also like to thank my friends and family who have helped maintain my sanity through a constant stream of support, and often coffee. Without their assistance, I would not have been able to complete this work.

ABSTRACT

Gold has drawn the fascination of society through its brilliant color, malleability, and chemical resistance (hence its chemical nobility) since its discovery in ancient times. Today, this material is still highly coveted by consumers, but also for research within the scientific realm. The inclusion of gold in intermetallics often leads to notably unique structural and bonding features due to the pronounced relativistic effects on its 5*d* and 6*s* orbitals. Examples include quasicrystals and their approximants, unique gold clusters such as isolated Au_7 clusters in $A_4Au_7X_2$ (*A* = K, Rb, Cs; *X* = Ge, Sn), one dimensional columns such as Au zig-zag chains through Ca_3Au_3In, two dimensional slabs, such as in K_2Au_3, as well as three dimensional gold networks as observed in the interconnected trigonal bipyramids in KAu_5, hexagonal diamond-like frameworks of Au tetrahedra in Au-rich Sr-Au-Al systems; and combinations of tetrahedral and fourfold planar Au atoms in Rb_3Au_7.

In recent years, compounds in the gold-rich region of the *R*-Au-*M* system (*R* = rare earth, *M* = groups 13-15) have come under increased study. Many compounds within this system produce varied electronic and magnetic properties such as Pauli paramagnetism, superconductivity, thermoelectricity, etc. The shielded 4*f* electrons of the added rare earth elements provide the unpaired spins that lead to the wealth of interesting magnetic properties in their compounds. Metals and metalloids from groups 13-15 may then be used as a bank of available options useful in tuning the valence electron count of the *R*-Au system toward the formation of stable compounds.

Exploration of the Gd-Au-Sb system by utilizing common solid state synthesis techniques frequently used for the production of intermetallics (such as arc melting and high-

temperature furnaces for self-flux reactions with low melting components) has yielded rich outcomes. These results include the discovery of a new R_3Au_9Pn series of compounds (R = Y, Gd-Ho; Pn = Sb, Bi), which undergo interesting metamagnetic transitions, varied coloring schemes for Sb substitutions in the known $R_{14}Au_{51}$ compound forming R_{14}(Au, M)$_{51}$ (R = Y, La-Nd, Sm-Tb, Ho, Er, Yb, Lu; M = Al, Ga, Ge, In, Sn, Sb, Bi), and a complex tetragonal Gd-Au-Sb structure with significant Sb site mixing and positional disorder, as well as preliminary structure results of several other previously unreported compounds within the R-Au-M family.

CHAPTER 1

GENERAL INTRODUCTION

Dissertation Organization

This dissertation acts as a culmination of works, aimed at scientific publication. As such, each following chapter is treated as its own manuscript, in line with requirements by the Iowa State University Graduate College. Chapters 2-5 will each contain individualized sections (Introduction, Experimental Procedures, etc.) including reference lists by chapter. Each chapter concludes with a list of tables and images, while supplemental figures and tables are located in a combined Appendix at the end of the dissertation. Crystallographic information files (.cif) that have been uploaded to the International Crystal Structure Database are freely accessible and are excluded from the dissertation to avoid excess length. Instead, accession codes are provided for each uploaded structure at the end of each chapter. Published manuscripts are denoted with the article's location and journal information below the title. Manuscripts that have been submitted to journals and are in the revision process are described similarly. Unpublished work to be completed in the future, as well as a general proposed direction for continued research are located in Chapter 6 as an overarching conclusion to the dissertation. Despite more targeted background sections within Chapters 2-5, an all-encompassing introduction will follow. This includes a generalized view of the synthesis and characterization strategies used for the compounds within this dissertation.

Motivation and Background

Rare earth and gold intermetallic compounds such as those within the *R*-Au-*M* family (*R* = rare earth, *M* = groups 13-15) have attracted substantial attention in the last few years, with attention moving toward the previously under-explored gold-rich regions of the system[1-6]. Many compounds

within this family produce varied electronic and magnetic properties such as Pauli paramagnetism, superconductivity, thermoelectricity, etc. as well as interesting or uncommon structural motifs.

The well-studied relativistic effects on gold's *5d* and 6*s* orbitals often produce notably unique structural and bonding features, which make it an advantageous addition to the search for new or fascinating intermetallic compounds[7-13]. Examples of gold's versatility in structure and bonding are extensive, but include: quasicrystals and their approximants[14-16], unique gold clusters such as isolated Au_7 clusters in $A_4Au_7X_2$ (A = K, Rb, Cs; X = Ge, Sn)[17, 18], one dimensional columns such as Au zig-zag chains through Ca_3Au_3In[19], two dimensional slabs, such as in K_2Au_3[20], as well as three dimensional gold networks as observed in the interconnected trigonal bipyramids in KAu_5,[21] hexagonal diamond-like frameworks of Au tetrahedra in Au-rich Sr-Au-Al systems[22]; and combinations of tetrahedral and fourfold planar coordinated Au atoms in Rb_3Au_7[23].

The shielded 4*f* electrons of the rare earth elements provide the unpaired spins essential to offer a wealth of interesting magnetic properties in their compounds. The varying magnetic moments and atomic sizes moving across the lanthanides also allow for fascinating alteration and comparison of properties and structures within a series of compounds with the same composition but different rare earth elements. Metals and metalloids from groups 13-15 may furthermore allow tuning the valence electron count of the *R*-Au system towards the formation of stable compounds with unprecedented properties. Those anions with similar radii to gold (Sn, Sb, etc.) may also allow for significant site mixing with gold.

Within the *R*-Au-*M* family, only few compounds have been discovered with atomic percent of gold over 50%, making this section particularly interesting for further exploration. Of these compounds, most recent research has focused on ternary compounds with tin and has led to the discovery of the $R_3Au_7Sn_3$ series of compounds. Their structure can be described as a superstructural polyhedral packing of the ZrBeSi-type featuring a new homoatomic Au cluster, $Au@Au_6$[2, 6]. However, gold rich systems in combination with rare earth elements and group 15

elements are largely underexplored. The high content of gold allows for more opportunities to explore the variety of Au-Au bonding as well as the capability of group 15 elements to stabilize the structures or clusters built up of it by adjusting the valence electron count.

There is only one known *R*-Au-*M* structure with group 15 elements where gold is the majority component, $R(Au_{\sim 0.75}Sb_{\sim 0.25})_2$ (*R* = La, Ce, Pr)[24]. Its structure can be related to the UHg_2 structure type, which belongs to the large AlB_2 family of structures. This set of compounds was reported to show statistical mixing of the gold and antimony, which does not appear to exist in the compounds communicated in Chapter 2 (and obviously the binary compounds of Chapter 3), but is largely present in the compounds described in Chapters 4 and 5. Although the focus of this dissertation is clearly on R-Au-M ternary intermetallic compounds, the work has also led to better understanding of binary Y-Au structures (Chapter 3), as well as a complex, disordered alkaline earth metal gold intermetallic in the Ba-Au-Ga family (Chapter 5).

Experimental Procedures

1. Synthesis

Starting materials (Au, 99.98%; rare earth elements (REEs), 99.9%; and Group 13-15 metals, 99.99% and greater) used for synthesis were obtained from the Materials Preparation Center, U.S. DOE Ames Laboratory, except for antimony, which was purchased from Alfa Aesar (99.99% pure). Early exploration began in the Gd-Au-Sb system in a sample loaded with a Gd:Au:Sb, 2:5:1 ratio that was reacted in a sealed tantalum ampule jacketed in fused silica, followed by an anneal. Different synthetic conditions were then tested to replicate results, form the structures as phase-pure samples, or test for formation of a structure with other rare earth elements or group 13-15 elements. The general strategy focused on a high-temperature reaction of starting materials (either by induction heating until at least one component reached liquid state,

acting as a flux; or arc melting), followed by lower temperature anneal to form higher quality single crystals for X-ray structure analysis.

All samples were handled under inert conditions using standard techniques. Sample sizes were typically 0.5g in total. Special care was taken with arc melted samples to avoid loss of the group 13-15 elements due to the low melting points and high vapor pressures of some individuals. In these cases an excess of ~6% mass of the group 13-15 elements was added to arc melted sample starting compositions to account for loss during sample preparation. The starting materials (in the form of filings or small chunks) were then pressed into a pellet with group 13-15 element pieces placed on one side, which was positioned away from direct contact with the arc. The samples were arc melted under an inert Ar environment for short periods (~5 seconds or until the surface appeared fully molten) and flipped four times between separate melting processes to encourage a homogeneity. Following arc melting, the samples were sealed into tantalum tubes under inert argon atmosphere by arc welding. The ampules were then enclosed under vacuum in fused silica tubes, which were set in tube furnaces for annealing.

For reaction in high-temperature furnaces, the stoichiometric amounts of rare earth elements, gold and group 13-15 metals to give the desired compound composition were sealed in tantalum tubes, which were jacketed by fused silica casings before high-temperature reaction and anneal in a tube furnace. Most reactions took place at 1050°C over a few hours, followed by an anneal at 800-850°C for a few days, up to two weeks. The goal of most self-flux reactions is to create a low melting, molten, component to begin the reaction with higher melting temperature components such as the rare earth elements. It may be noted that the reaction temperatures listed above are well beyond the melting point for most of the group 13-15 elements tested. Preliminary testing with Sb samples (melting point 630.6°C) showed that reactions at 850°C (just under the melting point of Au) were not adequate to combine the components. Therefore, the temperature

was raised to ensure that the main component, gold, was molten as well. However, molten gold at these high temperatures becomes reactive with the tantalum ampules, which, at times, resulted in sample mass loss and difficulty in replicating results. Samples typically appeared dark gray with a metallic luster, and displayed stability in air for weeks once removed from their various crucibles.

2. X-Ray Structure Analysis.

Samples were examined with powder X-ray diffraction (PXRD) for determination of phase composition and to assess phase purity on a STOE STADI P diffractometer (STOE image plate, Cu $K_{\alpha 1}$; λ = 1.54059 Å)[25] or in some cases a Guinier X-ray camera detector (graphite monochromated Cu $K_{\alpha 1}$ radiation; Si as an internal standard, a = 5.4308(1) Å)[25]. Samples for X-ray powder diffractometry were sieved to 38μm particles and dispersed onto vacuum grease between Mylar© sheets and set between Al rings. Data were analyzed using the *WinXPow 3.06*[25] and *LAZY PULVERIX* software packages.

The microstructural and homogeneity samples were characterized by optical and scanning electron microscopies (OM and SEM), the latter equipped with electron microprobe (Energy Dispersive X-ray analysis, EDS) for semi-quantitative elemental analysis. A Leica Cambridge 360 microscope, equipped with an Oxford X-Max 20 analyzer was used with Oxford Aztec software, utilizing an extra high tension voltage of 20.0 kV and probe current 220 pA. EDS analyses were performed on at least three sample-points (or areas) to identify the phase composition (counting time of 60 sec). While the majority of SEM/EDS work was completed on the Leica instrument, some supplemental analysis was completed with a JEOL JSM 6060LV (20.0 kV and counting time of 160 sec). EDS data from either instrument approximated atomic percentages for comparison and corroboration with single crystal refinement data.

Single crystals were selected from crushed bulk samples and affixed to glass fibers with grease. They were then tested at room temperature on a Bruker APEX CCD diffractometer or a

Bruker D8 VENTURE diffractometer (both with Mo K_α radiation; λ = 0.71073 Å) utilizing the APEX 2 and APEX 3 software suites respectively for data collection, integration, polarization, and empirical absorption correction[27, 28]. Scans typically covered the 2θ range of ~5-63°. The XPREP algorithms in the SHELXTL suite were used to check the intensity data sets for extinction conditions and E2-1 statistics necessary allowing for the assignment of the proper space group. Direct methods were used for structure solution (SHELXS-97)[29]. Structure refinement (refined atomic position, mixed side occupancy and anisotropic displacement parameters) was carried out with SHELXTL[29].

3. Physical Property Measurements.

Differential thermal analysis (DTA) was performed on a portion of 0.7-0.9 g of some samples, either in the as-cast or annealed form in order to determine future reaction and annealing temperatures. Each sample was enclosed in an out-gassed Mo crucible under Ar flux and transferred to the DTA equipment (Netzsch 404 thermal analyzer). Ta crucibles were not used because of the higher temperatures encountered (up to 1180°C), in which Au often reacts with Ta. Thermal cycles were carried out with rates of 20°C/min on heating and 10°C/min, or 5°C/min on cooling, and under a pure Ar atmosphere. The accuracy in the temperature measurements was ± 5°C.

DC magnetic data for the phase-pure samples was collected in a Quantum Design MPMS (Magnetic Property Measurement System) SQUID (Superconducting Quantum Interference Device) magnetometer. Powder of ~20mg was placed in a fused silica sample holder that was made gastight using Teflon tape followed by the lid and attachment for loading into the system. Samples typically were first tested in a DC field of 1 kOe over a temperature range of 2-250 or 300 K in order to determine critical temperature locations. Isothermal magnetization measurement would then follow at low temperatures (often 2 K) with fields up to 7 T to locate any metamagnetic

transitions at this temperature. If necessary, further testing against temperature at higher, set DC values targeted the metamagnetic transitions.

CHAPTER 2

R_3Au_9Pn (R = Y, Gd-Ho; Pn = Sb, Bi): A LINK BETWEEN $Cu_{10}Sn_3$ AND $Gd_{14}Ag_{51}$

Inorganic Chemistry
DOI: 10.1021/acs.inorgchem.7b00898
Volume: 56 Issue: 12 Pages: 7247-7256
Published: JUN 19 2017

Chris Celania, [†,‡] Volodymyr Smetana, [†,‡] Alessia Provino, [†,§,⊥] Vitalij Pecharsky,[†,‡] Pietro Manfrinetti, [†,§,⊥] Anja-Verena Mudring [†,‡*]

[†]*The Ames Laboratory, U.S. Department of Energy, Iowa State University, Ames, IA 50011, USA*

[‡]*Department of Materials Science and Engineering, Iowa State University, Ames, IA 50011, USA*

[§]*Department of Chemistry, University of Genova, Via Dodecaneso 31, 16146 Genova, Italy*

[⊥]*Institute SPIN-CNR, Corso Perrone 24, 16152 Genova, Italy*

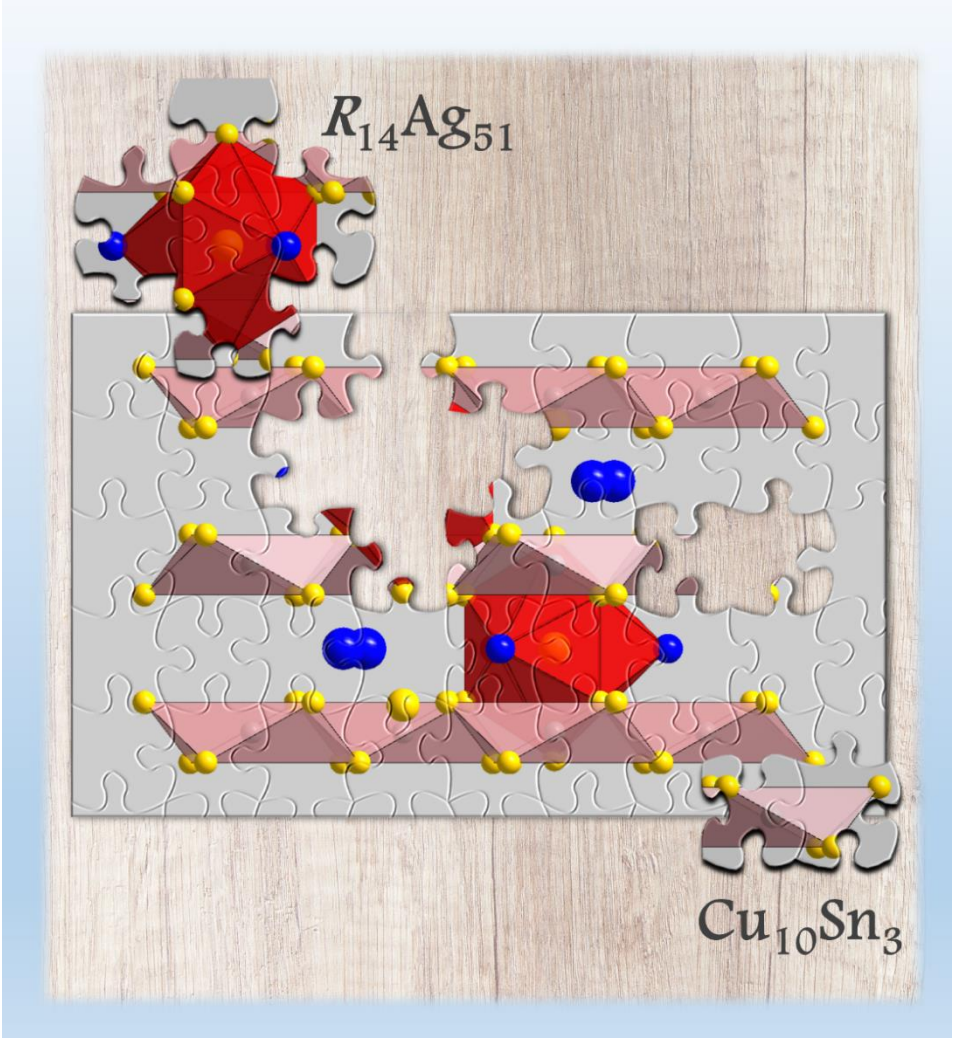

Chapter 2 Cover Image

Abstract

A new series of intermetallic compounds R_3Au_9Pn (R = Y, Gd-Ho; Pn = Sb, Bi) has been discovered during the explorations of the Au-rich parts of rare earth containing ternary systems with *p*-block elements. The existence of the series is strongly restricted by both geometric and electronic factors. R_3Au_9Pn crystallize in the hexagonal crystal system with space group $P6_3/m$ (a = 8.08–8.24 Å, c = 8.98–9.08 Å). All compounds feature Au-*Pn*, formally anionic, networks built up by layers of alternating edge-sharing Au@Au_6 and Sb@Au_6 trigonal antiprisms of overall composition $Au_{6/2}Pn$ connected through additional Au atoms and separated by a triangular cationic substructure formed by R atoms. From a first look, the series appears to be isostructural to recently reported $R_3Au_7Sn_3$ (a ternary ordered derivative of the $Cu_{10}Sn_3$-structure type), but no example of R_3Au_9M is known when M is a triel or tetrel element. R_3Au_9Pn also contains Au@$Au_6Au_2R_3$ fully capped trigonal prisms, which are found to be isostructural to those found in the well-researched $R_{14}Au_{51}$ series. This structural motif, not present in $R_3Au_7Sn_3$, represents a previously unrecognized link between $Cu_{10}Sn_3$ and $Gd_{14}Ag_{51}$ parent structure types. Magnetic property measurements carried out for Ho_3Au_9Sb reveal a complex magnetic structure characterized by antiferromagnetic interactions at low temperature (T_N = 10 K). Two metamagnetic transitions occur at high field with a change from antiferromagnetic toward ferromagnetic ordering. Density functional theory-based computations were performed to understand the materials' properties and to shed some light on the stability ranges. This allowed better understanding of the bonding pattern, especially of the Au-containing substructure, and to elucidate the role of the third element in the type stability.

Introduction

Rare earth and gold-containing intermetallic compounds such as those within the *R*-Au-*M* family (R = rare earth, M = groups 13-15) have received much research interest in the last few

years, with attention recently moving toward the less explored gold-rich regions of the systems.[1-7] Many such compounds show uncommon structural motifs as well as varied electronic and magnetic properties such as ferromagnetism, magnetocaloric effect, superconductivity, and thermoelectricity among others.

The well-studied relativistic effects on gold's 5*d* and 6*s* orbitals often produce notable structural and bonding features, which make it an advantageous component in the search for new intermetallic compounds.[8-14] Examples of gold's versatility in structure and bonding are extensive and include quasicrystals and their approximants,[15-17] as well as unique gold assemblies. Some examples include: isolated Au_7 clusters in $A_4Au_7X_2$ (*A* = K, Rb, Cs; *X* = Ge, Sn),[18,19] one dimensional columns such as Au zig-zag chains in Ca_3Au_3In,[20] and two dimensional slabs that are found in K_2Au_3.[21] Three dimensional gold networks are found in multiple forms such as: interconnected trigonal bipyramids found in KAu_5,[22] hexagonal diamond-like frameworks of Au as seen in the series of *Ae*-Au-*Tr* systems,[5,23-28] and combinations of tetrahedral and square planar Au fragments in Rb_3Au_7.[29]

The shielded 4*f* electrons of the rare-earth elements deliver the unpaired spins essential to provide a wealth of interesting magnetic properties in their compounds. The varying magnetic moments and atomic sizes moving across the lanthanides allow for fascinating alteration of magnetic interaction. Metals and metalloids from groups 13-15 with similar radii to Au (In, Sn, Sb, etc.) may allow significant site mixing and, furthermore, act as a bank of available options useful in tuning the valence electron count of the *R*-Au system toward the formation of stable compounds with unprecedented properties.

Within the *R*-Au-*M* family, only a few compounds have been discovered with concentration of gold over 50%, making this section particularly interesting for further exploration. Of these compounds, most of the recent research has focused on ternary compounds with tin and has led to the discovery of the $R_3Au_7Sn_3$ series of compounds, which can be described as superstructural

polyhedral packing of ZrBeSi-type featuring a new homoatomic Au cluster, Au@Au_6[2,3]. However, gold rich systems in combination with rare earth elements and group 15 elements are still largely underexplored. The high content of gold allows for a higher chance of homoatomic formations and more opportunities to explore the variety of Au-Au bonding and to investigate the capability of group 15 elements (Pn, pnictogen) to stabilize the structures and to affect such formations. The only up-to-date known *R*-Au-*Pn* structure with gold being the majority component, is $R(Au_{\sim 0.75}Sb_{\sim 0.25})_2$ (*R* = La, Ce, Pr).[30] These compounds serve as an evidence for the ability of group 15 like Sb to induce structural changes and to stabilize new formations. In this work we report on the first example of a gold-rich phase, where the group 15 element acts as an independent constituent and allows for the stabilization of a certain structure type.

Experimental Section

1. Synthesis

Starting materials used for synthesis were Au (99.98 %), rare earth elements (99.9+ %) and Bi (99.999 %) from the Materials Preparation Center in Ames Laboratory, and Sb (99.99%) from Alfa Aesar. Extra Au and Bi were also purchased from MaTeck (99.99%) and Alfa Aesar (99.999%) respectively. A representative of the R_3Au_9Pn series was first observed in the Gd-Au-Sb system as the majority phase in a sample loaded with Gd:Au:Sb in a 2 : 5 : 1 ratio that was reacted in a sealed tantalum ampule jacketed in fused silica at 1000°C for 3 hours, followed by annealing at 850°C for 12 hours. Different synthetic conditions were then tested to replicate results, obtain R_3Au_9Pn phase-pure, or test for formation with other rare earth elements (Y, La–Nd, Sm–Lu tested with Au and Sb) or 13-15 group elements (Al, Ga, In, Sn, Sb, and Bi tested with Gd and Au). The general strategy was to react the starting materials at high temperatures either by heating in an electrical-resistance furnace until at least one component reached liquid state or by arc melting, followed by annealing at lower temperature to create higher quality single crystals for X-

ray structure analysis. Samples were typically furnace cooled as opposed to quenching back to room temperature. The total mass of samples prepared was 0.5-2.0 g, and all samples were handled under inert conditions (glove boxes and other similar chambers) using standard techniques (such as oxide removal by surface filing of rare earth metals).

For the arc melted samples, ~6% extra mass of Sb or Bi was added in order to compensate for their loss occurring due to their relatively high vapor pressures. The starting materials (in the form of filings or small chunks) were pressed into a pellet with group 13-15 element pieces placed on one side, which was positioned away from direct contact with the arc. The sample was arc melted under an inert Ar environment for short periods (~5 seconds or until the surface appeared fully molten) and flipped three-four times between each re-melting to improve homogeneity. The arc melted samples were sealed by arc welding into tantalum tubes under inert Ar atmosphere, then enclosed under vacuum in fused silica tubes and set in a tube furnace for annealing at 850°C for 2 days, followed by 700°C for 5 days.

For reactions in resistance furnaces, amounts of *R* elements, Au and Sb (or Bi) in the stoichiometric ratio 3 : 9 : 1 were sealed by arc welding in Ta tubes, closed under vacuum in fused silica casings before high-temperature reaction and anneal in a tube furnace. The goal of most self-flux reactions is to melt a low melting component to initiate the reaction with higher melting temperature components such as the rare earth elements. We note that the temperatures required to initiate reactions are well beyond the melting points for most of the group 13-15 elements tested. Preliminary testing for R–Au–Sb (Sb melts at 631°C) showed that reactions at 850°C (significantly under the melting point of Au) were not adequate to combine the components. Therefore, the temperature was raised to ensure that the main component, gold, was molten as well. All samples, once removed from their various crucibles appeared dark gray with a metallic luster, and remained stable in air weeks later.

2. X-Ray Analysis

Samples were examined by X-ray powder diffraction for phase analysis by using either a STOE STADI P diffractometer with a STOE image plate detector or a STOE GmbH Guinier photographic camera with Cu $K_{\alpha 1}$; λ = 1.54059 Å (Si as an internal standard, a = 5.4308(1) Å). Powders were prepared by grinding, then sieved to 38μm particles and dispersed onto either vacuum grease between Mylar© sheets and fixed by Al rings, or placed on a single crystal Si zero background plate depending on the instrument. Data were analyzed using the *WinXPow 3.06* and *LAZY PULVERIX* software packages[31].

The microstructure and homogeneity of samples were characterized by optical and scanning electron microscopies (OM and SEM), the latter equipped with electron microprobe (Energy Dispersive X-ray analysis, EDS) for semi-quantitative elemental analysis. A Leica Cambridge 360 microscope, equipped with an Oxford X-Max 20 analyzer was used with Oxford Aztec software, utilizing an extra high-tension voltage of 20.0 kV and probe current of 220 pA. EDS analyses were performed on at least three small areas to identify the phase composition (counting time of 60 sec); the accuracy from the EDS is within 1 at%. The semi-quantitative atomic concentration data were also used as a check of results from single crystal refinement.

Single crystals were selected from crushed sample pieces and affixed to a glass fiber with grease. They were tested at room temperature on either a Bruker APEX CCD diffractometer or a Bruker D8 VENTURE diffractometer (both with Mo K_{α} radiation; λ = 0.71073 Å), utilizing the APEX 2 and APEX 3 software suites (for the former and the latter diffractometer, respectively) for data collection, integration, polarization, and empirical absorption correction[32,33]. Scans typically covered the 2θ range of ~5-63°. The XPREP algorithms in the SHELXTL suite were used to check the intensity data sets for extinction conditions and E statistics necessary allowing

for the assignment of the proper *P*6$_3$/*m* space group. Direct methods were used for structure solution (SHELXS-97)[34]. Structure refinement (refined atomic position, mixed site occupancy and anisotropic displacement parameters) was carried out with APEX 3 software. For details on the data collection; structure solution and refinement see Table 1. Table 2 contains the atomic coordinates for Y_3Au_9Sb, Gd_3Au_9Sb, Dy_3Au_9Sb, and Gd_3Au_9Bi. The structure of Gd_3Au_9Sb we will discuss in detail as a representative of the series.

3. Thermal analyses

Differential thermal analysis (DTA) was performed on portions of 0.7-0.9 g of samples, either in the as-cast or annealed form. Each sample was enclosed in an out-gassed Mo crucible by arc welding under Ar atmosphere, then transferred to the DTA equipment (Netzsch 404 thermal analyzer). Mo crucibles were chosen because of their better refractory properties with respect to Au at the higher temperatures of DTA. Thermal cycles were carried out with rates of 20°C/min on heating and 10°C/min, or 5°C/min on cooling, under an Ar atmosphere. The accuracy in the temperature measurements was ± 5°C.

4. Electronic structure calculations

Calculations were performed in order to understand the structural preferences, physical properties and stability ranges of the compounds under investigation. The Vienna *ab initio* Simulation Package (VASP) [35-39] was utilized to perform structural optimizations (unit cell volume, shape and atomic coordinates) prior to any band structure calculations until energy difference between two iterations fell below 0.01 meV/cell. The DFT (density functional theory) computations in the generalized-gradient approximation (PBE-GGA) [40] were carried out utilizing the projector-augmented wave (PAW) method of Blöchl[41], as adapted in the VASP code. The

energy cutoffs of the plane wave basis sets were set to 500 eV, while starting meshes of up to 8 × 8 × 8 *k*-points were used to sample the first Brillouin zones for reciprocal space integrations.

A chemical bonding map of Y_3Au_9Sb was accomplished based on the crystal orbital Hamilton population (COHP) analysis. COHP and their corresponding integrated values (ICOHP) were obtained in two ways – using the tight-binding linear-muffin-tin orbital (TB-LMTO) method with the atomic sphere approximation (ASA) in the Stuttgart code.[42,43] For the TB-LMTO-ASA calculations Wigner-Seitz spheres (WS) and empty spheres (ES) were automatically assigned, in order to best approximate the overlapping potentials in line with the full potentials. The following orbitals were utilized in the basis set (downfolded[44] orbitals in parentheses): Au-6*s*/-6*p*/-5*d*/(-5*f*); Y-5*s*/(-5*p*)/-4*d*/(-4*f*); Sb-5*s*/-5*p*/(-5*d*)/(-4*f*). The corresponding WS radii were [Å]: Au: 1.60, 1.60 and 1.62; Y: 1.85; Sn: 1.82. Reciprocal space integrations were performed with the tetrahedron method[45] using 312 irreducible *k*-points.

5. Physical Property Measurements

DC magnetization data for the Ho_3Au_9Sb single phase sample was collected in a Quantum Design MPMS (Magnetic Property Measurement System) SQUID (Superconducting Quantum Interference Device) magnetometer. A powder specimen of ~20 mg was placed in a fused silica sample holder that was made gas-tight using Teflon tape. The sample was first tested in a DC field of 1 kOe over a temperature range of 2-300 K in order to determine the magnetic behavior and possible critical temperature locations. Isothermal magnetization measurement at 2 K followed with fields up to ±70 kOe. Finally, further DC measurements in fields of 5 kOe, 15 kOe, and 40 kOe were performed (temperature ranges of 2-250 K, 2-300 K, and 2-300 K respectively).

Results and Discussion

1. Crystal Chemistry.

Crystals of sufficient quality for single crystal X-ray diffraction analysis could be obtained for Y_3Au_9Sb, Gd_3Au_9Sb, Dy_3Au_9Sb and Gd_3Au_9Bi. Structure analysis for Gd_3Au_9Sb reveals a complex 3D gold network comprised of $Au@Au_{6+2}$ bicapped trigonal prisms and $Sb@Au_6$ trigonal antiprisms as the most characteristic feature (Figure 1). Layers of alternating edge-sharing $Au@Au_6$ and $Sb@Au_6$ trigonal antiprisms are connected through the layers of interchanging Au atoms (which are the capping atoms of the $Au@Au_6$ trigonal antiprisms) and *R* triangles. The interatomic Au–Au distances within the central $Au@Au_6$ cluster range between 2.8242(4) and 2.8955(7) Å being consistent with the sum of corresponding covalent radii and are similar to those found in other Au-rich intermetallics.[2,3] It is worth noting that the Au-Au contacts between the central position and the surrounding trigonal prism in $Au@Au_6$ are the shortest gold contacts in the structure, while the distances to the Au atoms capping the trigonal prism are fairly long (2.9937(6) Å). The distances between the capping gold atoms of the $Au@Au_{6+2}$ prism and the Au vertices of other, nearby $Sb@Au_6$ antiprisms (2.8758(5) Å) are also appropriate distances for Au-Au interactions. Thus, a rather extended network of gold atoms is formed. The only known formations, similar to the $Au@Au_{6+2}$ prisms appear to be $Au@Au_8$ clusters that are stabilized with phosphine and form different conformations.[46] A non-centered, "naked" Au_9 cluster has also been predicted by Density Functional Theory (DFT) to be stable in the gas phase.[47]

Gadolinium atoms cap all three rectangular faces of the $Au@Au_{6+2}$ polyhedra with a distance of 3.0654(6) Å from the central gold atom and 3.1175(6) Å to the gold atoms on the rectangular faces. In summary, a fully capped trigonal prism $Au@Au_6Au_2Gd_3$ is formed around the central gold atom. The $Au@Au_6Au_2Gd_3$ units similarly form layers through Au vertex-sharing with $Sb@Au_6$ antiprisms. The Sb–Au distances are fairly long at 3.0165(4) Å (compared to the sum of their theoretical covalent radii, 2.850 Å[50]). However, the Au-Au distances along the edges of the

Au antiprism around the central Sb atom are, within values of 3.3274(5) Å and 5.0323(2) Å, even longer when compared to the sum of the covalent radii for gold, 2.880 Å. The second coordination sphere of Sb includes two Gd triangles (3.3578(5) Å) resulting in an overall coordination number 12 and an icosahedron as the coordination polyhedron. The gadolinium atoms themselves form a slightly distorted triangular network (due to inclusion of Au atoms), with three different interatomic distances (4.3036(2), 4.5904(2) and 5.3094(3) Å); see Figure A2. The longest distance refers to the Gd-Gd distances of a triangle surrounding the Au3 position, while the two shorter distances refer to Gd-Gd distances of two other triangles not centered by atoms. However, all three distances are noticeably longer than the covalent radii sum of 3.580 Å[50].

Unit cell parameters of the other isotypic R_3Au_9Pn compounds were derived from X-ray powder diffraction data. Their values are in line with the expectations from the lanthanide contraction, as well as with the increase in atomic size from Sb to Bi (Table 3). The average covalent radius[48] of *R* atoms used in forming R_3Au_9Pn is 1.92 Å, somewhat below the average of 1.96 Å forming the structurally similar $R_3Au_7Sn_3$ phase, while the radii of Au, Sn, and Sb are all nearly identical (1.36, 1.39, and 1.39 Å respectively). However, R_3Au_9Pn only formed for covalent radii ratios of *R*/Au between 1.40-1.44, but allowed for more variation with *R*/*Pn*: from Y/Sb (1.28) to Gd/Bi (1.41).

The R_3Au_9Pn structure is closely related to the structure reported for the $R_3Au_7Sn_3$ series[2,3], where both can be viewed as ordered representatives of the $Cu_{10}Sn_3$ structure type.[49] If one rewrites the formula of $R_3Au_7Sn_3$ as $R_3Au_7Sn'_2Sn''_1$, the compositional relationships become more evident; replacing Sn′ by Au and Sn″ by Sb leads to R_3Au_9Sb. The Au substitution also leads to some decrease of the unit cell volume (~4%) followed by a rather large increase (~22%) in density. However, upon substituting Sn by Au, the atomic position of the latter shifts slightly farther away from the center plane of the slab. Figure 2 displays a comparison of the common building unit in

the crystal structures of $Cu_{10}Sn_3$, $R_3Au_7Sn_3$, R_3Au_9Pn and $Gd_{14}Au_{51}$. From this viewpoint, the Gd_3Au_9Sb type appears to be a missing link connecting the two known binary types $Cu_{10}Sn_3$ and $Gd_{14}Ag_{51}$ and the recently discovered $Gd_3Au_7Sn_3$. On the other hand, R_3Au_9Pn is compositionally situated between $R_3Au_7Sn_3$ and $R_{14}Au_{51}$ or, more importantly, its ternary representatives $R_{14}(Au, M)_{51}$ (M = Group 13-15) [50,51]. The latter is known with all rare earths, several transition metals, and may accommodate the majority of post-transition metals. The crystal structure of $R_{14}(Au, M)_{51}$, due to a slightly different R content, contains similar Au centered and non-centered fully capped trigonal prisms complemented by interpenetrated Frank-Kasper polyhedra centered on the R sites along the z axis. A representation outlining similar polyhedra between $Gd_{14}Au_{51}$ and Gd_3Au_9Sb structures is found in Figure A3. Indeed, it was found that the $R_{14}(Au, M)_{51}$ phase is a strong competitor of R_3Au_9Pn, melting congruently at much higher temperatures, and being just a few at.% away compositionally (having visible homogeneity ranges). In fact, 12 of 15 unique elemental combinations used in attempts to synthesize R_3Au_9Pn yielded $R_{14}(Au, M)_{51}$, and 9 of those cases formed $R_{14}(Au, M)_{51}$ as the majority component as evidenced by PXRD.

Scanning electron microscopy analysis for a sample of nominal Tb_3Au_9Sb, revealed two similar but distinct phases: the phases appear discrete within the micrographs (Figure 3); the dark and light phases correspond to the Tb_3Au_9Sb and $Tb_{14}(Au,Sb)_{51}$, respectively. The EDS data are collected and summarized in Table 4. These values support the proposed formula for the Tb_3Au_9Sb compound, and indicate the existence of the compositionally similar ternary $Tb_{14}(Au,Sb)_{51}$ solid solution phase (as well the amount of Au-Sb mixing within). It is expected that the R_3Au_9Pn phases (Pn = Sb, Bi) do not form (or have very restricted, and as of yet unobserved existence ranges) for all rare earths. For example, no lanthanides lighter than Gd formed R_3Au_9Sb, often preferring $R_{14}(Au, M)_{51}$ structure, allowing the R_3Au_9Pn phases to play a role as a structural connection

between $R_3Au_7Sn_3$ and R_{14}(Au, M)$_{51}$. In this view, $R_3Au_7Sn_3$ appears as a byproduct, which is stabilized by insertion of a heteroatom in the center of the other systems' Au@Au_6 trigonal prisms.

2. Physical Properties

To elucidate the magnetic properties, the magnetization for phase-pure Ho_3Au_9Sb (PXRD pattern shown in Figure A4) was measured as a function of temperature, M(T), in applied magnetic fields of 1 kOe (between 2 and 250 K). A sharp peak at around 10 K in the magnetization curve can be associated with 1050a paramagnetic (PM) to antiferromagnetic (AFM) transition (inset of Figure 4). The isothermal magnetization, M(H), was measured at T = 2 K (below the critical temperature) and in between ± 70 kOe (Figure 5). The data show a peculiar behavior for this compound: from 0 to about 10 kOe the behavior is typical of an AFM material, with the magnetization weakly and almost linearly increasing with increasing magnetic field. Then, two field-induced metamagnetic transitions take place at 10.5 kOe (H1) and 20 kOe (H2) as determined from the maxima of the first derivative of the magnetization *versus* the applied magnetic field, dM/dH, (Figure A5). A small, though noticeable, hysteresis is also present after the first transition (Figure A5). Even at the highest applied field of 70 kOe, the magnetization keeps increasing without reaching gJ = 10 μ_B/ Ho^{3+}. This implies that either the ferromagnetic state is not collinear, or crystalline electric field effects are quite substantial. Neutron diffraction investigation as a function of magnetic field would be necessary to shed light on the complex magnetic behavior of this compound.

The two transitions noted in the isothermal magnetization data prompted further field cooled (FC), and zero field cooled (ZFC) M(T) measurements at fields congruent with the three regions separated by the transitions: 5 kOe (before H1), 15 kOe (before H2), and 40 kOe (after H2). The first was measured between 2 and 250 K, while the latter two were between 2 and 300 K (Figure 4). The data in both the 1 and 5 kOe curves show a trend typical of an AFM behavior where the

magnetization approaches nearly zero value below T_N. Meanwhile, the data at 15 and 40 kOe better represent the behavior of an FM-like material due to the much higher magnetizations below T_N.

The inverse magnetic susceptibility, $1/\chi$, plotted against temperature was used to determine the Weiss temperature (θ_P) and the effective moment (μ_{eff}) using the Curie-Weiss law, $\chi = C/(T-\theta_P)$ as illustrated in Figure 6. The Weiss temperature is slightly positive (4.0 K), pointing to a ferromagnetic ground state. The effective moment per rare earth atom (10.80 μ_B/Ho^{3+}) is close to the expected theoretical value calculated from Hund's rule for non-interacting Ho^{3+} ions (10.60 μ_B/Ho^{3+}).[52]

Analogous to the $R_3Au_7Sn_3$ structure, the triangular *R* lattice in R_3Au_9Pn does not indicate geometrical spin frustration. For $R_3Au_7Sn_3$, the low temperature, low field ordering predicted based on total energy calculations is spin up across a layer and spin down in the opposite layer as described for $Gd_3Au_7Sn_3$.[2] Possible ferrimagnetic (FIM) ordering in R_3Au_9Pn appears unlikely due to a single *R* site and its triangular lattice. Reported low field measurements for $R_3Au_7Sn_3$ compounds all similarly show low temperature transitions from a PM state to AFM.[2,3] $Nd_3Au_7Sn_3$ and $Tb_3Au_7Sn_3$ also appear to undergo metamagnetic field induced transitions from an AFM state to FIM/FM. However, these transitions are less sharp than either of the transitions observed in Ho_3Au_9Sb. Transitions from PM to AFM were also noted for $R_{14}Ag_{51}$ compounds (for *R* = Gd, Tb),[53,54] which, despite the comparable centered and non-centered fully capped trigonal prisms, do not share the triangular, planar rare earth structure because of the additional *R* positions at the centers of the interpenetrated Frank-Kasper polyhedra.

3. Electronic structures

The existence of two structurally related but compositionally different $R_3Au_7Tt_3$ and R_3Au_9Pn series of compounds with tetrels and pnictogens points towards a strong influence of electronic factors, while formal electron counting rules do not provide any help. In spite of

significantly lower number of valence electrons in the latter, the compounds exist, yet with less of the rare earth elements as a side effect of geometric factors. On the other hand, all attempts to substitute *Pn* with triel or tetrels failed. The electronic structure of Y_3Au_9Sb was investigated as a prototype for the series to obtain a better understanding of this phenomenon and to predict further possibilities for the extended family.

The electronic Densities of States (DOS) curves for Y_3Au_9Sb reveal broad valence bands reaching –10 eV and large Au 5*d* contributions between 2.5–6.5 eV below the Fermi level (E_F) (Figure 7a). The Au bands are dominant through the entire region, while Y contributions become significant starting from –1 eV and above, and Sb contributions remain relatively small above –8eV in accordance with its concentration in the compound. This picture is rather typical for a number of related Au-rich phases in the A–Au–E systems (A = active metal, E = post-transition element).[2,3,25,55] A more interesting situation is observed around the Fermi level. The DOS regions exhibit non-zero values, pointing towards metallic characteristics as can also be confirmed by the band structure plot (Figure A6). Despite the presence of many local minima, there is a clear relatively deep but narrow pseudogap at E_F. This feature of its electronic structure is in good agreement with not only the strong restriction for post-transition elements but also with the absence of any detectable mixing in any site of the crystal structure. This LMTO model of the electronic structure confirms the absence of R_3Au_9Tt compounds and suggests the existence of the R_3Au_9Tr compounds, which have not been detected yet. On the other hand, chemistry of indides and antimonides is very different, in part due to the $5s^2$ lone pair in the latter, leading to the formation of homoatomic fragments and networks.[56] Such electron configuration differs from triels and tetrels, i.e. indium or tin, and affects Au–Sb and RE–Sb bonding as will be discussed below.

A closer inspection of the previously reported electronic structure of the $R_3Au_7Sn_3$ series[2,3] showed an easily detectable local minimum at ~7 e^-/f.u. less with respect to the investigated composition and rather huge pseudogap starting at the Fermi level. Our initial attempts to obtain

such a compound by replacing all Au positions in the structure by Pt (1 e^-/a less) failed, apparently due to much higher location of the Pt 5*d* band and switch of the potential pseudogap into the regions of extremely high density of states. The "solution" was unexpectedly found through the decrease of the post-transition element proportion along with the exchange of the latter. Finally, the electronic densities of states for the binary $Cu_{10}Sn_3$ exhibit a local minimum at E_F and a distinct pseudogap at $3e^-$/f.u., more indication of further possibilities of Cu exchange with more electron-rich components.

The mystery remains that the existence of each subgroup is restricted to a specific post-transition metal. As we mentioned above the crystal structures of R_3Au_9Pn and $R_3Au_7Tt_3$ do not belong to the same structure type but are rather very close relatives. On the other hand, we know $Au_{10}In_3$[57] as an example of a strong distortion of the $Cu_{10}Sn_3$ type. What factors are the most important for formation and stabilization of all these modifications? Every structure comes up with its own valence electron concentration (*vec*) values, which are not so close to each other even within the same group. While the $Au_{10}In_3$ representatives[58,59] are restricted to 19 e^-/f.u., the $Cu_{10}Sn_3$ type spreads in a wide range from 21 to 28 e^-/f.u. Geometric factors and electronegativities have also been considered as possible factors influencing the type preference but no clear difference has been detected. Moreover, partial overlap of the main criteria occurs for all considered cases. Let us consider changes within three different subgroups based on the transition element proportion in $Cu_{10}Sn_3$, $Y_3Au_7Sn_3$ and Y_3Au_9Sb. The most affected unit in all the structures is not entirely isolated $M^I_6M^{II}$ cluster (M^I = Au or Cu, M^{II} = Sn, Sb, Au). The position of the central atom is moving from nearly the center of the unit closer to the face and finally out of the Au_6 trigonal antiprism (Figure 2). Such atomic rearrangement, in spite of the same quantity and type of Wyckoff positions, does not allow us to consider all three examples as representatives of a single structure type in terms of bonding. This fact may also explain a lower importance of *vec* factor for the group in general; however, it does not neglect its role in each separate case.

To learn more about the structural stability and variability and the role of local changes in these processes, we continued with COHP analysis of the interatomic interactions. The COHP curves for the selected contacts are shown on the Figures 7b and c, while the corresponding ICOHP values are summarized in Table 5. The first unexpected result appeared from the bonding pattern of Au–Sb pairs, showing strong antibonding interactions at the Fermi level and around. The position of the E_F at the local minimum of antibonding region suggests some island of stability, but in general a much higher number of electrons would be required to move this interaction into the bonding region. A very different picture has been observed for $Y_3Au_7Sn_3$, where all Au–Sn and Au–Au interactions were found bonding or optimized up to the Fermi level, and a larger number of electrons is not anticipated. Such picture is indeed in good agreement with the observed Au–Sb bond lengths, and may partially explain the lower proportion of Sb in the compound if compared to Sn in the $R_3Au_7Sn_3$ phases. The limited number of Au–Sb bonds does not play the major role in the general picture; however, an increase of Sb concentration would lead to a higher number of antibonding interactions and structural instability.

The most interesting question in Y_3Au_9Sb is the significance of orbital interactions within the extended Au network, particularly in the formal Au_9 unit. Analysis of the various Au–Au pairs (Figure 7c) revealed characteristic differences for both intra- and inter-cluster separations depending on direction. The most populated Au–Au bonds occur in the center of the Au_9 unit (a bicapped trigonal prismatic Au_7 cluster) and between its vertices and Au(2) positions, axially capping the neighboring Au_7 trigonal prism. Six Au(2) atoms, with the shortest distances to the central Au_7 unit, are common for three such units leading to the formulation $Au@Au_6Au_{6/3}$ = $Au@Au_8$ = Au_9. Despite the identical look, this formulation proves the concept of a layered structure normal to the *c* axis. It is also worth noting that Au(3)–Au(2) interactions are strongly antibonding below the Fermi level, rather nonbonding at E_F, and show the least –ICOHP values comparing to all others and even longer Au(2)–Au(2) intercluster contacts.

Highly populated homoatomic Au–Au contacts together with relatively long and less populated Au–M (M = post-transition element) is not a usual picture for the majority of the investigated A–Au–Tr systems.[55,60,61] This bonding picture may serve as an extra proof why no R_3Au_9M compound has been observed with In, Ga or Al. Another interesting fact is the rather high contributions from the heteroatomic Y–Au and Y–Sb contacts, showing greater involvement of rare earth elements in the covalent interactions. Such picture is quite atypical for the light active metals; however, relatively high contributions have been detected for some phases with Na and Ba.[15,62] It is reasonable to expect that Au–Au contacts provide the greatest contribution to the total orbital interactions (Table 5), but the –ICOHP values of 0.6–0.7 eV/bond for the Y containing pairs guarantee the second place for the formal cation containing pairs, being comparable or even exceeding the contribution from the Au–Sb pairs.

Summary

The new series of isostructural Au-rich intermetallic compounds with general formula R_3Au_9Pn has been discovered and investigated being restricted to the majority of the heavy lanthanides or Y and heavy pnictides. The compounds crystallize in a hexagonal unit cell with its own structure type (Gd_3Au_9Sb-type), which is closely related to $Cu_{10}Sn_3$ and $Gd_3Au_7Sn_3$ and provides an excellent possibility to analyze the influence of all possible factors on the phase formation and stability of $Cu_{10}Sn_3$ related compounds. $Au@Au_6Au_2R_3$ fully capped trigonal prisms found within the R_3Au_9Pn series, isostructural to those of the $R_{14}Au_{51}$ series, create a structural link between the parent structures ($Cu_{10}Sn_3$ and $Gd_{14}Ag_{51}$), complementing the compositional similarities between the R_3Au_9Pn and $R_{14}Au_{51}$ series. Structural analysis and electronic structure calculations revealed $Au_9 = Au@Au_6Au_{6/3}$ as the main building block of the anionic network in contrast to more intuitive $Au@Au_6Au_2$ bicapped trigonal prism. The shift of the Au position with respect to the center of trigonal antiprismatic slabs from one type to another,

which occurs because of changing strength and type of interatomic interactions, explains failure of electron counting rules, lower importance of electronegativities, as well as geometric criteria in the hypothetically common structure type stability. Magnetization measurements in Ho_3Au_9Sb revealed antiferromagnetic ordering, with Néel temperature of 10 K; metamagnetic transitions observed with increasing magnetic field at 2 K suggest that a ferromagnetic state can be stabilized at high fields. Overall, the comparison with several closely related structure types allows for an explanation of structural changes, tuning of physical properties, and simplifies the search for new representatives in unexplored systems.

Table 1. Crystallographic details and refinement parameters for Y_3Au_9Sb, Gd_3Au_9Sb, Dy_3Au_9Sb, and Gd_3Au_9Bi.

Formula	Y_3Au_9Sb	Gd_3Au_9Sb	Dy_3Au_9Sb	Gd_3Au_9Bi
Structure type	Gd_3Au_9Sb	Gd_3Au_9Sb	Gd_3Au_9Sb	Gd_3Au_9Sb
Formula wt.	2381.95	2366.20	2161.18	2453.43
Space group	$P6_3/m$ (no. 176)	$P6_3/m$ (no. 176)	$P6_3/m$ (no. 176)	$P6_3/m$ (no. 176)
Z	2	2	2	2
a, Å	8.127(2)	8.1641(4)	8.127(2)	8.242(2)
c, Å	9.036(2)	9.0344(6)	8.998(3)	9.055(3)
V [Å^3]	516.9(3)	521.49(6)	514.7(3)	532.7(4)
Density (calculated) [g/cm^3]	13.885	15.069	15.370	15.295
Absorption coefficient μ [mm^{-1}]	146.260	147.278	151.670	158.126
F (000)	1758	1908	1920	1972
θ range for data collection	2.894 ° – 29.961°	2.881 ° – 31.886 °	2.894° – 28.997°	2.854° – 29.889°
Index ranges	$-11 \le h, k \le 11$ $-12 \le l \le 12$	$-11 \le h, k \le 11$ $-13 \le l \le 13$	$-11 \le h, k \le 11$ $-12 \le l \le 12$	$-11 \le h, k \le 11$ $-12 \le l \le 12$
Intensity data collected	9542	7512	6642	4449
Number of independent	483 [R_{int} = 0.0819]	521 [R_{int} = 0.0238]	411 [R_{int} = 0.0335]	404 [R_{int} = 0.0102]
Data/ Restraints/ Parameters	537/ 0/ 24	618/ 0/ 24	489/0/ 24	548/0/ 24
Goodness-of-fit (F^2)	1.132	1.120	1.109	1.035
R_1, wR_2 [$I_0>2\sigma$ (I)]	0.0325; 0.0624	0.0238; 0.0446	0.0335; 0.0731	0.0354; 0.0678
R_1, wR_2 (all data)	0.0399; 0.0644	0.0327; 0.0466	0.0421; 0.0759	0.0604; 0.0749
Largest diff. peak and hole [e·Å^{-3}]	3.889 and -3.558	4.770 and -2.926	3.666 and -3.341	5.192 and -3.856

Table 2. Atomic coordinates and equivalent isotropic displacement parameters for R_3Au_9Sb.

Atom	***Wyckoff site***	***x***	***y***	***z***	U_{eq}
Au1	12*i*	0.36854(7)	0.03302(7)	0.09038(5)	0.0065(2)
Au2	4*f*	1/3	2/3	0.0801(1)	0.0091(2)
Au3	2*c*	2/3	1/3	1/4	0.0083(3)
Y	6*h*	0.2877(2)	0.3219(2)	1/4	0.0043(3)
Sb	2*b*	0	0	0	0.0049(4)
Au1	12*i*	0.37176(5)	0.03425(5)	0.08975(4)	0.0039(1)
Au2	4*f*	1/3	2/3	0.08137(7)	0.0035(1)
Au3	2*c*	2/3	1/3	1/4	0.0054(2)
Gd	6*h*	0.28498(9)	0.32057(8)	1/4	0.0016(1)
Sb	2*b*	0	0	0	0.0010(3)
Au1	12*i*	0.36988(8)	0.03385(8)	0.08978(6)	0.0081(2)
Au2	4*f*	1/3	2/3	0.0826(1)	0.0083(3)
Au3	2*c*	2/3	1/3	1/4	0.0093(3)
Dy	6*h*	0.2864(1)	0.3214(1)	1/4	0.0063(3)
Sb	2*b*	0	0	0	0.0072(5)
Au1	12*i*	0.3754(1)	0.0338(1)	0.09165(8)	0.0108(2)
Au2	4*f*	1/3	2/3	0.0802(1)	0.0110(3)
Au3	2*c*	2/3	1/3	1/4	0.0139(4)
Gd	6*h*	0.2879(2)	0.3238(2)	1/4	0.0087(3)
Bi	2*b*	0	0	0	0.0093(4)

Table 3. Lattice parameters (*a* and *c*), observed unit cell volume (V_{obs}) and formation volume (ΔV %) for R_3Au_9Pn (*Pn* = Sb, Bi).

R_3Au_9Sb	Lattice parameters *a* [Å]	*c* [Å]	V_{obs} [Å^3]	ΔV % from Gd_3Au_9Sb PXRD	Obtained by
Gd_3Au_9Sb	8.1641(4)	9.0344(6)	521.49(1)		SCXRD
Gd_3Au_9Sb	8.1809(1)	9.0751(1)	526.00(9)	0	PXRD
Tb_3Au_9Sb	8.1432(3)	9.0345(7)	518.83(9)	-7.17	PXRD
Dy_3Au_9Sb	8.127(2)	8.998(3)	514.6(8)	-11.3	SCXRD
Ho_3Au_9Sb	8.1083(3)	9.0059(7)	512.76(4)	-13.25	PXRD
Er_3Au_9Sb	8.0800(1)	8.9773(3)	507.57(4)	-18.44	PXRD
Tm_3Au_9Sb	8.079(1)	8.977(1)	507.4(3)	-18.61	PXRD
Y_3Au_9Sb	8.1327(6)	9.0486(1)	518.30(1)	-7.71	PXRD
Y_3Au_9Sb	8.1274(2)	9.036(2)	516.9(3)		SCXRD
Gd_3Au_9Bi	8.242(2)	9.055(3)	532.7(4)	+12.7	SCXRD

Table 4. EDS data corresponding to the SEM images of a Tb DTA sample with nominal composition Tb_3Au_9Sb (see Figure 3).

Element	Average (overall)		Dark phase (A)		Light phase (B) (≤ 3 vol.%)	
	wt.%	at.%	wt.%	at.%	wt.%	at.%
Tb	18.93	21.78	19.23	22.08	17.67	20.75
Au	75.87	70.41	75.39	69.86	80.24	76.04
Sb	5.2	7.8	5.38	8.06	2.09	3.21

The phase with higher terbium content shows a composition similar to the expected atomic percentages for the Tb_3Au_9Sb phase, while the one with the lower terbium content suggests the $Tb_{14}(Au, Sb)_{51}$ phase.

Table 5. Bond lengths and ICOHP values for the selected interactions in Y_3Au_9Sb.

Bond type	Length (Å)	–ICOHP/bond (eV)	no./cell	–ICOHP (eV)	contribution(%)
Au–Au	2.824	1.26	12	15.12	14.04
Au–Au	2.858	1.25	12	15	13.93
Au–Au	2.876	1.08	6	6.48	6.02
Au–Au	2.895	1.27	6	7.62	7.08
Au–Au	2.916	1.08	6	6.48	6.02
Au–Au	2.994	0.78	4	3.12	2.90
Au–Au	3.046	1.10	2	2.2	2.04
Au–Sb	3.017	1.06	12	12.72	11.81
Y–Au	3.044	0.73	26	18.98	17.63
Y–Au	3.117	0.65	20	13	12.08
Y–Sb	3.358	0.64	12	6.4	7.13
Y–Y	4.303	0.07	6	0.42	0.39
Y–Y	4.591	0.02	6	0.12	0.11

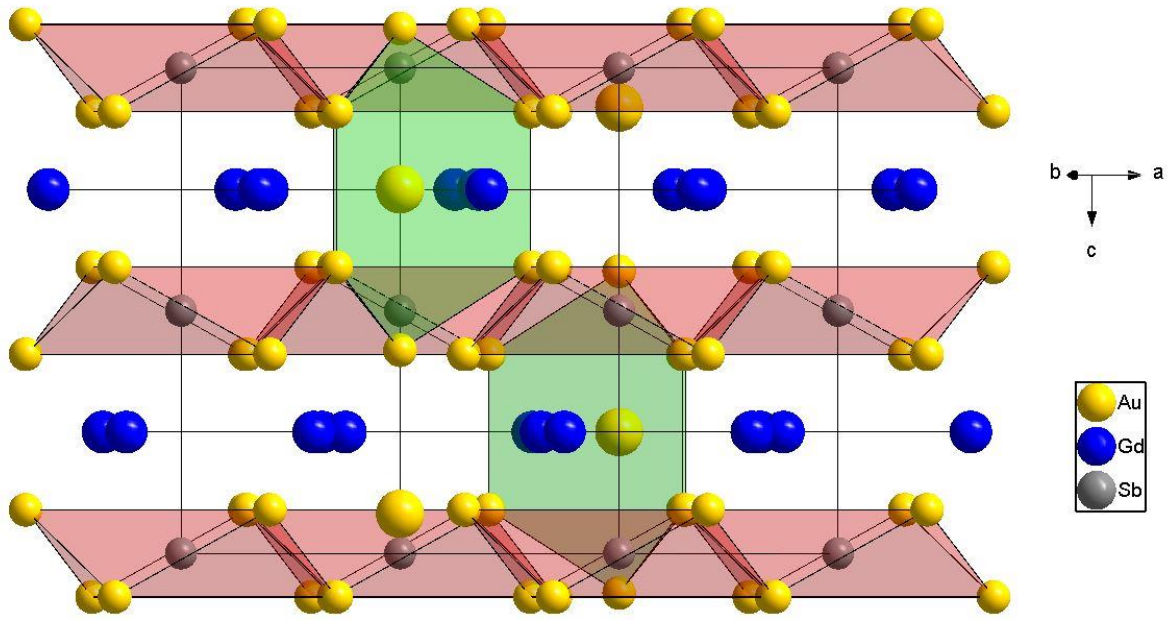

Figure 1. Representation of the crystal structure of Gd_3Au_9Sb; the three main fragments characterizing the structure are noticeable. The green bicapped trigonal prisms denote $Au@Au_8$ units. The red polyhedra denote $Sb@Au_6$ trigonal antiprisms that share vertices with the basal planes of the bicapped trigonal prisms. Trigonal planes of Gd are in plane with the center atom of the bicapped trigonal prisms, as shown in following figures.

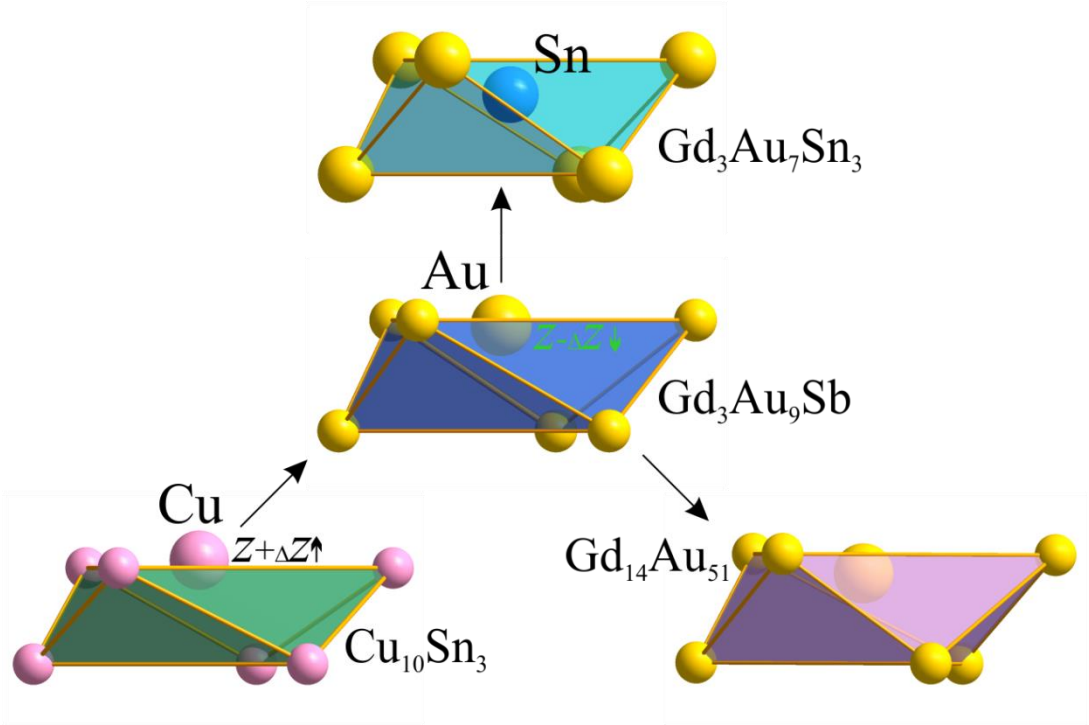

Figure 2. Variation of the common building unit in the crystal structures of $Cu_{10}Sn_3$, $R_3Au_7Sn_3$, R_3Au_9Pn and $Gd_{14}Au_{51}$.

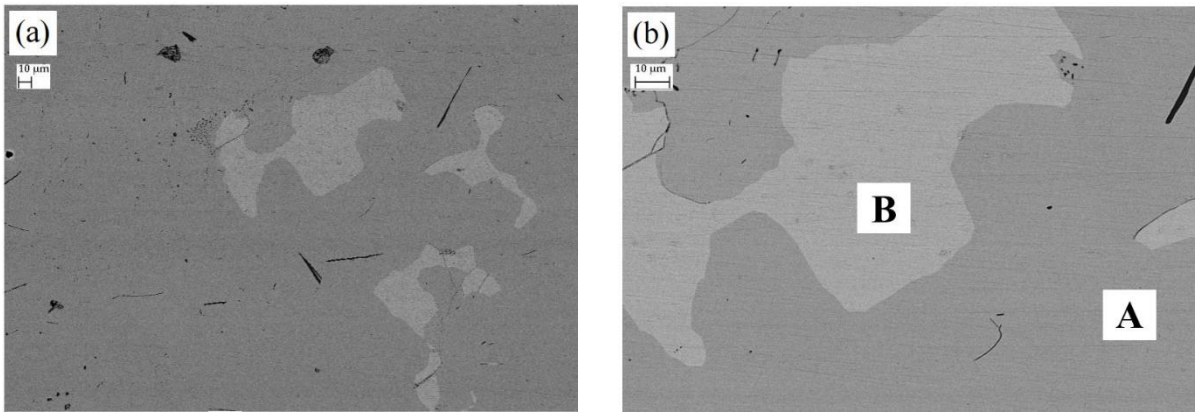

Figure 3. SEM micrograph (backscattering mode) of a sample with nominal composition Tb_3Au_9Sb (a). Portion of sample, at higher magnification, used for EDS analysis (b) [the data corresponding to the phases A, Tb_3Au_9Sb, and B, $Tb_{14}(Au,Sb)_{51}$, can be found in Table 3].

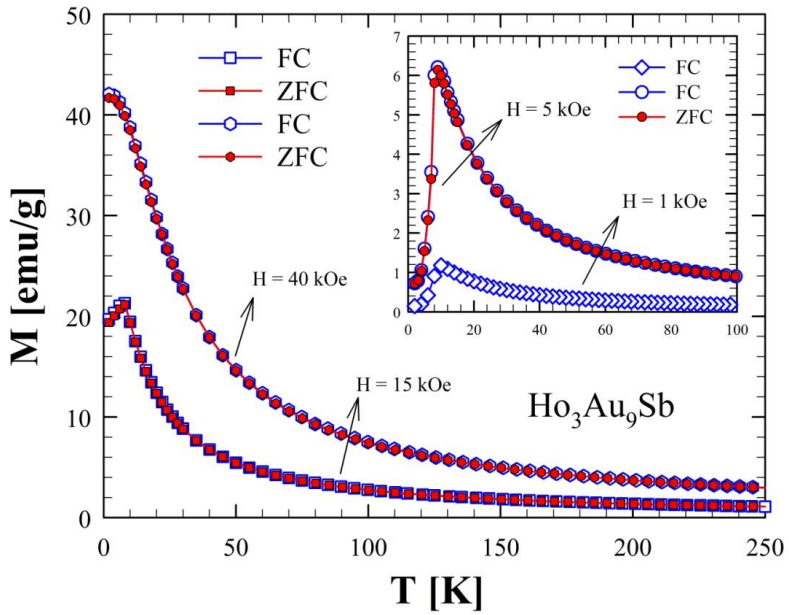

Figure 4. Magnetization *versus* temperature for Ho_3Au_9Sb measured in applied magnetic fields of 1 and 5 kOe (top right inset), 15 and 40 kOe between 2 and 250 K.

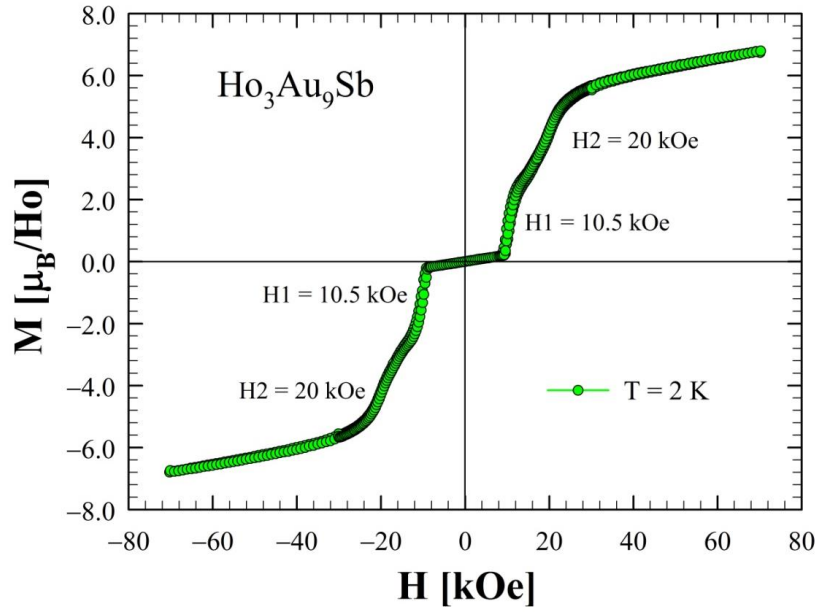

Figure 5. Isothermal magnetization measured at T = 2 K between −70 and 70 kOe for Ho_3Au_9Sb compound. Transition field values are listed alongside the curves.

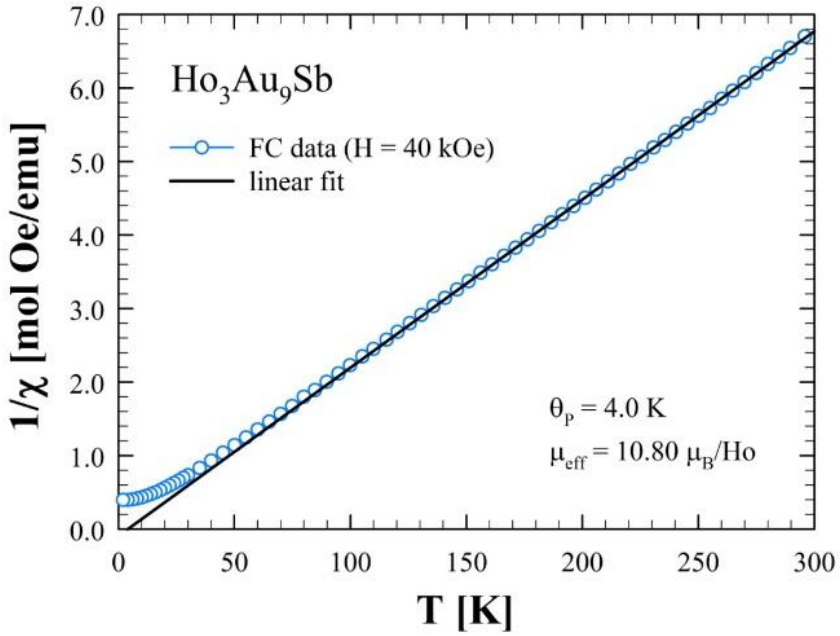

Figure 6. Curie-Weiss fitting of field cooled inverse susceptibility curve over 2-300 K temperature ranges for 40 kOe field.

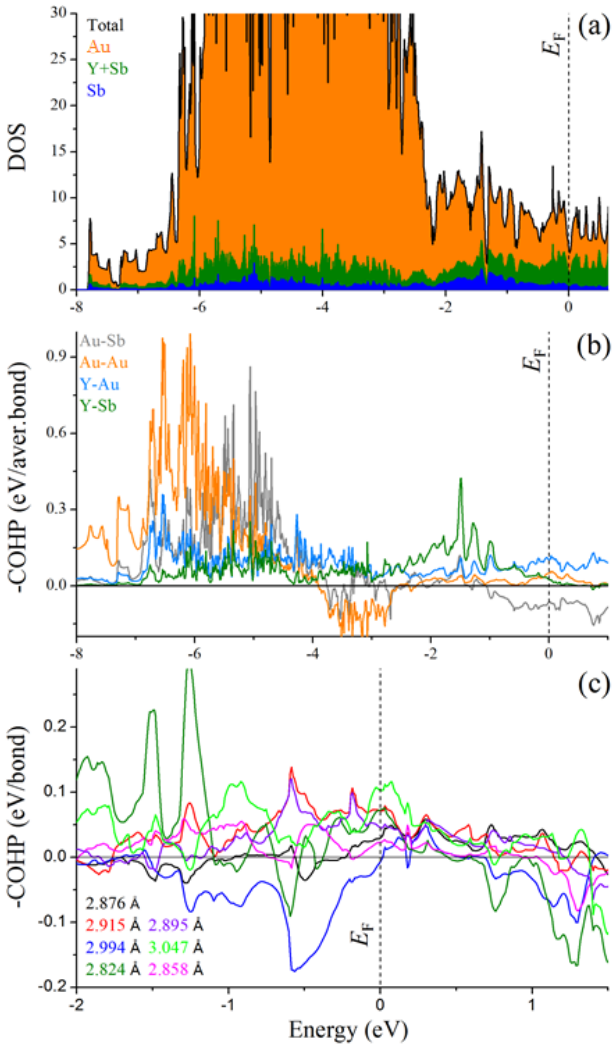

Figure 7. Plots of (a) total and projected DOS curves for Y_3Au_9Sb, (b) and (c) average and interaction projected COHP curves. The Fermi level is represented by dashed lines.

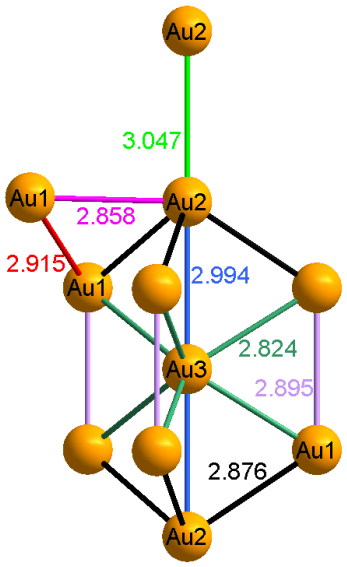

Figure 8. Interatomic Au–Au contacts in Å around Au_9 formation as observed in the crystal structure of Y_3Au_9Sb.

Information in Appendix

Thermal treatments of various samples; atomic displacement parameters for Gd_3Au_9Sb; alternate representation of the layered structure (Au/Sb slabs and Gd/Au triangular plane); comparison of R_3Au_9Pn and $R_{14}Au_{51}$ polyhedra; hysteresis and critical field data for Ho_3Au_9Sb; band structure of Y_3Au_9Sb. PXRD pattern and Rietveld refinement for Ho_3Au_9Sb. DSC data from relevant segment for Ho_3Au_9Sb. This material is available free of charge via the Internet at http://pubs.acs.org.

Accession codes

CSD- 432556, 432557, 432558 and 433017 contain the supplementary crystallographic data for this paper (Y_3Au_9Sb, Gd_3Au_9Sb, Dy_3Au_9Sb and Gd_3Au_9Bi respectively). These data can be obtained free of charge from FIZ Karlsruhe, 76344 Eggenstein-Leopoldshafen, Germany (fax: (+49)7247-808-666; e-mail: crysdata@fiz-karlsruhe.de.

Acknowledgments

The research was supported by the Office of the Basic Energy Sciences, Materials Sciences Division, U.S. DOE. Ames Laboratory is operated for DOE by Iowa State University under Contract DE-AC02-07CH11358.

Synopsis Image and Text

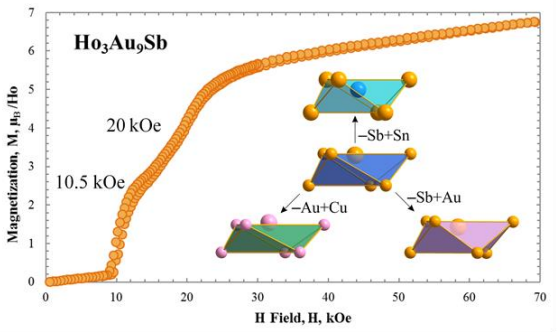

The newly discovered series R_3Au_9Pn (R = Y, Gd, Tb, Dy, Ho; Pn = Sb, Bi) acts as a structural focal point, connecting $Cu_{10}Sn_3$, $R_3Au_7Sn_3$, and $R_{14}Au_{51}$ intermetallic structures. Electronic structure calculations and magnetic property measurements shed light on the anionic substructure as well as the metamagnetic transitions the system undergoes.

References

(1) Fickenscher, T.; Rodewald, U.; Pottgen, R. Ternary stannides $RE_2Au_5Sn_2$ (RE = Gd-Er)-i3 superstructures of the Fe_2P type. *Z. Kristallorg.* **2015**, *230*, 117-122.

(2) Provino, A.; Steinberg, S.; Smetana, V.; Kulkarni, R.; Dhar, S.; Manfrinetti, P.; Mudring, A. Gold-rich $R_3Au_7Sn_3$: establishing the interdependence between electronic features and physical properties. *J. Mat. Chem. C* **2015**, *3*, 8311-8321.

(3) Provino, A.; Steinberg, S.; Smetana, V.; Paramanik, U.; Manfrinetti, P.; Dhar, S. K.; Mudring, A.-V. Gold in the layered structures of $R_3Au_7Sn_3$: from relativity to versatility. *Cryst. Growth Des.* **2016**, *16*, 5657-5668.

(4) Gebresenbut, G.; Tamura, R.; Eklöf, D.; Gomez, C. Syntheses optimization, structural and thermoelectric properties of 1/1 Tsai-type quasicrystal approximants in RE-Au-SM systems (RE = Yb, Gd and SM = Si, Ge). *J. Phys.: Condens. Mat.* **2013**, *25*, 135402.

(5) Smetana, V.; Steinberg, S.; Card, N.; Mudring, A.; Miller, G. Crystal Structure and Bonding in $BaAu_5Ga_2$ and $AeAu_{4+x}Ga_{3-x}$ (Ae = Ba and Eu): Hexagonal Diamond-Type Au Frameworks and Remarkable Cation/Anion Partitioning in the Ae-Au-Ga Systems. *Inorg. Chem.* **2015**, *54*, 1010-1018.

(6) Bigun, I.; Steinberg, S.; Smetana, V.; Mudryk, Y.; Kalychak, Y.; Havela, L.; Pecharsky, V.; Mudring, A.-V. Magnetocaloric behavior in ternary europium indides EuT5In: probing the design capability of first-principles-based methods on the multifaceted magnetic materials. *Chem. Mater.* **2017**, *29*, 2599-2614.

(7) Smetana, V.; Steinberg, S.; Mudryk, Y.; Pecharsky, V.; Miller, G. J.; Mudring, A.-V. Cation-poor complex metallic alloys in Ba(Eu)–Au–Al(Ga) systems: identifying the keys that control structural arrangements and atom distributions at the atomic level. *Inorg. Chem.* **2015**, *54*, 10296-10308.

(8) Pitzer, K. S. Relativistic effects on chemical properties. *Acc. Chem. Res.* **1979**, *12*, 272-276.

(9) Pyykkö, P.; Desclaux, J. P. Relativity and the periodic system of elements. *Acc. Chem. Res.* **1979**, *12*, 276-281.

(10) Pyykkö, P. Relativistic Effects in Structural Chemistry. *Chem. Rev.* **1988**, *88*, 563-594.

(11) Pyykkö, P.; Johnson, M.; Martinez, T. Relativistic effects in chemistry: more common than you thought. *Annu. Rev. Phys. Chem.* **2012**, *63*, 45-64.

(12) Schwerdtfeger, P.; Bast, R.; Gerry, M.; Jacob, C.; Jansen, M.; Kello, V.; Mudring, A.; Sadlej, A.; Saue, T.; Sohnel, T.; Wagner, F. The quadrupole moment of the 3/2(+) nuclear ground state of Au-197 from electric field gradient relativistic coupled cluster and density-functional theory of small molecules and the solid state. *J. Chem. Phys.* **2005**, *122*.

(13) Mudring, A.; Jansen, M.; Daniels, J.; Kramer, S.; Mehring, M.; Ramalho, J.; Romero, A.; Parrinello, M. Cesiumauride ammonia (1/1), CsAu center dot NH_3: A crystalline analogue to alkali metals dissolved in ammonia? *Angew. Chem. Int. Ed.* **2002**, *41*, 120-124.

(14) Mudring, A.; Jansen, M. Base-induced disproportionation of elemental gold. *Angew. Chem. Int. Ed.* **2000**, *39*, 3066-3067.

(15) Smetana, V.; Lin, Q.; Pratt, D. K.; Kreyssig, A.; Ramazanoglu, M.; Corbett, J. D.; Goldman, A. I.; Miller, G. J. A sodium-containing quasicrystal: using gold to enhance sodium's covalency in intermetallic compounds. *Angew. Chem. Int. Ed.* **2012**, *51*, 12699-12702.

(16) Lin, Q.; Corbett, J. Development of the Ca-Au-In icosahedral quasicrystal and two crystalline approximants: Practice via pseudogap electronic tuning. *J. Am. Chem. Soc.* **2007**, *129*, 6789-6797.

(17) Lin, Q.; Corbett, J. Approximant phases and an icosahedral quasicrystal in the Ca-Au-Ga system: The influence of size of gallium versus indium. *Inorg. Chem.* **2008**, *47*, 7651-7659.

(18) Sinnen, H.-D.; Schuster, H.-U. $Rb_4Au_7Sn_2$, eine intermetallische Phase mit siebenatomigen Goldclustern/ $Rb_4Au_7Sn_2$, an Intermetallic Phase with Sevenatomic Gold-Clusters. *Z. Naturforsch. B* **1981**, *36*, 833.

(19) Zachwieja, U.; Wlodarski, J. $Cs_4Au_7Sn_2$: a gold tin framework structure with Au_7 clusters and Sn_2 dumb-bells. *Z. Anorg. Allg. Chem.* **1998**, *624*, 1443-1446.

(20) Muts, I.; Zaremba, V.; Rodewald, U.; Pottgen, R. Infinite gold zig-zag chains as structural motif in Ca_3Au_3In - A ternary ordered variant of the Ni_4B_3 type. *Z. Anorg. Allg. Chem.* **2008**, *634*, 56-60.

(21) Kriegerbeck, P.; Brodbeck, A.; Strahle, J. Synthesis and structure of K_2Au_3, a new phase in the system potassium gold. *Z. Naturforsch. B* **1989**, *44*, 237-239.

(22) Zachwieja, U. Single-crystal growth and strucrural refinement of KAu_5 and $RbAu_5$. *J. Alloys Compd.* **1993**, *196*, 187-190.

(23) Palasyuk, A.; Grin, Y.; Miller, G. J. Turning gold into “diamond”: a family of hexagonal diamond-type Au-frameworks interconnected by triangular clusters in the Sr–Al–Au system. *J. Am. Chem. Soc.* **2014**, *136*, 3108-3117.

(24) Seidel, S.; Hoffmann, R.-D.; Pöttgen, R. $SrAu_4Ga_3$: a further example with Ga_3 units and a Lonsdaleite-related gold substructure. *Monatsh. Chem.* **2014**, *145*, 1043-1049.

(25) Lin, Q.; Mishra, T.; Corbett, J. D. *J Am. Chem. Soc.* **2013**, *135*, 11023–11031.

(26) Gerke, B.; Hoffmann, R.-D.; Pöttgen, R. Zn_3 and Ga_3 triangles as building units in $Sr_2Au_6Zn_3$ and $Sr_2Au_6Ga_3$. *Z. Anorg. Allg. Chem.* **2013**, *639*, 2444-2449.

(27) Gerke, B.; Pottgen, R. $Sr_2Au_6Al_3$ and $Eu_2Au_6Al_3$ - First Representatives of the $Sr_2Au_6Zn_3$ Type with Aluminum Triangles. *Z. Naturforsch. B* **2014**, *69*, 121-124.

(28) Gerke, B.; Korthaus, A.; Niehaus, O.; Haarmann, F.; Pöttgen, R. Triangular Zn_3 and Ga_3 units in $Sr_2Au_6Zn_3$, $Eu_2Au_6Zn_3$, $Sr_2Au_6Ga_3$, and $Eu_2Au_6Ga_3$ – structure, magnetism, 151Eu Mössbauer and $^{69;71}$Ga solid state NMR spectroscopy. *Z. Naturforsch. B* **2016**, *71*, 567-577.

(29) Zachwieja, U. A new compound in the rubidium gold system - synthesis and structure of Rb_3Au_7. *J. Alloys Compd.* **1993**, *199*, 115-118.

(30) Salamakha, L. P.; Sologub, O. L.; Gonçalves, A. P.; Mudryi, S. I.; Almeida, M. $R(Au_{0.75}Sb_{0.25})_2$ (R = La, Ce, Pr) with UHg_2 structure type, new members of the AlB_2 family. *J. Alloys Compd.* **2007**, *429*, 140-142.

(31) Stoe & Cie GmbH Darmstadt, Germany, 2004.

(32) Blessing, R. H. An empirical correction for absorption anisotropy. *Acta Crystallogr. A* **1995**, *51*, 33-38.

(33) Bruker AXS, I. Madison, WI, 1996.

(34) Sheldrick, G. M. A short history of SHELX. *Acta Crystallogr. A* **2008**, *64*, 112-122.

(35) Kresse, G.; Marsman, M.; Furthmüller, J. *Vienna Ab Initio Simulation Package (VASP), The Guide* Universität Wien, Vienna, Austria, 2010; p.

(36) Kresse, G.; Furthmüller, J. Efficiency of ab-initio total energy calculations for metals and semiconductors using a plane-wave basis set. *J. Comput. Mat. Sci.* **1996**, *6*, 15-50.

(37) Kresse, G.; Furthmüller, J. Efficient iterative schemes for ab initio total-energy calculations using a plane-wave basis set. *Phys. Rev. B* **1996**, *54*, 11169-11186.

(38) Kresse, G.; Hafner, J. Ab initio molecular dynamics for liquid metals. *Phys. Rev. B* **1993**, *47*, 558–561.

(39) Kresse, G.; Joubert, D. From ultrasoft pseudopotentials to the projector augmented-wave method. *Phys. Rev. B* **1999**, *59*, 1758–1775.

(40) Perdew, J. P.; Burke, K.; Ernzenhof, M. Generalized gradient approximation made simple. *Phys. Rev. Lett.* **1996**, *77*, 3865–3868.

(41) Blöchl, P. E. Projector augmented-wave method. *Phys. Rev. B* **1994**, *50*, 17953–17979.

(42) Tank, R.; Jepsen, O.; Burkhardt, A.; Andersen, O. K.; Max-Planck-Institut für Festkörperforschung: Stuttgart, Germany, 1994.

(43) Andersen, O. K.; Jepsen, O. Explicit, first-principles tight-binding theory. *Phys. Rev. Lett.* **1984**, *53*, 2571–2574.

(44) Lambrecht, W. R. L.; Andersen, O. K. Donwfold tech. *Phys. Rev. B* **1986**, *34*, 2439–2449.

(45) Blöchl, P. E.; Jepsen, O.; Andersen, O. K. Tetrahedron method. *Phys. Rev. B* **1994**, *49*, 16223–16233.

(46) Qiu, Y.; Wang, S. Theoretical Investigations of Phosphine-stabilization on Gold Cluster $[Au@Au_8(PR3)_8]^{3+}$ (R=Me, OMe, H, F, Cl, CN). *Chem. J. Chinese U.* **2012**, *33*, 2549-2555.

(47) Wells, D.; Delgass, W.; Thomson, K. Density functional theory investigation of gold cluster geometry and gas-phase reactivity with O-2. *J. Chem. Phys.* **2002**, *117*, 10597-10603.

(48) Cordero, B.; Gomez, V.; Platero-Prats, A. E.; Reves, M.; Echeverria, J.; Cremades, E.; Barragan, F.; Alvarez, S. Covalent radii revisited. *Dalton Trans.* **2008**, 2832-2838.

(49) Lenz, J.; Schubert, K. Crystal structure of $Cu_{10}Sn_3$ (m). *Monatsh. Chem.* **1971**, *102*, 1689-1698.

(50) Lin, Q.; Corbett, J. D. $Ca_{14}Au_{46}Sn_5$: a "colored" $Gd_{14}Ag_{51}$-type structure containing columns of well-differentiated hexagonal gold stars. *Inorg. Chem.* **2011**, *50*, 1808-1815.

(51) Verbovytsky, Y. New ternary phases from the *R*-Au-Ga systems (*R* = Gd-Tm). *Chem. Met. Alloys* **2014**, *7*, 42-55.

(52) Cotton, S. *Lanthanide and Actinide Chemistry*; John Wiley & Sons Ltd: Chichester, 2006; p.

(53) Fischer, P.; Pomjakushin, V.; Keller, L.; Daoud-Aladine, A.; Sikora, W.; Dommann, A.; Hulliger, F. Antiferromagnetic three-sublattice Tb ordering in $Tb_{14}Ag_{51}$. *Phys. Rev. B* **2005**, *72*, 134413.

(54) Tambornino, F.; Sappl, J.; Hoch, C. The $Gd_{14}Ag_{51}$ structure type and its relation to some complex amalgam structures. *J. Alloys Compd.* **2015**, *618*, 326-335.

(55) Smetana, V.; Miller, G. J.; Corbett, J. D. Polyclusters and Substitution Effects in the Na–Au–Ga System: Remarkable Sodium Bonding Characteristics in Polar Intermetallics. *Inorg. Chem.* **2013**, *52*, 12502–12510.

(56) A. Papoian, G.; Hoffmann, R. Hypervalent Bonding in One, Two, and Three Dimensions: Extending the Zintl–Klemm Concept to Nonclassical Electron-Rich Networks. *Angew. Chem. Int. Ed.* **2000**, *39*, 2408-2448.

(57) Jandali, M. Z.; Rajasekharan, T.; Shchubert, K. Crystal structure of $Au_{10}In_3$. *Z. Metallkd.* **1982**, *73*, 463-467.

(58) Schubert, K.; Balk, M.; Bhan, S.; Breimer, H.; Esslinger, P.; Stolz, E. Einige strukturelle Ergebnisse an metallischen Phasen IV. *Naturwissenschaften* **1959**, *46*, 647-648.

(59) Guenzel, E.; Schubert, K. Strukturuntersuchungen im System Kupfer-Antimon. *Z. Metallkd.* **1958**, *49*, 433-439.

(60) Smetana, V.; Corbett, J. D.; Miller, G. J. Four polyanionic compounds in the K−Au−Ga system: a case study in exploratory synthesis and of the art of structural analysis. *Inorg. Chem.* **2012**, *51*, 1695–1702.

(61) Smetana, V.; Miller, G. J.; Corbett, J. D. Three alkali-metal-gold-gallium systems. Ternary tunnel structures and some problems with poorly ordered cations. *Inorg. Chem.* **2012**, *51*, 7711-7721.

(62) Zhang, H.; Borrmann, H.; Oeschler, N.; Candolfi, C.; Schnelle, W.; Schmidt, M.; Burkhardt, U.; Baitinger, M.; Zhao, J.-T.; Grin, Y. Atomic Interactions in the p-Type Clathrate I $Ba_8Au_{5.3}Ge_{40.7}$. *Inorg. Chem.* **2011**, *50*, 1250-1257.

CHAPTER 3

CRYSTAL STRUCTURES AND NEW PERSPECTIVES ON Y_3Au_4 AND $Y_{14}Au_{51}$

Acta Crystallographica Section C Volume: 73 Issue: 9 Pages: 692-696
DOI: https://doi.org/10.1107/S2053229617011068 Published: Sept 2017

Chris Celania[ab], Volodymyr Smetana[ac] and Anja-Verena Mudring[c]*

[a]*The Ames Laboratory, U.S. Department of Energy, Iowa State University, Ames, IA, 50011, USA*

[b]*Department of Materials Science and Engineering, Iowa State University, Ames, IA, 50011, USA*

[c]*Department of Materials and Environmental Chemistry, Stockholm University, Svante Arrhenius väg 16 C, 10 691, Stockholm, Sweden*

Correspondence email: anja-verena.mudring@mmk.su.se

Abstract

Y_3Au_4 and $Y_{14}Au_{51}$, two binary representatives of Au rich rare earth (*R*) systems crystallize hexagonally with the space groups $R\bar{3}$ and *P*6/*m*, adopting the Pu_3Pd_4 and $Gd_{14}Ag_{51}$ structure types, respectively (Pearson symbols *hR*42 and*hP*65). A variety of binary *R*–Au compounds have been reported, although only a few have been investigated thoroughly. Many reports lack information or misinterpret known compounds reported elsewhere. The Pu_3Pd_4 type is fairly common for group 10 elements – Ni, Pd and Pt, while Au representatives are restricted to just five examples – Ca_3Au_4, Pr_3Au_4, Nd_3Au_4, Gd_3Au_4 and Th_3Au_4. Sm_6Au_7 is suspected to be Sm_3Au_4 due to identical symmetry and close unit cell parameters. The Pu_3Pd_4 structure type allows for full substitution of the rare earth's position by more electronegative and smaller elements, i.e. Ti and Zr. The $Gd_{14}Ag_{51}$ type instead is more common for the group 11 metals, while rare representatives of group 12 are known. Y_3Au_4 can be represented as a tunnel structure with encapsulated cations and anionic chains. Though the tunnels are present in $Y_{14}Au_{51}$, this structure is more complex and is best described in terms of polyhedral "pinwheels" around the tunnel forming polyhedra along the *c* axis.

Introduction

Rare earth-gold intermetallics have a rich history dating back almost six decades starting with the discovery of the first binary compounds (Baenziger & Moriarty, 1961). While research on ternary and even quartenary compounds has expanded recently, there still exists a gap in knowledge within some binary systems. These intermetallics often show notable electronic or magnetic properties due to the rare earths, while simultaneously presenting atypical bonding motifs originating from the strong relativistic effects of gold. The contemporary Y-Au binary phase diagram suggests nine compounds exist with varying amount of crystallographic information available. With increasing gold content these structures include: Y_2Au, Y_3Au_2, YAu, YAu RT, Y_3Au_4, YAu_2, YAu_3, $Y_{14}Au_{51}$, and YAu_6 (Chai & Corbett, 2011, Gschneidner *et al.*, 2009, Saccone, Delfino, *et al.*, 1997). Almost all of these structures are found in a large amount of other R-Au systems and adopt a variety of symmetries (orthorhombic, tetragonal, trigonal, hexagonal, and cubic). Of these, Y_3Au_4, $Y_{14}Au_{51}$, and YAu_6 have no reported detailed structural investigation (except of symmetry check and structure type suggestion), while Y_3Au_2 and YAu RT are missing from the only binary phase diagram available (Saccone, Delfino, *et al.*, 1997).

Researchers at Los Alamos Scientific Laboratory first synthesized Pu_3Pd_4 in 1973 (Cromer *et al.*, 1973), and since then, much of the research has focused on representatives with group 10 elements such as Pd and Pt. The structure has been stabilized with various rare earths as well as actinides such as Th (Palenzona & Cirafici, 1986) and (obviously) Pu. Within the confines of rare earth-gold compounds, full structural data via single crystal analysis has only been reported for Nd_3Au_4 (Fornasini & Saccone, 1994, Saccone *et al.*, 1999). However, the phase has been preliminarily identified in Y-Au, Pr-Au, Gd-Au, and suggested of Sm-Au systems (Saccone *et al.*, 1996, Saccone, Maccio, *et al.*, 1997, Mazzone *et al.*, 2009). While the majority of members within the structure type contain rare earth elements, the possibility of other active metal formation with

gold has been confirmed with Ca_3Au_4, (Henry & Weller, 1999), opening wider horizons for possible substitutions.

The $Gd_{14}Ag_{51}$ structure type, in contrast, has more literature data available. The structure itself has significantly more representatives and closely related phases due to various ternary compounds possible via anion mixing, and various crystallographically similar amalgams (Tambomino *et al.*, 2015, McMasters *et al.*, 1971). Certain $R_{14}Au_{51}$ compounds (namely $Nd_{14}Au_{51}$ and $Pr_{14}Au_{51}$) have also been shown to have some form of phase width away from being strict line compounds (Saccone, Maccio, *et al.*, 1997, Saccone *et al.*, 1999, Mazzone *et al.*, 2009). Forming with a majority of the rare earths and gold, there is a full structural report available for every known $R_{14}Au_{51}$ compound except $Y_{14}Au_{51}$.

Experimental Procedure

1. Synthesis and crystallization

Starting materials used for synthesis were Au (99.98 %), and rare earth elements (99.9 %) from the Materials Preparation Center, U.S. Dept. of Energy, Ames Laboratory. New representatives of both the Pu_3Pd_4 and $Gd_{14}Ag_{51}$ structure types were observed in the Y-Au system as the major phase and minor phase in samples loaded with in a 3:5 and 2:7 rare earth:Au ratio. The Y-Au samples were pre-reacted at 1000°C followed by a weeklong anneal at 700°C to obtain better quality single crystals. Total mass of the samples were 0.3g each. Due to the rare earth components, the sample was handled under inert conditions using standard inert gas techniques such as utilization of dry gloveboxes.

Samples were first loaded at the composition previously listed into a Ta tube in the form of turnings from filing or pieces cut to a similarly small size. The tube was then sealed by arc welding in Ar atmosphere, followed by jacketing in fused silica under vacuum. Temperatures near (but slightly below) the melting point of gold were used to ensure full reactions while discouraging

Ta-Au binary formation. The sample appeared dark gray with a metallic luster, and remained stable weeks later.

2. Refinement

X-ray powder diffraction was performed on the sample by a STOE STADI P diffractometer with a STOE image plate detector with Cu $K_{\alpha 1}$; λ = 1.54059 Å (Si as an internal standard, a = 5.4308(1) Å). Powder preparation included grinding of brittle samples, then sieving to < 38μm particles, and dispersion onto vacuum grease between Mylar© sheets and fixed by Al rings. Data analysis was completed with the *WinXPow 3.06* software package (Stoe & Cie GmbH, 2004).

The sample was crushed in a die press and single crystals were selected and affixed to a glass fiber with grease. All single crystal data, collection methods, and other structure refinement information are listed in Table 1. Upon initial observation of the unit cell parameters of the Y_3Au_4 sample, a similarity to those of the rare earth-gold binary Nd_3Au_4 was noticed. Systematic absences suggested *R*3 and $R\bar{3}$ as potential space groups and further structure refinement confirmed $R\bar{3}$ as the correct option showing its isotypic nature to Nd_3Au_4 and parent structure Pu_3Pd_4. All positions also appear fully occupied. Systematic absences within the $Y_{14}Au_{51}$ sample proposed $P\bar{3}$, *P*3, $P\bar{6}$, *P*6, as well as the correct space group *P*6/*m*, isotypic to $Gd_{14}Ag_{51}$.

Results and discussion

The atom packing in Y_3Au_4 is best described in terms of a tunnel structure. When viewed along the *c* axis, a gold net featuring tunnels becomes apparent (Figure 1a). *R* atoms form triangles within the tunnels and are centered by a one dimensional infinite chain of Au atoms. A comparable network structure has been described for Ca_3Au_3In (Muts *et al.*, 2008), in which an anionic network of Au and In housed triangles of a cation, which, in turn, are centered by zig-zag chains of gold. Similarly, BaPt (Karpov *et al.*, 2004) displays hexagonal cation nets of Ba housing an anionic

infinite platinum chain through the center. However, BaPt does not display the outer anion network described in the prior structures mentioned and exhibit strong Pt–Pt bonding, which is not present in the electron richer Y_3Au_4 structure. The latter may then be viewed as a combination of motifs from both BaPt and Ca_3Au_3In structures. The outer anionic net within Y_3Au_4 is still somewhat unique compared to both others though, and further reflection revealed an interesting pattern. Au atoms forming the tunnel walls are naturally segmented into structures resembling molecules of cyclooctane in the chair conformation (Figure 1b, 1c).

The four crystallographic sites in Y_3Au_4 are composed of three gold and one yttrium position. Both Au2 and Au3 sites exhibit $Au@Y_6Au_2$ bicapped trigonal antiprisms (CN = 8) while Au1 is situated in an odd 10-coordinated site. The $Au@Y_7Au_3$ polyhedron is best described as an equatorially four-capped trigonal prism. The Y site's coordination is a $Y@Au_8Au_1$ distorted rectangular prism capped by an additional Au atom (Figure A8a). When applied across the structure, the Y coordination polyhedra share faces with each other to create a space-filling network (Figure 2 *left*). A stacking sequence for this network was discovered along [5, 4, 7] in an a-b-c-c'-b'-a' pattern, in which the Au3 site capping the distorted rectangular prism rotates to face each relative axis direction (Figure 2 *right*).

The $Y_{14}Au_{51}$ structure contains ten crystallographic sites, three corresponding to Y and the other seven to Au. A recognizable trait of the $Gd_{14}Ag_{51}$ structure type is found in the Au5 site of $Y_{14}Au_{51}$. A disordered position forming hexagons about the *c* axis are 50% occupied to instead form Au5 triads (Figure 3 *left*) due to the creation of unrealistically short Au5-Au5 distances between adjacent members of the hexagon (Table 1S). These triads are then statistically disordered, or otherwise would form a superstructure as seen in some amalgam structures (Tambomino *et al.*, 2015). However, no evidence of such a superstructure were indicated by X-ray diffraction data in this work. Similar to Y_3Au_4, $Y_{14}Au_{51}$ consists of a three-dimensional anionic

network around the rare earth positions, whose coordination polyhedra (Figure A8b) connect to form a stacking structure. Unlike Y_3Au_4 however, the yttrium coordination polyhedra do not connect to form a space-filling representation (Figure 3 *right*). The coordination polyhedron of the Y3 site incorporates the six half occupied Au5 sites and shares faces to polyhedra above and below forming interpenetrating Frank-Kasper (FK) polyhedra with the appearance of having a coordination number (CN) of 18, but formally 15 when only a triad of Au5 are occupied. When viewed along the *c* axis, these polyhedra are surrounded by the other polyhedra forming multi-polyhedral pinwheels throughout the structure. The Y1 and Y2 polyhedra make up hexagonal slabs around the Y3 sites. The Y1 site has CN 14 and connects to other polyhedra in three different forms. Y1 polyhedra share edges between other Y1 polyhedra within the slab, and share faces with the Y2 polyhedra slabs above and below while sharing vertices with the Y3 polyhedra in the center of the pinwheel. One half-occupied Au5 site is a part of the Y1 coordination environment. Therefore, the Y1 polyhedron possesses CN 14 when the site is occupied and shares a face with the Y3 polyhedron. Otherwise, Y1 CN is 13 and its polyhedron shares only edges with the latter. This contributes to the inability to form a space-filling representation of the structure via coordination polyhedra.

The single crystal X-ray diffraction data for both compounds in this work is in agreement with the powder X-ray diffraction data derived from the preliminary phase analysis of the Y-Au system (Saccone, Delfino, *et al.*, 1997). Various $R_{14}Au_{51}$ single crystal data are available, allowing structural comparison, however, $Gd_{14}Au_{51}$ presents an advantageous choice because of the similar metallic radii of Gd and Y. Caveats within the atomic distances involve the disordered Au5 position are accepted across the series of $Gd_{14}Ag_{51}$ type compounds. Distances between adjacent Au5 sites are unrealistically short ~1.5 Å, while those between atoms directly across from each other are somewhat long ~3.1 Å. Both are ignored due to the formal 50% occupancy of the site.

The one Au5 site within the *R*2 coordination polyhedra also forms a noticeably short *R*-Au distance across the series. Exempting these three distances, the Au-Au and Y-Au distances range from 2.734(7)– 3.064(1) Å (covalent sum of 2.88 Å) and 3.018(1) – 3.251(1) Å (covalent sum of 3.22 Å) respectively (Table 1S). Comparatively, Au-Au and Gd-Au distances from $Gd_{14}Au_{51}$ are all in line with these values, though on average slightly larger (~30 pm), which is common between other Gd/Y-Au intermetallics(McMasters *et al.*, 1971).

A logical next step is a comparison of Y_3Au_4 to a counterpart, such as Nd_3Au_4, of which single crystal and atomic distance data is available (Fornasini & Saccone, 1994), and in which the interatomic distances are quite similar to those of Y_3Au_4 (~15 pm for Au-Au, but ~100 pm for *R*-Au) (Table 1S). Within Y_3Au_4 we see Au-Au distances range of 2.974(1)–3.0578(9) Å (covalent sum of 2.88 Å), and Au-Y ranges of 2.881(2)–3.275(2) Å (covalent sum of 3.22 Å); however, the upper edge of the latter is the least populated. Average distances for Y_3Au_4 are shorter due to its lower orbital shell. However, Au-Au and Au-*R* distances within both samples are within expected values from other rare earth and gold intermetallics (Chai & Corbett, 2011, Gschneidner *et al.*, 2009). The addition of the full crystallographic data via single crystal refinement allows for better comparison between compounds within Pu_3Pd_4 and $Gd_{14}Ag_{51}$ structure types as well as the reevaluation of anionic networks or other structural motifs within for new perspectives.

Table 1. Crystal data and collection information for both Y_3Au_4 and $Y_{14}Au_{51}$ samples. Experiments were carried out with Mo *K*α radiation. Empirical (using intensity measurements), Blessing, 1995. Computer programs: (APEX3, 2015, SAINT, 2015, Krause et al., 2015, Brandenburg, 2006, Sheldrick, 2015b, a)

Crystal data		
Chemical formula	Au_4Y_3	$Au_{51}Y_{14}$
M_r	1054.60	11290.03
Crystal system, space group	Trigonal, $R\bar{3}$:*H*	Hexagonal, *P*6/*m*
Temperature (K)	296	293
a, *b*, *c* (Å)	13.3664 (15), 13.3664 (15), 5.9640 (9)	12.5433 (17), 12.5433 (17), 9.1389 (14)
α, β, γ (°)	90, 90, 120	90, 90, 120
V (Å^3)	922.8 (2)	1245.2 (4)
Z	6	1
μ (mm^{-1})	122.83	165.57
Crystal size (mm)	0.09 × 0.07 × 0.07	0.06 × 0.05 × 0.05
Data collection		
Diffractometer	Bruker Venture	Bruker Venture
T_{min}, T_{max}	0.0, 0.0	0.0, 0.0
No. of measured, independent and observed [$I > 2\sigma(I)$] reflections	3552, 722, 567	12877, 1075, 994
R_{int}	0.102	0.054
$(\sin\theta/\lambda)_{max}$ (Å^{-1})	0.764	0.660
Refinement		
$R[F^2 > 2\sigma(F^2)]$, $wR(F^2)$, *S*	0.047, 0.094, 1.04	0.022, 0.044, 1.13
No. of reflections	722	1075
No. of parameters	25	62
$\Delta\rho_{max}$, $\Delta\rho_{min}$ (e Å^{-3})	4.07, −3.91	2.26, −2.50

Table 2. Atomic positions and all atomic displacement parameters for both Y_3Au_4 and $Y_{14}Au_{51}$.

Y_3Au_4

Atom	Wyck.	x	y	z	U
Au1	18*f*	0.39424(5)	0.11583(5)	0.0443(1)	0.0080(2)
Au2	3*a*	0	0	0	0.0248(5)
Au3	3*b*	0	0	1/2	0.0246(4)
Y4	18*f*	0.0433(1)	0.2136(1)	0.2266(3)	0.2266(3)

Atom	U_{11}	U_{22}	U_{33}	U_{23}	U_{13}	U_{12}
Au1	0.0086(3)	0.0077(3)	0.0082(3)	0.0002(2)	0.0007(2)	0.0046(3)
Au2	0.0096(5)	0.0096(5)	0.055(1)	0	0	0.0048(3)
Au3	0.0230(6)	0.0230(6)	0.028(1)	0	0	0.0115(3)
Y4	0.0069(7)	0.0120(8)	0.0079(7)	-0.0021(6)	-0.0012(5)	0.0047(6)

$Y_{14}Au_{51}$

Atom	Wyck.	x	y	z	U
Au1	12*l*	0.10246(6)	0.44233(6)	0.33622(8)	0.0064(1)
Au2	12*l*	0.26716(6)	0.07682(6)	0.23267(8)	0.0058(1)
Au3	12*l*	0.49383(6)	0.11646(6)	0.15145(7)	0.0063(1)
Au4	6*k*	0.05845(9)	0.23781(9)	1/2	0.0046(1)
Au5	6*j*	0.0281 (2)	0.1388(2)	0	0.0075(3)
Au6	4*h*	1/3	2/3	0.3098(1)	0.0060(2)
Au7	2*c*	1/3	2/3	0	0.0094(2)
Y1	6*k*	0.4652(2)	0.1409(2)	1/2	0.0039(3)
Y2	6*j*	0.1133(2)	0.3921(3)	0	0.0104(3)
Y3	2*e*	0	0	0.3026(5)	0.0034(5)

Atom	U_{11}	U_{22}	U_{33}	U_{23}	U_{13}	U_{12}
Au1	0.0060(2)	0.0039(2)	0.0069(2)	0.0017(2)	-0.0008 (2)	0.0008(2)
Au2	0.0045(2)	0.0066(2)	0.0072(2)	0.0018(2)	0.0023(2)	0.0035(2)
Au3	0.0028(2)	0.0078(2)	0.0066 (2)	0.0010 (2)	0.0001(2)	0.0014(2)
Au4	0.0015(3)	0.0063(3)	0.0061(3)	0	0	0.0019(2)
Au5	0.0138(7)	0.0032(5)	0.0058(5)	0	0	0.0046(5)
Au6	0.0035(2)	0.0035(2)	0.0110(3)	0	0	0.0017 (1)
Au7	0.0093(3)	0.0093(3)	0.0097(5)	0	0	0.0046(2)
Y1	0.0030(7)	0.0037(7)	0.0053(7)	0	0	0.0020(6)
Y2	0.0084(8)	0.0214(9)	0.0054(7)	0	0	0.0103(7)
Y3	0.0016(7)	0.0016(7)	0.007(1)	0	0	0.0008(3)

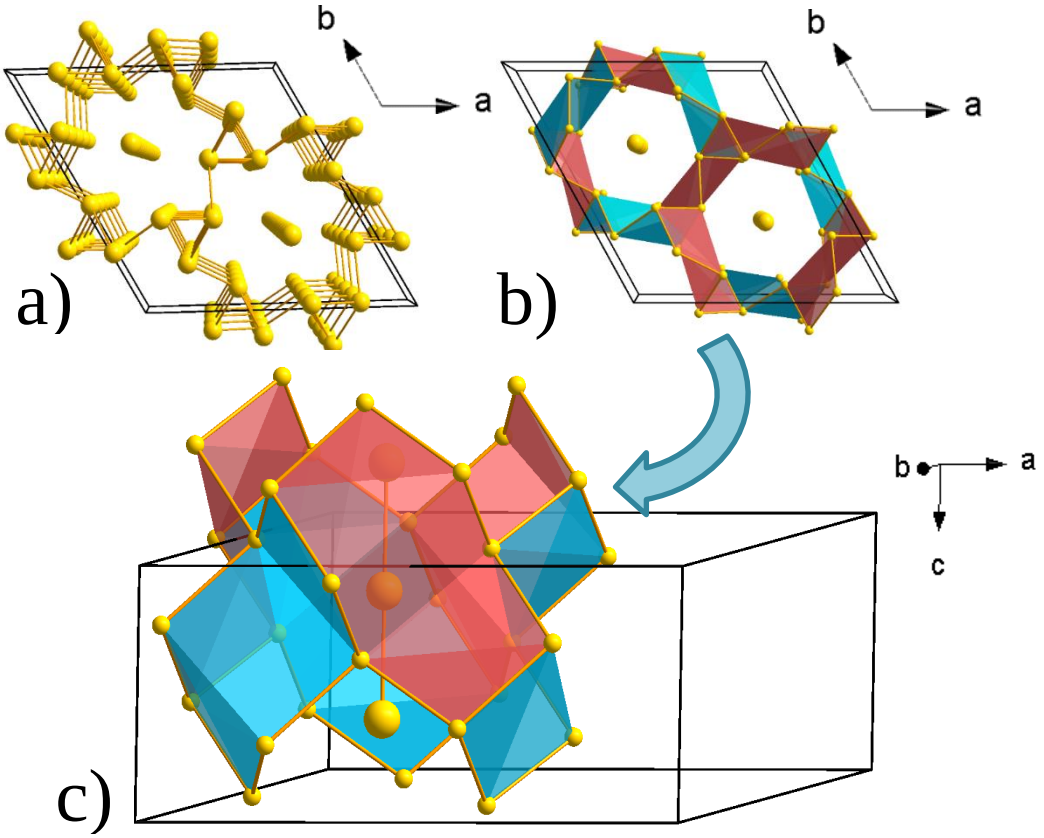

Figure 1. The anionic network forms gold nets surrounding hexagons of rare earth cations (removed for clarity) centered by infinite one dimensional Au chains (a.). Alternatively viewed, the anion networks are linked segments of Au similar to chair configuration cyclooctane (b. and c.).

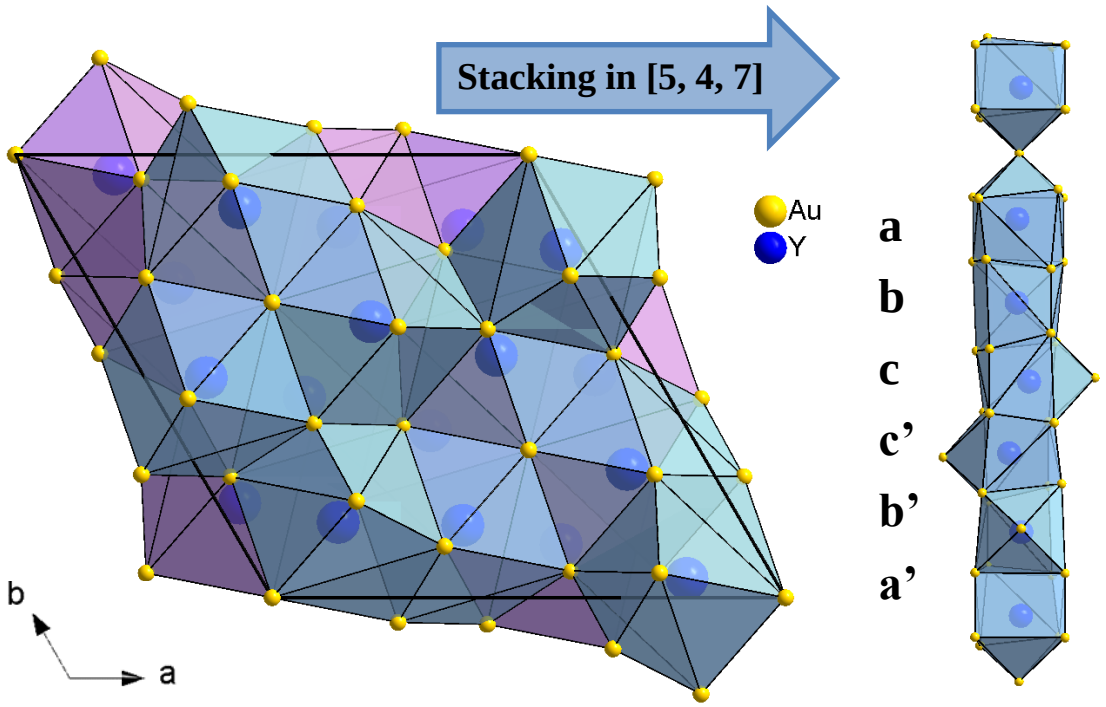

Figure 2. When all Y coordination polyhedra are represented, they connect to form a space filling network of face-sharing polyhedra that can be described as slabs (left). However, as the purple slab layer demonstrates, these slabs are irregular and interpenetrate at several locations. The stacking sequence (a, b, c, c', b', a') of the Y coordination polyhedra becomes resolved when viewed along [5, 4, 7] direction (right).

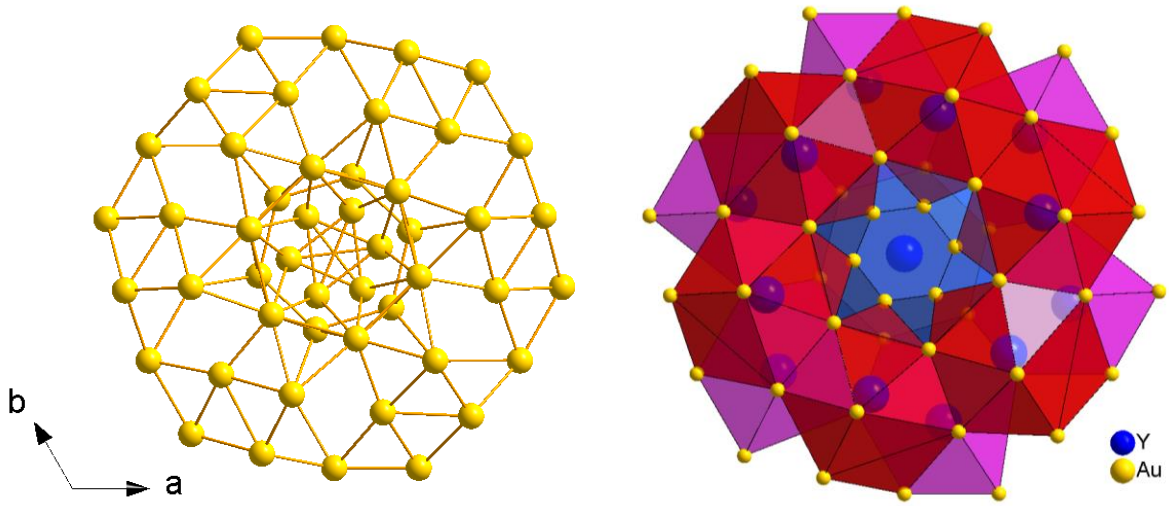

Figure 3. Pinwheel pattern of both the anionic lattice (left) and the rare earth coordination polyhedra (right) within $Y_{14}Au_{51}$. The half-filled, disordered Au site has been left fully occupied for clarity, forming the innermost hexagon of atoms in each. Y1 polyhedra are shown in magenta, Y2 in red, and Y3 in blue.

Information in Appendix

A table of interatomic distances for both Y_3Au_4 and $Y_{14}Au_{51}$ samples; Images of the coordination polyhedra for all sites in Y_3Au_4 and all Y sites in $Y_{14}Au_{51}$.

Acknowledgements

The research was supported by the Office of the Basic Energy Sciences, Materials Sciences Division, U.S. DOE. Ames Laboratory is operated for DOE by Iowa State University under Contract DE-AC02-07CH11358.

Synopsis Image and Information

The crystal structures of Y_3Au_4 and $Y_{14}Au_{51}$ have been investigated using single crystal X-ray diffraction.

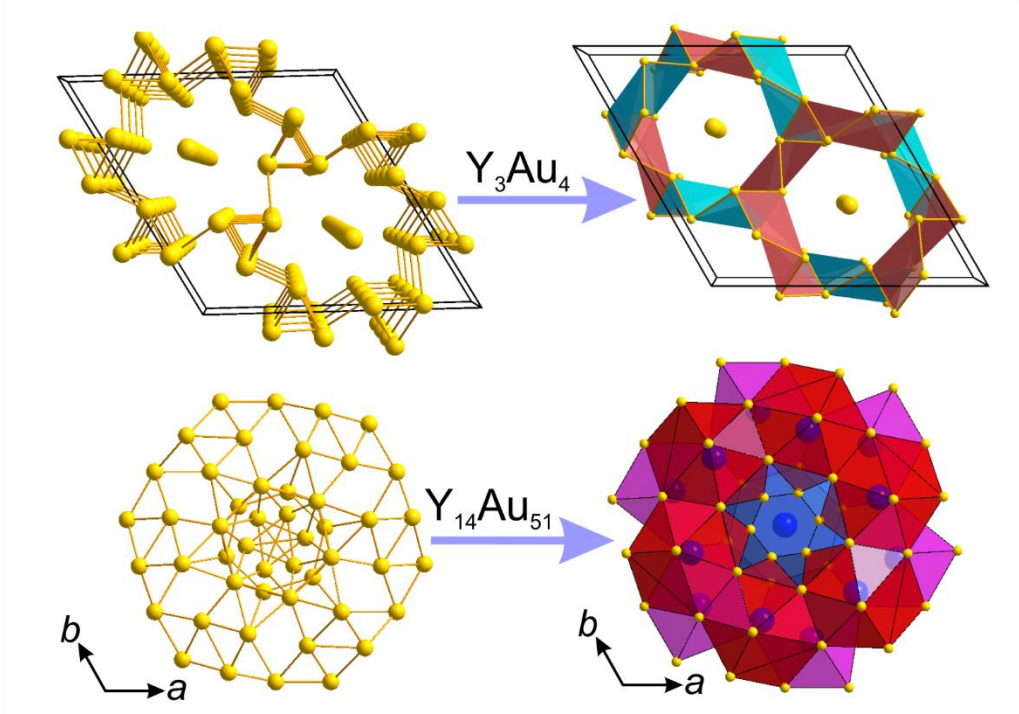

References

APEX3. (2015).

Baenziger, N. & Moriarty, J. (1961). *Acta Crystallogr.* **14**, 946-947.

Brandenburg, K. (2006). *DIAMOND.*

Chai, P. & Corbett, J. (2011). *Acta Crystallogr. C* **67**, I53-I55.

Cromer, D., Larson, A. & Roof, R. (1973). *Acta Crystallogr. B* **B 29**, 564-567.

Fornasini, M. & Saccone, A. (1994). *Z. Kristallogr.* **209**, 657-659.

Gschneidner, K., Mudryk, Y., Becker, A. & Larson, J. (2009). *Calphad* **33**, 8-10.

Henry, P. & Weller, M. (1999). *J. Alloys Compd.* **292**, 152-155.

Karpov, A., Nuss, J., Wedig, U. & Jansen, M. (2004). *J. Am. Chem. Soc.* **126**, 14123-14128.

Krause, L., Herbst-Irmer, R., Sheldrick, G. & Stalke, D. (2015). *J. Appl. Crystallogr.* **48**, 3-10.

Mazzone, D., Marazza, R., Riani, P., Zanicchi, G., Cacciamani, G., Fornasini, M. & Manfrinetti, P. (2009). *Calphad* **33**, 31-43.

McMasters, O., Gschneidner, K., Bruzzone, G. & Palenzona, A. (1971). *J. Less Common Met.* **25**, 135-160.

Muts, I., Zaremba, V., Rodewald, U. & Pottgen, R. (2008). *Z. Anorg. Allg. Chem.* **634**, 56-60.

Palenzona, A. & Cirafici, S. (1986). *J. Less Common Met.* **124**, 245-249.

Saccone, A., Delfino, S., Maccio, D. & Ferro, R. (1997). *J. Chim. Phys. Phys.-Chim. Biol.* **94**, 948-957.

Saccone, A., Fornasini, M., Maccio, D. & Delfino, S. (1996). *Intermetallics* **4**, 111-119.

Saccone, A., Maccio, D., Delfino, S. & Ferro, R. (1999). *Metall. Mater. Trans. A* **30**, 1169-1176.

Saccone, A., Maccio, D., Giovannini, M. & Delfino, S. (1997). *J. Alloys Compd.* **247**, 134-140.

SAINT. (2015).

Sheldrick, G. (2015a). *Acta Crystallogr. A* **71**, 3-8.

Sheldrick, G. (2015b). *Acta Crystallogr. C* **71**, 3-8.

Stoe & Cie GmbH (2004). Darmstadt, Germany.

Tambomino, F., Sappl, J. & Hoch, C. (2015). *J. Alloys Compd.* **618**, 326-335.

CHAPTER 4

R_{14}(Au, M)$_{51}$ (R = Y, La-Nd, Sm-Tb, Ho, Er, Yb, Lu; M = Al, Ga, Ge, In, Sn, Sb, Bi): STABILITY RANGES AND SITE PREFERENCE IN THE $Gd_{14}Ag_{51}$ STRUCTURE TYPE

Submitted to Crystal Growth & Design October 2017

Chris Celania, [†,‡] Volodymyr Smetana, [†,∥] Alessia Provino, [†,§,⊥] Pietro Manfrinetti, [†,§,⊥] Anja-Verena Mudring [†,‡,∥*]

[†]*The Ames Laboratory, U.S. Department of Energy, Iowa State University, Ames, IA 50011, USA*

[‡]*Department of Materials Science and Engineering, Iowa State University, Ames, IA 50011, USA*

[∥]*Department of Materials and Environmental Chemistry, Stockholm University, Svante Arrhenius väg 16 C, 106 91 Stockholm, Sweden*

[§]*Department of Chemistry, University of Genova, Via Dodecaneso 31, 16146 Genova, Italy*

[⊥]*Institute SPIN-CNR, Corso Perrone 24, 16152 Genova, Italy*

Abstract

Twenty new ternary representatives of the $Gd_{14}Ag_{51}$ structure type have been synthesized within the R-Au-M family (R = Y, La-Nd, Sm-Tb, Ho, Er, Yb, Lu; M = Al, Ga, Ge, In, Sn, Sb, Bi) using standard solid state synthesis techniques. The list of post-transition metals (M) involved in the formation of this type of structure has been augmented by five new representatives. All compounds crystallize in the hexagonal space group $P6m$ (#175) with the unit cell ranges of a = 12.3136(2) – 12.918(1) Å and c = 8.9967(3) – 9.385(1) Å, and incorporate different degrees of Au/M mixing. The involvement of the post-transition element in the structure varies from one to another compound both qualitatively and quantitatively. A rather significant phase width can be expected for the majority of compounds, however, not without exclusions. The distribution of the post-transition metals within the structure has been analyzed via single crystal X-ray diffraction. While the positional disorder of one near-origin Au position is expectable for all compounds due to steric reasons, two specimens show an obvious deviation from the others including another Au position split along the c axis. Possible factors affecting this behavior have been discussed.

Introduction

Gold is well known for its flexibility in chemical bonding and formation of notable structural features, which finds its origin in the strong relativistic influence on its 5*d* and 6*s* valence orbitals. This renders gold an exciting component in the exploration of new intermetallic compounds.[1-8] The varied bonding capabilities and size of gold also provide a prime opportunity for the incorporation of slight structural changes akin to the substitution of various group 13-15 elements. Examples of gold's flexibility in structure and bonding are numerous, including the formation of quasicrystals, their approximants and related crystalline formations with crystallographically forbidden symmetries, along with various homoatomic gold assemblies.[8-12] Such motifs comprise isolated Au_7 clusters as found in $A_4Au_7X_2$ (*A* = K, Rb, Cs; *X* = Ge, Sn),[13,14] one dimensional columns such as Au zig-zag chains like in Ca_3Au_3In,[15] and two dimensional slabs, which are observable in K_2Au_3.[16] Three dimensional gold networks also form in several arrangements: interconnected trigonal bipyramids are found in KAu_5,[17] hexagonal diamond-like frameworks of Au are the characteristic structural motifs in the *Ae*-Au-*Tr* (*Ae* = alkaline earth, *Tr* = triel element) systems,[18-24] and assemblies of tetrahedral and square planar Au fragments are observed in Rb_3Au_7.[25]

Rare earth intermetallic compounds with gold have received much research interest in the last few years, with shifting attention towards the exploration of gold-rich regions of the systems.[20,26-31] Various compounds within these systems show exciting or rare structural motifs and a variety of often useful magnetic and electronic properties such as the magnetocaloric effect, ferromagnetism, superconductivity, thermoelectricity, etc. Compounds with rare earths are regarded for their diverse magnetic properties, which they owe to the unpaired spins provided by their well-shielded 4*f* electrons. By moving down the series of rare earth elements, various magnetic moments and atomic sizes become available, permitting an intriguing alteration of magnetic interaction.

The gold-rich section of the *R*-Au-*M* family remains a particularly interesting region for further exploration. The high content of gold allows for a higher chance of homoatomic formations and more opportunities to explore the variety of Au–Au bonding and to investigate the capability of group 13–15 elements to stabilize the structures and to affect such formations. For example, substitution of gold by a post-transition metal *M* may allow the stabilization of ternary compounds where certain binary compounds have not been reported. Of these compounds, much recent research has focused on ternary compounds with tin and has led to the discovery of the $R_3Au_6Sn_5$,[32,33] $R_3Au_4Sn_3$,[32] $R_5Au_8Sn_5$,[32] $R_4Au_7Sn_4$,[32] $R_2Au_5Sn_2$[26] and $R_3Au_7Sn_3$ series of compounds,[27,28] The latter can be described as superstructural polyhedral packing of ZrBeSi-type featuring a new homoatomic Au cluster, $Au@Au_6$. Recent work also led to the discovery of a compositionally and structurally related series R_3Au_9Pn.[34] The R_3Au_9Pn structure contains $Au@Au_6$ trigonal antiprisms and stacking features similar to those found in $R_{14}Au_{51}$ structures that are not present in the $R_3Au_7Sn_3$ structure, acting as a bridge between the $Gd_{14}Au_{51}$ and $Cu_{10}Sn_3$ parent structure types. However, gold rich systems in combination with rare earth elements and group 13–15 elements are still largely underexplored, showing specific scarcity with compounds featuring pnictogens (*Pn*, group 15) aside from the previously mentioned work. Because of the structural and compositional similarities between R_3Au_9Pn series and the $Gd_{14}Ag_{51}$ structure type, exploration of samples at the *R*:Au:*M* compositional ratio of 3:9:1 with rare earth and group 13–15 metal variation often yielded more thermodynamically stable $R_{14}(Au, M)_{51}$.

Reports first identified the $Gd_{14}Ag_{51}$ structure type under the formula of Ag_3Gd in 1968 and further refined it to the formal structure type in 1970 with representatives spanning the near entirety of the rare earths.[35,36] The structure falls under space group *P*/6*m* (175) and ranges in size from $Hf_{14}Cu_{51}$ (a = 11.18 Å, c = 8.25 Å) to $Sr_{14}Hg_{51}$ (a = 13.78 Å, c = 9.88 Å).[37,38] The structure type has come under increased study in the past decade (specifically within ternary compounds) resulting in numerous representatives of the type and its derivative structures.[39,40] Reported

compounds have displayed actinide mixing in $U_7Th_7Au_{51}$;[41,42] group 11 mixing between Cu, Ag, and Au in $Dy_{14}Ag_{42.3}Cu_{8.7}$, $U_{14}Au_{42}Ag_9$, and $U_{14}Ag_{42}Cu_9$;[43,44] and group 11 and group 13-14 element mixing with focus on Cu–Ga ranging from $Gd_{14}Cu_{48}Ga_3$ to $Sc_{14}Cu_{36.7}Ga_{14.3}$.[45,46] *R*-Au-*M* (*R* = rare earth, *M* = groups 13-15) representatives have only recently been reported solely for Ga and Sn.[47,48] Though studied more recently in detail, a consensus on how site mixing and coloring occurs within these ternary compounds does not appear to exist[47,49,50] and the numerous *R*-Au-*M* compounds studied within this work shed more light on this phenomenon.

Experimental Section

1. Synthesis.

Starting materials used for synthesis were Au (99.98 %), rare earth elements (99.9 %) and group 13-15 elements Al, Ga, Ge, In, Sn, Bi (99.99 %) from the Materials Preparation Center, Ames Laboratory, and Sb (99.99%) from Alfa Aesar. Extra Au and Bi were obtained from MaTeck (99.99%) and Alfa Aesar (99.999%) respectively. A representative of the R_{14}(Au, M)$_{51}$ series was first observed in the Gd-Au-Sb system as a minor phase in a sample loaded with Gd:Au:Sb in a 2:5:1 ratio. The sample was reacted in a sealed tantalum ampule jacketed in fused silica at 1000°C for 3 hours, followed by annealing at 850°C for 12 hours. Different synthetic conditions were then tested at loaded (*R*:Au:*M*) 3:9:1 compositions in order to explore the R_3Au_9Pn series, often yielding R_{14}(Au, M)$_{51}$ as the majority phase product. Investigation spanned the breadth of the rare earths (Y, La–Nd, Sm–Lu tested with Au and Sb) as well as various group 13-15 elements (Al, Ga, In, Sn, Sb, and Bi tested with Gd and Au). This constitutes the majority of included compounds. However, R_{14}(Au, M)$_{51}$ compounds discovered through other, unrelated *R*-Au-*M* explorations loaded at different Au-rich compositions have also been included for a more comprehensive overview (Gd:Au:Sb and Yb:Au:Sn at 3:7:3 and Er:Au:Ga, Ce:Au:Ga, and Lu:Au:Ga at 14:34.1:16.9). Regardless of loaded composition, the general strategy was to react the starting

materials at high temperatures (either by heating in an electrical-resistance furnace until at least one component reached the liquid state or by arc melting), followed by annealing at lower temperature to create higher quality single crystals for X-ray structure analysis. Total mass of samples prepared was 0.5g. All samples were handled under inert conditions using standard techniques.

Samples to be arc melted were first formed into pellets using a die press to combine the starting materials (as small chunks or filings) with two metric tons of force. Because of the low melting points and high vapor pressures of some group 13-15 elements, ~6% extra mass was added to the loaded compositions to account for loss during the process. These elements were strategically loaded on one side of the pellet so that it could be placed out of direct contact with the arc to discourage vaporization. Arc melting occurred in short bursts (~5 seconds or until buttons appeared fully molten) in an inert Ar environment. Between subsequent melts, buttons were flipped (three to four times in total) to improve homogeneity. Samples were sealed in tantalum tubes (under inert Ar atmosphere by arc welding) followed by fused silica jackets (under vacuum) before annealing at 850°C in a tube furnace.

Samples to be formed by high-temperature self-flux reactions in furnaces were first loaded at *R*:Au:*M* stoichiometric ratios into Ta tubes, which were then sealed by arc welding in Ar followed by jacketing in fused silica under vacuum. To ensure full reactions while discouraging Ta-Au binary formation, temperatures slightly under the melting point of the main component (Au) were used. The fully molten *M* component and high surface-area-to-volume ratio of the other components (small chunks or filings) encouraged reactivity. All samples, despite synthesis technique, appeared dark gray with a metallic luster, and remained stable weeks later.

2. X-Ray Analysis.

X-ray powder diffraction for phase analysis was performed on samples by either a STOE STADI P diffractometer with a STOE image plate detector with Cu $K_{\alpha 1}$; λ = 1.54059 Å (Si as an internal standard, a = 5.4308(1) Å). For powder preparation the brittle samples were ground, then sieved to < 38μm particles, and dispersed onto either vacuum grease sandwiched between Mylar© sheets and fixed by Al rings. Data analysis was performed with the *WinXPow 3.06* software package.[51]

Scanning electron microscopes (SEM) were used for characterization of microstructure and homogeneity for several representatives of the series. A Leica Cambridge 360 equipped with an Oxford X-Max 20 analyzer (for Energy Dispersive X-ray analysis, EDS) allowed for semi-quantitative elemental analysis. Utilizing a high-tension voltage of 20.0 kV, distinct phases were recognized and further analyzed via EDS to identify the phase composition (counting time of 60 s). The $Pr_{14}(Au, Sb)_{51}$ sample was analyzed with a JEOL JSM 6060LV (20.0 kV and counting time of 160 sec). With the accuracy within 1 at.%, the data allow for verification of the estimated compositions by the single crystal method.

For single X-ray diffraction, samples were crushed in a die press and single crystals were selected under a microscope and then affixed to a glass fiber with grease. Single crystal x-ray diffraction took place at room temperature on either a Bruker APEX CCD diffractometer or a Bruker D8 VENTURE diffractometer (both with Mo K_{α} radiation; λ = 0.71073 Å), utilizing the APEX 2 and APEX 3 software suites (for the former and the latter diffractometer, respectively) for data collection, integration, polarization, and empirical absorption correction.[52,53] Scans ranged 2θ values of ~3-63°. The SHELXTL suite and XPREP algorithms within were used to check for extinction conditions and E statistics in the intensity data sets necessary for the assignment of the proper $P6/m$ space group. Direct methods were used for structure solution (SHELXS-97).[54] APEX

3 software was then used to carry out full structure refinement (refining atomic positions, determining mixed site occupancies and anisotropic displacement parameters).

Results and Discussion

Pursuit of R_3Au_9Pn within the wider realm of the *R*-Au-*M* systems produced numerous ternary representatives of the compositionally similar $R_{14}(Au, M)_{51}$ phases. These compounds exhibit variation in overall composition as well as Au/*M* site mixing despite parallel elemental ratios and synthesis conditions. Representatives of $R_{14}(Au, M)_{51}$ compounds comprise *R* = Y, La–Nd, Sm–Tb, Ho, Er, Yb, Lu; *M* = Al, Ga, Ge, In, Sn, Sb, Bi, including $Yb_{14}(Au, Sn)_{51}$, and $Lu_{14}(Au, Ga)_{51}$, which are ternary representatives with no reported binary phase, as well as a replication of the recently reported $Er_{14}(Au, Ga)_{51}$ ternary representative for comparison[47]. The details of the crystallographic investigation along with the positional data are summarized in Tables 1 and 2.

1. Crystal Chemistry.

The crystal structure of the $R_{14}(Au, M)_{51}$ compounds accounts for ten independent crystallographic sites, three of which being occupied by the rare earths. The coordination polyhedra of these three rare earth positions (Figure 1) build up a layered structure (Figure 2). A characteristic feature of the structure is the Au7 site, which forms hexagons centered around the *c* axis. Due to Au-Au short distances (~1.6 Å), these sites are only half-filled and practically form triangles. In the case of $Gd_{14}Ag_{51}$ structures, these triangles are statistically disordered, while ordering is observed in structurally related amalgam structures[39,55-57]. Independent refinement of this position results in 50(1) % occupancy for the binary compounds[40]. The occupancy for Au7 has been fixed at 50% to explore Au/*M* mixing at this site. This disordered site is highlighted in the top and bottom planes of the face-sharing double coordination polyhedra for the *R*2 sites displayed in Figure 2(a) (with coordination number (CN) 15 instead of CN 18). The *R*3

coordination polyhedra form the top and bottom slabs of the layered structure via face sharing (Figure 2(b)) and incorporate the disordered position by forming either 13 or 14 atom coordination polyhedra depending on the conformation of the triangle of the partially filled Au7 sites. A second slab of *R*1 coordination polyhedra (CN 14) share edges with the *R*2 face-sharing double polyhedra and share faces with the *R*3 polyhedra slabs above and below.

While almost all compounds in this report adopt minor modifications of the basic $Gd_{14}Ag_{51}$ structure type through alterations in bond lengths, one noticeable difference occurs in the La-Au-Bi and Lu-Au-Ga ternary representatives. The Au6 site within this structure becomes disordered, creating a secondary position ~0.5 Å offset along the *c* axis (see Table 2). The coordination polyhedra of this site for both structures are represented in Figure 3, with unoccupied positions as black spheres for clarity. The comparatively small radii of Lu and Ga create a noticeably small unit cell for the Lu-Au-Ga representative of the series. When the Ga6A site is occupied (Figure 3(a), *right*) the distance to adjacent Au6 sites lengthens to 3.540 Å, which appears unreasonably long. Simultaneously, a short Ga6A-Au5 distance of only 2.488 Å forms. While uncommon, shorter distances are reported in other Au-Ga compounds.[11] For La-Au-Bi, the expanded structure leads to an unreasonably long Au6-Au6 distance (3.870 Å), reducing the coordination polyhedra regardless of if the disordered position is occupied. The Bi6A disordered site has an occupancy of 17% over the normal Au6 site, but occupation of this Bi6A site appears problematic as it forms an unrealistically short Bi6A–Au5 distance of 2.233 Å. However, a complementary occupancy of 82% is noted for the Au5 site, representing an absence in both the Au5 and Au6 sites when the Bi6A site is occupied (Figure 3(b), *right*). The origin of this disorder is speculated to stem from size effects, as it only appears present in a sample with a large *R* element mixed with a large *M* element, and a sample with a small *R* element mixed with a small *M* element. However, future experimentation or theoretical calculations may elucidate this.

A similar disorder is seen in the related amalgam $Eu_{10}Hg_{55}$ structure.[55] Because of the ordering of the split Au7 position, the system moves into the $P\bar{6}$ structure type. Additionally, the *R*2 site becomes a mixed Eu/Hg position (accounting for the composition change). Aside from these differences, both the Au5 and Au6 positions appear disordered along the *c* axis. The disordered positions are more nearly equidistant between their original site and the nearest above/below, and are approximately 50% occupied.

The full list of discovered ternary gold intermetallics organized by rare earth and then post-transition metal components is presented in Table 3. Three values are listed for Gd-Au-Sb that were taken from samples loaded from different starting Au-rich compositions for comparison. The $Er_{14}(Au, Ga)_{51}$ compound, though already reported in literature, was replicated to confirm Au-Ga mixing is possible at each Au crystallographic site as described and will be discussed further. As a note, testing a second crystal from the same $Er_{14}(Au, Ga)_{51}$ sample showed comparable mixing percentages in the same sites. This asserts that the single crystal data within this work are representative of site preference and not stochastic for all sites.

Deviations from reported binary cell volumes range from -1.9% to +3.3% with substitutions typically increasing the unit cell size despite Bi being the only tested *M* element with a noticeably larger covalent radius than Au.[58] In fact, the largest cell volume increase is noted for the $Ho_{14}(Au, Sn)_{51}$ sample despite not having an exceptional amount of post-transition metal mixed into the gold sites. Another example of tin's ability to expand the structure is found in $Yb_{14}(Au, Sn)_{51}$, which contains a large amount of tin, and is the only heavy rare earth element example with unit cell volume over 1300 $Å^3$. Ho-Au/Sn interatomic distances for coordination polyhedra range from 3.066 – 3.311 Å (excepting a short 2.846 Å distance connecting the R3 position to the disordered Au7 site when forming the 14-atom coordination polyhedra), approaching the sum of the Ho and Au covalent radii of 3.180 Å. Au/Sn-Au/Sn distances show a similar variance, ranging from 2.718 – 3.218 Å (ignoring the distance well under 2 Å between two adjacent disordered Au7

sites). These values are shorter than, and longer than the Au-Au covalent radii summation of 2.880 Å respectively, but are not unheard of values within gold intermetallics.[59]

While there is no known binary for unit cell volume comparison, the smallest cell is found in $Lu_{14}(Au, Ga)_{51}$. This is due not only to small radius of Lu, but also significant mixing of Au with smaller Ga atoms. In fact, this sample has the highest concentration of post-transition metal of the list of tested compounds. Aside from those distances involved with the extra disordered position that was discussed above, short distances between Au/Ga sites exist between Au2-Au2 sites (2.541 Å) and Au1-Au4 sites (2.645 Å). However, neither are exceptionally short within the literature.[11,60] And more generally, atomic *R*-Au, Au-Au, and Au-*M* distances within all other samples appear within expected values from literature from their respective fields of intermetallics.[61-63]

SEM images with EDS analysis of La-Au-Bi, Pr-Au-Sb, Nd-Au-Ga, Sm-Au-Bi, and Lu-Au-Ga samples (Figure A9 and Table A4 respectively) are in agreement with atomic compositions predicted from refinements of single crystals, and support claims that samples in this report are in fact ternary representatives, and not simply the reported binary phases. Atomic phase width reported for the $Pr_{14}Au_{51}$ binary phase (as well as within a ternary representative: $Pr_{14}(Au, Sn)_{51}$) allows for slightly more gold-rich compositions than expected from the line composition.[48] EDS elemental values from the report on the R_3Au_9Pn structure describe a secondary phase labeled as "$Tb_{14}(Au, Sb)_{51}$," which are also within 1 at% of the composition designated for the Tb-Au-Sb sample by the single crystal refinement data of this work. In the cases of Gd-Au-Sn, Ho-Au-Ge, and Ho-Au-Sb, powder X-ray diffraction shows representatives of the $R_{14}(Au, M)_{51}$ structure are forming in these systems. This is further supported by SEM/EDS analysis, which also supplies overall compositions.

The degree of Au/*M* site mixing is summarized in Table 3. The overall amount of the *M* component within the composition varies greatly from only 0.5 % in $Nd_{14}Au_{50.7}Sb_{0.3}$ to 24.2 % in

$Lu_{14}Au_{35.3}Ga_{15.7}$. While, the amount of overall *M* within the phase may be limited by the starting composition as well as if other phases were present, there is some indication of available phase widths. This point is emphasized by the three Gd-Au-Sb samples that stemmed from three different starting compositions (multiphase samples starting from Gd:Au:Sb ratios of 3:9:1 to 3:7:3) that show increasing overall Sb mixing from 4.2% – 8.6%. Single crystal refinements of these separate samples all show mixing in sites Au6 and Au7. The most Sb-rich crystal appears to fully occupy the Au6 site with Sb before allowing mixing to take place in a third location, the Au4 site. The majority of samples were synthesized from a 3:9:1 *R*:Au:*M* ratio (7.8% *M*), and yet over half of the R_{14}(Au, *M*)$_{51}$ compounds contain less than this amount of M (~$R_{14}Au_{46}M_5$). This proposes that a maximum phase width has been reached for those samples. A trend of high Au/*M* mixing stood out for Ga samples, prompting testing at higher concentrations (the Er-Au-Ga and Lu-Au-Ga samples). These high-Ga samples were used as a comparison to an $Er_{14}Au_{34.1}Ga_{16.9}$ sample reported by Verbovytskyy that conveyed mixing in all seven Au sites, as determined by powder X-ray diffraction analysis.[47] While the starting composition may be limiting in some cases, this report covers samples with overall *M* of up to 24.2%, and yet none of the samples displayed Au/*M* mixing in all seven sites simultaneously, as described in Verbovytskyy's report. Lu_{14}(Au, Ga)$_{51}$, with its extensive mixing, is also the only sample that refines mixing into the Au1 site. For comparison, the Nd_{14}(Au, Sb)$_{51}$ sample with only 0.5% overall Sb showed small amounts of mixing in two sites. Three samples with Bi (La_{14}(Au, Bi)$_{51}$, Sm_{14}(Au, Bi)$_{51}$, and Gd_{14}(Au, Bi)$_{51}$), display another trend: low Au/Bi mixing. Each sample displays mixing in only one site, which is different for each of the three samples.

It should also be noted that in all but three samples, refinement data propose mixing in the half occupied, disordered Au7 site. The three outliers are all samples that include Bi, which is slightly larger than Au. Even after the Au7 hexagons have been ordered into triangles, there are still relatively short Au-Au bonds (~2.70 Å) across the series. Substitution of Au with smaller

atoms (or similar sized atoms that still create favorable heteroatomic bonds) may alleviate the local energy of this site. The literature appears inconsistent with its allowance of mixing at this disordered atomic site. In the work previously mentioned by Verbovytskyy, mixing was determined by powder x-ray diffraction to exist at all seven sites, including the disordered Au7,[47] while in recent works by Belgacem et al. and Lin and Corbett, mixing at this site is discounted.[49] A disordered Er site in the $Er_{14}Cu_{51-x}Ga_x$ ($5.5 \leq x \leq 11.0$) compound reported by Belgacem et al. that is near the Au7 site would have likely shown preferential occupancy if the Au7 site showed mixing.[50] No analogous disordered rare earth site is present in the samples of this work. Other works do not discuss individual site mixing in detail, and assume mixing in all sites based on the overall starting composition of the samples.[45,46,64]

Statistical analysis of data within Table 3 was attempted in order to draw structural and mixing relationships. Factors analyzed include: Size of *R* and *M* atoms, Valence Electron Count (VEC), ΔV from binary structures, overall %*M* in samples, and individual site mixing. No direct relationships between the parameters listed were unraveled due to the limited data set available. Such interactions may be determined if a larger data set (systematic testing of possible *R*-Au-*M* combinations with multiple replications) were available. On the other hand, site preference for Au/*M* mixing within a given system may be better understood by performing theoretical structure calculations such as total energies analysis for each possible combination.

Summary

A series of *R*-Au-*M* ternary representatives of the $Gd_{14}Ag_{51}$ structure have been investigated, greatly expanding on the list of known representatives as well as post-transition metal options for gold-site mixing. Twenty-one unique representatives are reported while including multiple crystals within samples for phase width comparison. All adhere to the *P*/6*m* space group and are

isostructural to $Gd_{14}Ag_{51}$, barring the Lu-Au-Ga and La-Au-Bi samples, which have an additional disordered Au site. When occupied, the new position alters coordination polyhedra, as well as forces a complementary vacancy with a nearby gold site. The addition of post-transition metals stabilized the structure of $Lu_{14}(Au, Ga)_{51}$ and $Yb_{14}(Au, Sn)_{51}$, for which no binaries have been reported. Overall post-transition metal mixing ranged from 0.5% to 24.2% of the total composition between samples. Of the seven Au sites, mixing took place at a minimum of one and a maximum of five within each sample (covering all seven sites across the structure). This work allowed for mixing within the half-filled, disordered Au7 and, found that all but three samples refined mixing on this site, showing a strong preference for it. While more systematic testing across the family with repetition may further elucidate size and electronic trends for mixing at individual sites, this work certainly includes mixing data on the greatest number of elemental combinations for ternary $Gd_{14}Ag_{51}$ representatives within one report, and may act as a platform for future understanding.

Table 1. Crystallographic details and refinement parameters for $Gd_{14}(Au, Sb)_{51}$, $Lu_{14}(Au, Ga)_{51}$, and $La_{14}(Au, Bi)_{51}$. For all structures: hexagonal, P6/m. Experiments were carried out with Mo Kα radiation with empirical absorption correction.

	Gd-Au-Sb	**Lu-Au-Ga**	**La-Au-Bi**
Crystal data			
Chemical formula	$Au_{48.27}Gd_{14}Sb_{2.73}$	$Au_{35.30}Ga_{15.70}Lu_{14}$	$Au_{49.93}Bi_{0.70}La_{14}$
M_r	12041.21	10497.10	11925.56
Temperature (K)	296	293	297
a, *c* (Å)	12.6929 (5), 9.2006 (5)	12.3233 (4), 8.9664 (3)	12.918 (1), 9.385 (1)
V (Å^3)	1283.7 (1)	1179.24 (9)	1356.1 (3)
Z	1	1	1
μ (mm−1)	156.43	147.02	147.38
Crystal size (mm)	0.1 × 0.1 × 0.1	0.1 × 0.1 × 0.1	0.1 × 0.1 × 0.1
Data collection			
Diffractometer	Bruker CCD	Bruker Venture	Bruker Venture
T_{min}, T_{max}	0.1, 0.2	0.1, 0.2	0.1, 0.2
No. of measured, independent and observed [$I > 2\sigma(I)$] reflections	11869, 681, 541	13515, 1231, 997	38695, 1404, 1274
R_{int}	0.122	0.090	0.111
θ_{max} (°)	23.5	30.0	30.0
$(\sin\theta/\lambda)_{max}$ (Å^{-1})	0.56	0.703	0.703
Refinement			
$R[F^2 > 2\sigma(F^2)]$, $wR(F^2)$, *S*	0.027, 0.057, 1.01	0.031, 0.060, 1.09	0.027, 0.055, 1.17
No. of reflections	681	1231	1404
No. of parameters	63	66	64
$\Delta\rho_{max}$, $\Delta\rho_{min}$ (e Å^{-3})	2.34, −3.22	4.33, −4.93	3.75, −3.42

Table 2. Atomic position and site occupancy data for three representative samples. Filled mixed sites are designated as M while a disordered split position unique to the Lu-Au-Ga and La-Au-Bi samples is designated as *M*6A.

	$Gd_{14}Au_{48.3}Sb_{2.7}$				$Lu_{14}Au_{35.3}Ga_{15.7}$				$La_{14}Au_{49.9}Bi_{0.7}$			
	x	***y***	***z***	**Occ.**	***x***	***y***	***z***	**Occ.**	***x***	***y***	***z***	**Occ.**
***R*1**	0.4627(2)	0.1392(2)	1/2		0.13413(7)	0.46549(8)	1/2		0.14246(8)	0.46760(8)	1/2	
***R*2**	0	0	0.3083(3)		0	0	0.3017(2)		0	0	0.30167(17)	
***R*3**	0.1163(2)	0.3936(2)	0		0.39266(9)	0.12020(8)	0		0.39268(13)	0.11926(10)	0	
Au1	0.10199(9)	0.44196(9)	0.3387(1)		0.07155(6)	0.26917(6)	0.22642(7)	0.762(5)	0.07235(4)	0.26868(4)	0.23752(5)	
***M*1**					0.07155(6)	0.26917(6)	0.22642(7)	0.238(5)				
Au2	0.0590(1)	0.2377(1)	1/2		0.2292(1)	0.0587(1)	1/2	0.464(6)	0.23858(5)	0.06035(5)	1/2	
***M*2**					0.2292(1)	0.0587(1)	1/2	0.536(6)				
Au3	0.49142(9)	0.11140 (9)	0.1513(1)		0.44488(5)	0.11326(5)	0.33656(6)		0.44025(4)	0.10250(4)	0.33498(5)	
***M*3**												
Au4	0.26716(9)	0.07549(9)	0.2335(1)		0.10893(7)	0.49172(7)	0.14548(9)	0.553(4)	0.11118(4)	0.49308(4)	0.15141(5)	
***M*4**					0.10893(7)	0.49172(7)	0.14548(9)	0.447(4)				
Au5	1/3	2/3	0		1/3	2/3	0		1/3	2/3	0	0.814(6)
Au6	1/3	2/3	0.2998(2)	0.53(2)	1/3	2/3	0.3277(5)	0.379(7)	1/3	2/3	0.2938(3)	0.830(6)
***M*6**	1/3	2/3	0.2998(2)	0.48(2)								
***M*6A**					1/3	2/3	0.2775(8)	0.621(7)	1/3	2/3	0.238(1)	0.170(6)
Au7	0.0313(3)	0.1394(3)	0	0.36(1)	0.1351(2)	0.0326(3)	0	0.203(6)	0.1412(1)	0.0345(1)	0	1/2
M7	0.0313 (3)	0.1394(3)	0	0.14(1)	0.1351(2)	0.0326(3)	0	0.297(6)				

Table 3. Lattice parameters, cell volume (as well as comparison to reported binary compounds) a summary of individual site mixing data for all R_{14}(Au, M)$_{51}$ single crystal data from this work (except for those cases labeled with "N/A" where SCXRD was not performed). *Composition verified with EDS †Lattice parameters verified with PXRD (see Tables A4 and A5)

Compound	Lattice Parameters		V_{obs} [Å^3]	ΔV%	%*M* Mixing at Au Site						
	a [Å]	*c* [Å]			**1**	**2**	**3**	**4**	**5**	**6**	**7**
$Y_{14}Au_{47.1}Sb_{3.9}$	12.638(2)	9.215(2)	1274.7(4)	1.3						75	29
*$La_{14}Au_{49.9}Bi_{0.7}$	12.918(1)	9.385(1)	1356.1(3)	0.7						17	
$Ce_{14}Au_{42.6}Ga_{8.4}$	12.750(1)	9.262(1)	1304.0(3)	-1.6		34	25		11	62	22
$Ce_{14}Au_{47.8}Sb_{3.2}$	12.869(1)	9.332(1)	1338.5(3)	1					50	28	19
*$Pr_{14}Au_{48.7}Sb_{2.3}$	12.820(2)	9.3043(2)	1324.4(5)	0.8						41	23
*†$Nd_{14}Au_{45.6}Ga_{5.4}$	12.680(2)	9.212(1)	1282.6(4)	-1.3		40		8	58		28
$Nd_{14}Au_{50.7}Sb_{0.3}$	12.743(2)	9.276(1)	1304.5(4)	0.2					5		6
*$Sm_{14}Au_{49.4}Bi_{1.6}$	12.7260(5)	9.2403(4)	1296.0(1)	0.9					11		
$Gd_{14}Au_{44.5}Al_{6.5}$	12.5613(5)	9.1195(3)	1246.2(1)	-1.6		48	13		87		8
$Gd_{14}Au_{43.0}Ga_{7.0}$	12.553(1)	9.112(1)	1243.5(3)	-1.9		50		10	73	7	35
$Gd_{14}Au_{48.65}In_{2.35}$	12.686(1)	9.1727(9)	1278.5(3)	0.9			8			15	28
*†$Gd_{14}Au_{46.9}Sn_{4.1}$	12.6958(1)	9.1960(1)	1283.7(1)	1.3				N/A			
$Gd_{14}Au_{48.3}Sb_{2.7}$	12.6929(5)	9.2006(5)	1283.7(1)	1.3						47	28
$Gd_{14}Au_{48.0}Sb_{3.0}$	12.692(2)	9.215(2)	1285.5(4)	1.5						51	33
$Gd_{14}Au_{45.4}Sb_{5.6}$	12.706(2)	9.217(2)	1288.7(4)	1.7				6		99	34
$Gd_{14}Au_{46.7}Bi_{4.3}$	12.642(2)	9.195(2)	1272.7(4)	0.4				34			
$Tb_{14}Au_{49.1}Sb_{1.9}$	12.638(4)	9.172(4)	1268.6(1)	1		4				26	21
*†$Ho_{14}Au_{45.3}Ge_{5.7}$	12.4888(2)	9.0812(3)	1226.64(4)	-1.5				N/A			
$Ho_{14}Au_{48.2}Sn_{2.8}$	12.710(2)	9.196(2)	1286.7(4)	3.3		11				37	23
*†$Ho_{14}Au_{45.1}Sb_{5.9}$	12.6192(1)	9.1869(1)	1267.0(1)	1.8				N/A			
$Er_{14}Au_{39.9}Ga_{11.1}$	12.406(1)	9.029(1)	1203.4(3)	N/A		45	41			64	48
$Yb_{14}Au_{37.8}Sn_{13.2}$	12.8315(4)	9.2435(4)	1318.0 (1)	N/A		30	36	32		50	36
*†$Lu_{14}Au_{35.3}Ga_{15.7}$	12.3233(4)	8.9664(3)	1179.24(9)	N/A	24	54		45		62	59

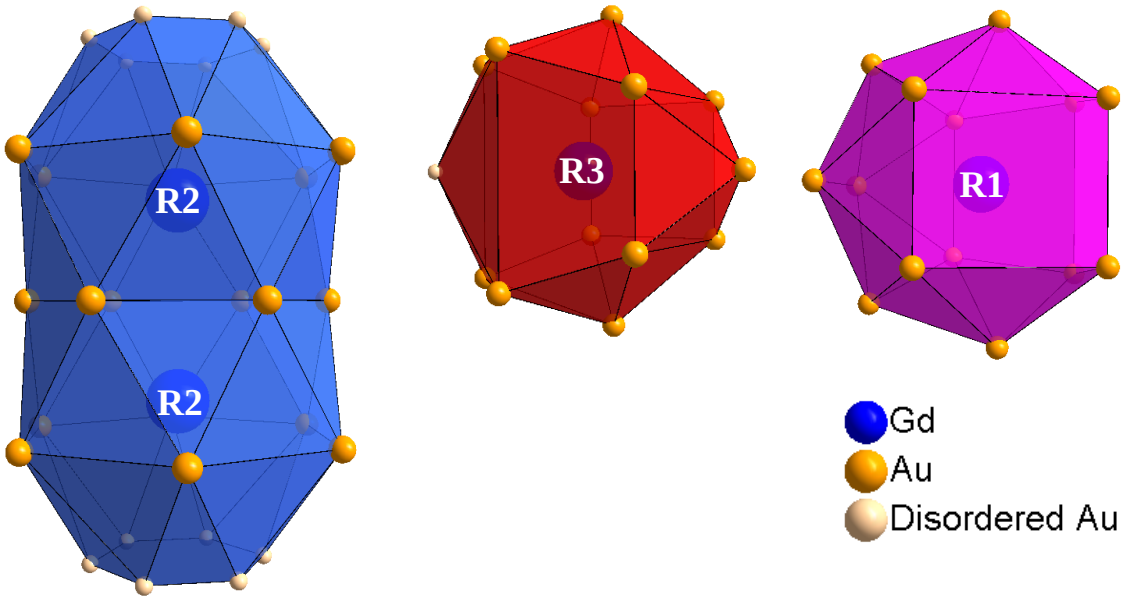

Figure 1. Coordination polyhedra for the three rare earth sites R1-R3 in $Gd_{14}Au_{51}$. The disordered half-filled Au7 position is highlighted in the R2 and R3 polyhedra for clarity. Because of its occupancy, R2 sites are coordinated by only 15 atoms, and R3 sites are coordinated by 13 or 14 Au atoms depending on if the Au7 site is occupied.

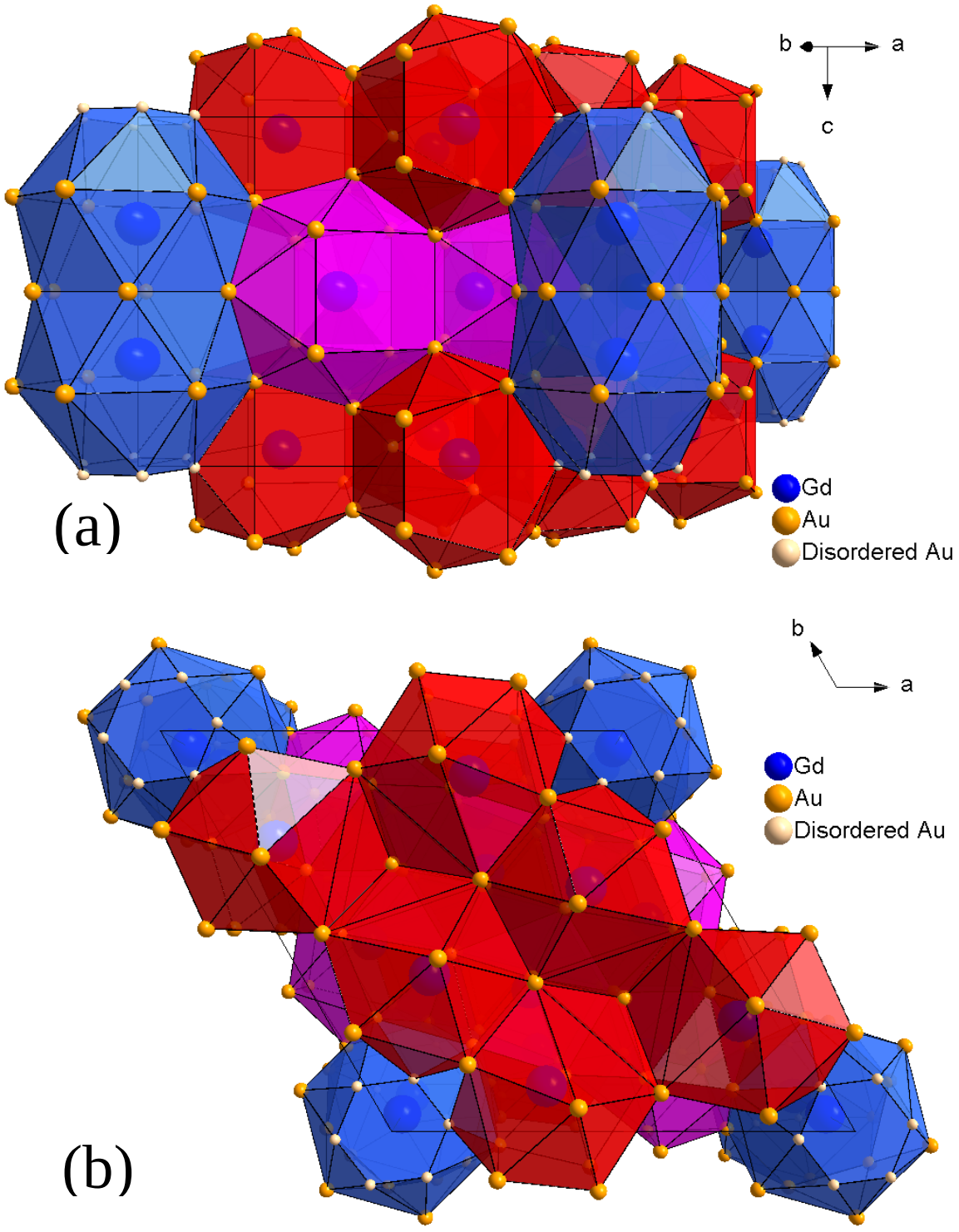

Figure 2. Side and top perspectives ((a) and (b) respectively) of the polyhedral packing within $Gd_{14}Au_{51}$ made up of the three Gd sites' coordination polyhedra. The disordered, half-filled Au7 site is highlighted in tan for clarity. Polyhedra form face and edge sharing slabs around columns of interpenetrating Frank-Kasper polyhedra (shown in blue).

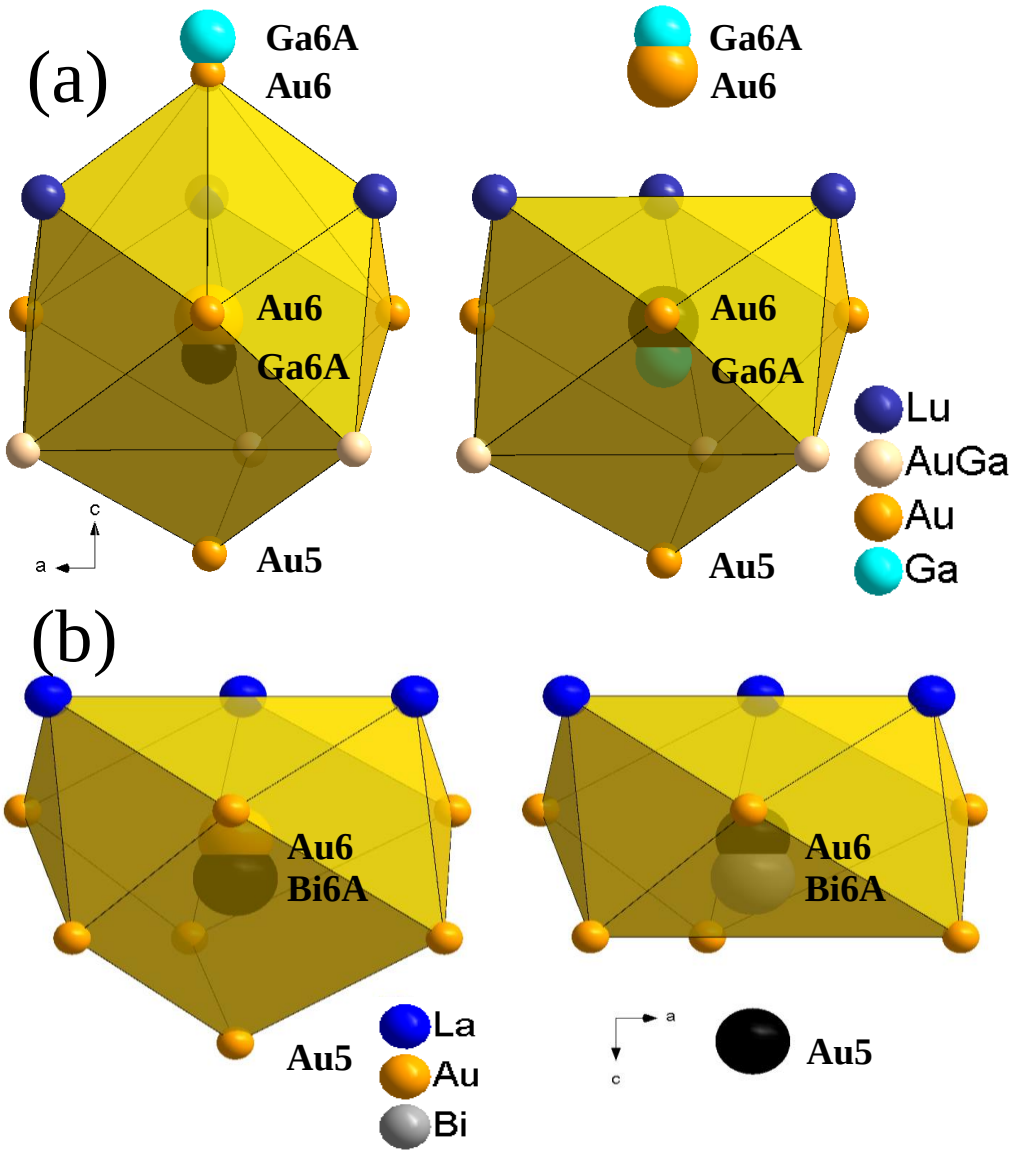

Figure 3. A representation of the additional split position located in the La-Au-Bi and Lu-Au-Ga samples where unoccupied sites are displayed as black spheres. The shorter unit cell for Lu-Au-Ga and Ga's significantly smaller radii to that of Au, create an unreasonably long Au5-Ga6A distance (~3.5 Å) when Ga6A is occupied (A right). While the Ga6A-Au5 distance is short (~2.5 Å), it is not unheard of. When the Bi6A site is occupied (B right), a short Bi6A-Au5 distance is formed, however, we see a complementary vacancy in the Au5 site. Au6-Au6 lengths also increase significantly to unreasonable lengths (~3.9 Å).

Information in Appendix

SEM/EDS data for eight samples; a representative single-phase powder X-ray diffraction pattern for Gd-Au-In; an alternate perspective of the $R_{14}Au_{51}$ structure.

Accession codes

The following table defines the CCDC numbers associated with the supplementary crystallographic data for the compounds described in this paper. These data can be obtained free of charge via www.ccdc.cam.ac.uk/data_request/cif, or by emailing data_request@ccdc.cam.ac.uk, or by contacting The Cambridge Crystallographic Data Centre, 12 Union Road, Cambridge CB2 1EZ, UK; fax: +44 1223 336033.

Compound	**CCDC #**	**Compound**	**CCDC #**	**Compound**	**CCDC #**
$Y_{14}Au_{47.1}Sb_{3.9}$	1581777	$Gd_{14}Au_{44.5}Al_{6.5}$	1581765	$Tb_{14}Au_{49.1}Sb_{1.9}$	1582101
$La_{14}Au_{49.9}Bi_{0.7}$	1581775	$Gd_{14}Au_{44.0}Ga_{7.0}$	1581780	$Ho_{14}Au_{48.2}Sn_{2.8}$	1582098
$Ce_{14}Au_{42.6}Ga_{8.4}$	1581764	$Gd_{14}Au_{48.65}In_{2.35}$	1581779	$Er_{14}Au_{39.9}Ga_{11.1}$	1581769
$Ce_{14}Au_{47.8}Sb_{3.2}$	1581774	$Gd_{14}Au_{48.3}Sb_{2.7}$	1581767	$Yb_{14}Au_{37.8}Sn_{13.2}$	1581773
$Pr_{14}Au_{48.7}Sb_{2.3}$	1581771	$Gd_{14}Au_{48.0}Sb_{3.0}$	1581781	$Lu_{14}Au_{35.3}Ga_{15.7}$	1582099
$Nd_{14}Au_{45.6}Ga_{5.4}$	1582100	$Gd_{14}Au_{45.4}Sb_{5.6}$	1581766		
$Nd_{14}Au_{50.7}Sb_{0.3}$	1581770	$Gd_{14}Au_{46.7}Bi_{4.3}$	1581768		
$Sm_{14}Au_{49.4}Bi_{1.6}$	1581772				

Acknowledgments

The research was supported by the Office of the Basic Energy Sciences, Materials Sciences Division, U.S. DOE. Ames Laboratory is operated for DOE by Iowa State University under Contract DE-AC02-07CH11358.

Synopsis Image and Text

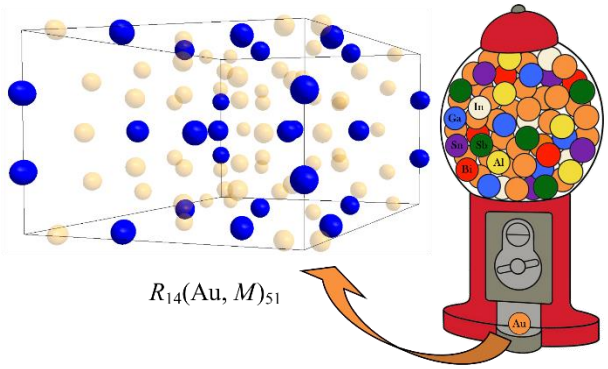

The structure stability and site preference of the R_{14}(Au, M)$_{51}$ as a function of the rare earth and post-transition elements combinations, including the addition of twenty new ternary representatives. A new type of disorder found within La_{14}(Au, Bi)$_{51}$ and Sm_{14}(Au, Bi)$_{51}$ systems is also discussed.

References

(1) Pitzer, K. S. *Acc. Chem. Res.* **1979**, *12*, 272-276.

(2) Pyykkö, P.; Desclaux, J. P. *Acc. Chem. Res.* **1979**, *12*, 276-281.

(3) Pyykkö, P. *Chem. Rev.* **1988**, *88*, 563-594.

(4) Pyykkö, P.; Johnson, M.; Martinez, T. *Annu. Rev. Phys. Chem.* **2012**, *63*, 45-64.

(5) Schwerdtfeger, P.; Bast, R.; Gerry, M.; Jacob, C.; Jansen, M.; Kello, V.; Mudring, A.; Sadlej, A.; Saue, T.; Sohnel, T.; Wagner, F. *J. Chem. Phys.* **2005**, *122*.

(6) Mudring, A.; Jansen, M.; Daniels, J.; Kramer, S.; Mehring, M.; Ramalho, J.; Romero, A.; Parrinello, M. *Angew. Chem. Int. Ed.* **2002**, *41*, 120-124.

(7) Mudring, A.; Jansen, M. *Angew. Chem. Int. Ed.* **2000**, *39*, 3066-3067.

(8) Smetana, V.; Rhodehouse, M.; Meyer, G.; Mudring, A. V. *Acc. Chem. Res.* **2017**, *Accepted*.

(9) Smetana, V.; Lin, Q.; Pratt, D. K.; Kreyssig, A.; Ramazanoglu, M.; Corbett, J. D.; Goldman, A. I.; Miller, G. J. *Angew. Chem. Int. Ed.* **2012**, *51*, 12699-12702.

(10) Lin, Q.; Corbett, J. *J. Am. Chem. Soc.* **2007**, *129*, 6789-6797.

(11) Lin, Q.; Corbett, J. *Inorg. Chem.* **2008**, *47*, 7651-7659.

(12) Smetana, V.; Corbett, J. D.; Miller, G. J. *J. Solid State Chem.* **2013**, *207*, 21-28.

(13) Sinnen, H.-D.; Schuster, H.-U. *Z. Naturforsch. B* **1981**, *36*, 833.

(14) Zachwieja, U.; Wlodarski, J. *Z. Anorg. Allg. Chem.* **1998**, *624*, 1443-1446.

(15) Muts, I.; Zaremba, V.; Rodewald, U.; Pottgen, R. *Z. Anorg. Allg. Chem.* **2008**, *634*, 56-60.

(16) Kriegerbeck, P.; Brodbeck, A.; Strahle, J. *Z. Naturforsch. B* **1989**, *44*, 237-239.

(17) Zachwieja, U. *J. Alloys Compd.* **1993**, *196*, 187-190.

(18) Palasyuk, A.; Grin, Y.; Miller, G. J. *J. Am. Chem. Soc.* **2014**, *136*, 3108-3117.

(19) Seidel, S.; Hoffmann, R.-D.; Pöttgen, R. *Monatsh. Chem.* **2014**, *145*, 1043-1049.

(20) Smetana, V.; Steinberg, S.; Card, N.; Mudring, A.; Miller, G. *Inorg. Chem.* **2015**, *54*, 1010-1018.

(21) Lin, Q.; Mishra, T.; Corbett, J. D. *J Am. Chem. Soc.* **2013**, *135*, 11023–11031.

(22) Gerke, B.; Hoffmann, R.-D.; Pöttgen, R. *Z. Anorg. Allg. Chem.* **2013**, *639*, 2444-2449.

(23) Gerke, B.; Pottgen, R. *Z. Naturforsch. B* **2014**, *69*, 121-124.

(24) Gerke, B.; Korthaus, A.; Niehaus, O.; Haarmann, F.; Pöttgen, R. *Z. Naturforsch. B* **2016**, *71*, 567-577.

(25) Zachwieja, U. *J. Alloys Compd.* **1993**, *199*, 115-118.

(26) Fickenscher, T.; Rodewald, U.; Pottgen, R. *Z. Kristallogr.* **2015**, *230*, 117-122.

(27) Provino, A.; Steinberg, S.; Smetana, V.; Kulkarni, R.; Dhar, S.; Manfrinetti, P.; Mudring, A. *J. Mat. Chem. C* **2015**, *3*, 8311-8321.

(28) Provino, A.; Steinberg, S.; Smetana, V.; Paramanik, U.; Manfrinetti, P.; Dhar, S. K.; Mudring, A.-V. *Cryst. Growth Des.* **2016**, *16*, 5657-5668.

(29) Gebresenbut, G.; Tamura, R.; Eklöf, D.; Gomez, C. *J. Phys.: Condens. Mat.* **2013**, *25*, 135402.

(30) Bigun, I.; Steinberg, S.; Smetana, V.; Mudryk, Y.; Kalychak, Y.; Havela, L.; Pecharsky, V.; Mudring, A.-V. *Chem. Mater.* **2017**, *29*, 2599-2614.

(31) Smetana, V.; Steinberg, S.; Mudryk, Y.; Pecharsky, V.; Miller, G. J.; Mudring, A.-V. *Inorg. Chem.* **2015**, *54*, 10296-10308.

(32) Fornasini, M. L.; Mazzone, D.; Provino, A.; Michetti, M.; Paudyal, D.; Gschneidner Jr, K. A.; Manfrinetti, P. *Intermetallics* **2014**, *53*, 169-176.

(33) Fickenscher, T.; Rodewald Ute, C.; Niehaus, O.; Gerke, B.; Haverkamp, S.; Eckert, H.; Pöttgen, R. *Z. Naturforsch. B* **2015**, *70*, 425.

(34) Celania, C.; Smetana, V.; Provino, A.; Pecharsky, V.; Manfrinetti, P.; Mudring, A.-V. *Inorg. Chem.* **2017**.

(35) Steeb, S.; Godel, D.; Lohr, C. **1968**, *15*, 137-141.

(36) Gschneidner, K.; McMasters, O.; Alexander, D.; Venteicher, R. *Metall. Trans.* **1970**, *1*, 1961-1971.

(37) Bsenko, L. *J. Less Common Met.* **1975**, *40*, 365-366.

(38) Bruzzone, G.; Merlo, F. *J. Less Common Met.* **1974**, *35*, 153-157.

(39) Tambomino, F.; Sappl, J.; Hoch, C. *J. Alloys Compd.* **2015**, *618*, 326-335.

(40) Celania, C.; Smetana, V.; Mudring, A.-V. *Acta Crystallogr. C* **2017**, *73*, 692-696.

(41) Canepa, F.; Palenzona, A.; Eggenhoffner, R. *Physica B* **1992**, *176*, 293-300.

(42) Eggenhoffner, R.; Canepa, F.; Palenzona, A. *J. Alloys Compd.* **1992**, *178*, 125-129.

(43) Dommann, A.; Hulligar, F. *J. Less Common Met.* **1988**, *141*, 261-273.

(44) Zhang, K.; Chen, L.; He, C. *J. Alloys Compd.* **1993**, *194*, 59-62.

(45) Gumenyuk, R.; Kuz'ma, Y. *Inorg. Mater.* **2007**, *43*, 135-137.

(46) Markiv, V.; Belyavina, N.; Gavrilenko, I. *Russ. Metall.* **1984**, 227-230.

(47) Verbovytskyy, Y. *Chem. Met. Alloys* **2014**, *7*, 42-55.

(48) Mazzone, D.; Marazza, R.; Riani, P.; Zanicchi, G.; Cacciamani, G.; Fornasini, M.; Manfrinetti, P. *CALPHAD* **2009**, *33*, 31-43.

(49) Lin, Q.; Corbett, J. *Inorg. Chem.* **2011**, *50*, 1808-1815.

(50) Belgacem, B.; Pasturel, M.; Tougait, O.; Potel, M.; Roisnel, T.; Ben Hassen, R.; Noel, H. *J. Alloys Compd.* **2009**, *478*, 89-95.

(51) Stoe & Cie GmbH Darmstadt, Germany, 2004.

(52) Blessing, R. H. *Acta Crystallogr. A* **1995**, *51*, 33-38.

(53) Bruker AXS, I. Madison, WI, 1996.

(54) Sheldrick, G. M. *Acta Crystallogr. A* **2008**, *64*, 112-122.

(55) Tambornino, F.; Hoch, C. *Z. Anorg. Allg. Chem.* **2015**, *641*, 537-542.

(56) Tkachuk, A. V.; Mar, A. *Inorg. Chem.* **2008**, *47*, 1313-1318.

(57) Hoch, C.; Simon, A. *Angew. Chem. Int. Ed.* **2012**, *51*, 3262-3265.

(58) Cordero, B.; Gomez, V.; Platero-Prats, A.; Reves, M.; Echeverria, J.; Cremades, E.; Barragan, F.; Alvarez, S. *Dalton Trans.* **2008**, 2832-2838.

(59) Krompholz, K.; Weiss, A. *Z. MetaIlkd.* **1976**, *67*, 400-403.

(60) Grin, Y.; Rogl, P.; Hiebl, K. *J. Less Common Met.* **1988**, *136*, 329-338.

(61) Lin, Q.; Corbett, J. *Acta Crystallogr. C - Struct. Chem.* **2014**, *70*, 773-775.

(62) Salamakha, L.; Sologub, O.; Goncalves, A.; Mudryi, S.; Almeida, M. *J. Alloys Compd.* **2007**, *429*, 140-142.

(63) Wang, F.; Miller, G. J. *Eur. J. Inorg. Chem.* **2011**, *2011*, 3989-3998.

(64) Markiv, V.; Shevchenko, I.; Belyavina, N.; Kuzmenko, P. *Dopov. Akad. Nauk. A.* **1986**, 78-81.

CHAPTER 5

BRINGING ORDER TO LARGE SCALE DISORDERED COMPLEX METAL ALLOYS: $Gd_2(Au, Sb)_{15}$ AND $Ba(Au, Ga)_{12}$

Submitted to Crystal Engineering Communications October 2017

Chris Celania, [†,‡] Volodymyr Smetana, [†,‖] Anja-Verena Mudring [†,‡,‖*]

[†]*The Ames Laboratory, U.S. Department of Energy, Iowa State University, Ames, IA 50011, USA*

[‡]*Department of Materials Science and Engineering, Iowa State University, Ames, IA 50011, USA*

[‖]*Department of Materials and Environmental Chemistry, Stockholm University, Svante Arrhenius väg 16 C, 106 91 Stockholm, Sweden*

Abstract

Two new tetragonal complex metallic alloys (CMAs) have been discovered and characterized: $Gd_2Au_{15-x}Sb_x$ [x = 3.0-3.6; *I*4/*mmm*; *tI*34; *a* = 7.31-7.33 Å, *c* = 14.05-14.11Å; *V* = 750.2-758 Å^3] and $BaAu_xGa_{12-x}$ [x = 3.6−4.4; *I*4/*mcm*; *tI*104; *a* = 8.77−8.78 Å, *c* = 26.06−26.13 Å; *V* = 2006.5-2010Å^3]. Both structures incorporate significant anionic site mixing and intricate positional disorder. $Gd_2Au_{15-x}Sb_x$ represents a new structure type with in-plane disordered, however, strongly geometrically restricted rhombi motifs. These rhombi connect through additional mixed Au/Sb positions along the *c* axis forming octahedral fragments. $BaAu_xGa_{12-x}$ finds its place within the extended $NaZn_{13}$ structural family, displaying cation centered snub cubes with empty, distorted icosahedra (allowing for the 1:12 ratio) and tetrahedral stars. The split positions order due to geometric constraints to form nets of crown cyclooctane-like sheets in two different conformations. Adjacent planes adopt opposite conformations, forming layers of snub cubes with ordering between layers, but disordered across the greater structure. The substantial degree of mixing in both structures, together with

mutual orientation of the ordered and disordered positions suggest a significant importance of heteroatomic bonding, typically found for polar intermetallic compounds.

Introduction

Complex metallic alloys (CMAs) are denoted by their markedly intricate structure, often leading to interesting physical and mechanical properties with respect to other intermetallics. Their elaborate structures create a rich area for study housing notable thermoelectric and magnetocaloric materials.[1, 2] Site mixing and disorder can often have radical effects on magnetic and transport properties within a given structure type.[3, 4] Unit cells of CMAs range from tens to thousands of atoms, regularly forming icosahedral symmetries, and frequently incorporate defect features such as disorder, extensive site mixing, and vacancies.[5, 6] Quasicrystals therefore also align closely with CMAs. These structural characteristics of CMAs inspire physical, mechanical, electronic, and transport properties that differ from typical metal alloys and allow them to find application in areas such as thermoelectrics or catalysis.[1-3, 6-9] For successful materials design and synthesis in these areas, a complete understanding of the variety of structural disorder accessible is still required. This point is emphasized by recent research on the $La(Fe,Si)_{13}$ system, a member of the $NaZn_{13}$ family of structures.[10] This system is well known for its magnetic properties, specifically the giant magnetocaloric effect as observed in $LaFe_{11.4}Si_{1.6}$.[4] Additionally, the system allows for a great deal of Fe/Si mixing, which significantly affects the Curie temperature of the compounds. Recent work on a $NaZn_{13}$ type representative with Eu, Au and Ga sheds more light on the influence of site preference effects on magnetic properties within the structure.[11] Available types of disorder known with Au CMAs are discussed in detail in this report.

Strong relativistic effects affecting gold's bonding behavior allow for extensive heteroatomic and homoatomic formations with high coordination, including clusters and anionic networks around more electropositive counterparts.[12, 13] Homoatomic gold assemblies include: secluded clusters of Au_7 located in $A_4Au_7X_2$ (A = K, Rb, Cs; X = Ge, Sn),[14, 15] 1D columns such as Au zig-zag chains in Ca_3Au_3In,[16] and 2D slabs observed in K_2Au_3.[17] 3D gold networks are represented by interconnected trigonal bipyramids in KAu_5,[18] hexagonal diamond-like frameworks of Au in the *Ae*-Au-*Tr* (*Ae* = alkaline earth, *Tr* = triel element) systems,[19-25] and combinations of tetrahedral and square planar Au segments in Rb_3Au_7.[26] These features also make Au a productive component for quasicrystals and crystalline approximants.[12, 27-31]

Group I, II and the rare earth metals act as formal electron donors within these networks, and have been useful in forming a variety of new ternary representatives with gold in the last several years[11, 13, 20-24, 32-38]. The addition of rare earth components allows for the added benefit of potentially useful magnetic and electronic properties (ferromagnetism, magnetocaloric effect, superconductivity, thermoelectricity, etc.) due to their shielded 4*f* orbitals and high magnetic moments[11, 21, 39-43]. The addition of post-transition metals allows for electron tuning of the overall valence electron count (*vec*) toward stable structures. Many are recognized for their high miscibility in gold structures as well as for their existence in disordered or other complex structures, sometimes stabilizing ternary representatives of binary phases that do not exist.[44, 45] Much recent focus has been on ternary compounds with tin and led to the discovery of the $R_3Au_6Sn_5$,[46, 47] $R_3Au_4Sn_3$,[46] $R_5Au_8Sn_5$,[46] $R_4Au_7Sn_4$,[46] $R_2Au_5Sn_2$[43] and $R_3Au_7Sn_3$ series of compounds[39, 40]. The following work has been completed to better understand the disordered

$R_{14}Au_{51}$ structure and the incorporation of different post-transition representatives utilizing a variety of group 13-15 elements[45, 48, 49].

Experimental Section

1. Synthesis.

Starting materials used for synthesis were Au (99.98 %) and Gd (99.9 %) from the Materials Preparation Center, Ames Laboratory, and Sb (99.99 %), Ga (99.999 %), and dendritic Ba (99.99 %) from Alfa Aesar. All materials were stored under Ar atmosphere, but the Ba pieces were scraped to remove any surface oxide layer before measuring. A representative of the $Gd_2Au_{15-x}Sb_x$ solution was first observed as a minor phase in a sample loaded with Gd:Au:Sb in a 2:5:1 ratio during exploration toward new gold-rich rare earth intermetallics. The $Ba(Au,Ga)_{12}$ compound was found during more targeted testing of compounds with Ba:*M* ratios of 1:12 following previous work on 1:12 and 1:13 $NaZn_{13}$ type derivatives and disordered superstructures. Compounds were formed by high-temperature reaction and annealing in sealed tantalum ampules (by arc welding under argon atmosphere) jacketed in fused silica (under vacuum). The $Gd_2Au_{15-x}Sb_x$ sample was reacted at 1000°C for 3 hours, followed by annealing at 850°C for 12 hours. A second representative of the solid solution was found in a sample loaded at a Gd:Au:Sb ratio of 6:13:1 and at slightly more intense heating scheme of 1050°C for 5 hours, followed by annealing at 850°C for 72 hours. The $BaAu_xGa_{12-x}$ sample was formed at lower temperatures of 800°C for 8 hours followed by a quench and subsequent anneal at 400°C for 5 days. This synthesis strategy allows for a fully molten low melting component to act as a flux for reaction with the high surface-area-to-volume ratio of the other components (small chunks or filings). Short reaction times were chosen in order to avoid unwanted reactions between Au/Ga/Sb with the Ta crucible. Total mass of samples prepared

was 0.5g, and all appeared dark gray with a metallic luster, remaining stable weeks later.

2. X-Ray Analysis.

X-ray powder diffraction for phase analysis was performed on samples by a STOE STADI P diffractometer with a STOE image plate detector with Cu $K_{\alpha 1}$; λ = 1.54059 Å (a = 5.4308(1) Å). For powder preparation the brittle samples were ground, then sieved to < 38 μm particles, and dispersed onto vacuum grease sandwiched between Mylar© sheets and fixed by Al rings. Data analysis was performed with the *WinXPow 3.06* software package.[50]

Single crystals were selected under an optical microscope from crushed samples, and then affixed to a glass fiber with grease. Single crystal X-ray diffraction at room temperature was performed on either a Bruker APEX CCD diffractometer or a Bruker D8 VENTURE diffractometer (both with Mo K_α radiation; λ = 0.71073 Å), utilizing the APEX 2 and APEX 3 software suites (for the former and the latter diffractometer, respectively) for data collection, integration, polarization, and empirical absorption correction.[51, 52] Scans ranged 2θ values of ~3-62°. The SHELXTL suite and XPREP algorithms within were used to check for extinction conditions and E statistics in the intensity data sets necessary for the assignment of the proper space groups (*I*4/*mmm* for $Gd_2Au_{15-x}Sb_x$ and *I*4/*mcm* for $BaAu_xGa_{12-x}$). Direct methods were used for structure solution determination (SHELXS-97).[53] APEX 3 software was then utilized to carry out full structure refinement (refining atomic positions, determining mixed site occupancies, identifying disordered positions, and anisotropic displacement parameters). The single crystal refinement data for $Gd_2Au_{11.43}Sb_{3.57}$ and $BaAu_{4.36}Ga_{7.64}$ are summarized in Tables 1 and 2. Table 1 displays the relevant refinement information and parameters, while Table 2 displays site-specific positional information. Atomic coordinates and occupations for the second crystals of each structure, $Gd_2Au_{10.32}Sb_{4.68}$ and $BaAu_{3.58}Ga_{8.42}$, are also included in

Table A5 for comparison of mixing and composition. Interatomic distances for all compounds may be found in the Table A7 as well.

Results and Discussion

Both compounds discussed are strongly dominated by anionic components and incorporate significant element mixing in their crystal structures and a very specific crystallographic ordering. **$Gd_2Au_{15-x}Sb_x$** represents a new structure type, *I*4/*mmm*, *tI*34. It is characterized by its unique disorder leading to a complex anionic network. The *8i* position is split along the *a* and the *b* axes around the *c* axis as displayed in Figure 1. The split positions are designated as (AuSb)5 (inner, yellow) and (AuSb)6 (outer, gray). Filling of immediately adjacent (AuSb)5 sites is impossible because of the unrealistically short distance for (AuSb)-(AuSb) contacts (2.131(5) Å). Similarly, the (AuSb)6 positions may only be filled if the nearest (AuSb)5 sites are empty (otherwise forming a distance of only 1.738(9) Å). The expected motif formed by occupied sites about the *c* axis resembles a rhombus, as depicted in Figure 1, with positions made translucent that are geometrically incapable of being filled. To summarize, once a particular split position is occupied, geometric constraints force the occupation of the rest of the *a*-*b* plane into perpendicular rhombi. Refinements suggest nearly perfect 50% occupation of both sites, which supports this disorder scheme. Instead of viewing the structural disorder in terms of the occupation of specific site, it is more prudent to then think of it as ordered planes of orthogonal, checkered rhombi that come in two settings, chosen stochastically. The system exhibits local order within a given *a*-*b* plane, but long-range disorder when comparing different *a*-*b* planes along the c axis.

The overall structure is displayed in Figure 2 with unoccupied disordered atoms removed for clarity. The disordered rhombus is shown to the right for comparison (with all disordered sites present) as well as the (AuSb)3 sites directly above and below the center of the rhombus. The inner (AuSb)5 positions, when occupied, appear to connect above and below the rhombus (shown as orange bonds in the cut out of Figure 2) to form rhombic bipyramids (or highly distorted octahedra). The outer (AuSb)6 positions in contrast, would create an unreasonably long distance (3.916(5) Å) to the Au3 site, but may still form interplanar bonds by connecting the disordered rhombi to the square patterned (AuSb)2 sites in the center of the unit cell. One may surmise that the electronic structure and properties of this compound may have interesting directional preference due to the disordered nature of bond formation of the anionic network along the *c* direction.

Pairs of distorted octahedra along the *c* axis are formed from the (AuSb)1, 2, and 3 sites, which are connected by the *2a* site. These octahedra are nearly ideal − 2.97 Å toward the *2a* site and 3.14 Å toward the opposite end (AuSb3, *4e* sites) (labeled in Figure 2). It should be noted from Table 2 that all non-Gd positions within the structure allow for significant Au-Sb site mixing. This includes both disordered positions, though it appears in both $Gd_2Au_{15-x}Sb_x$ samples that the inner position shows strong preference for Au occupation while the outer position somewhat prefers Sb. The overall structure then may be modeled as combinations of anionic polyhedra in the form of empty distorted octahedra and disordered slabs of orthogonal, checkered empty rhombic bipyramids surrounding Gd positions. The closest structural comparison may come from Cs_9Pt_4H, which shows similar distortion in its octahedra.[54] Octahedra line the unit cell edges and center of the cell in analogy to the polyhedra within $Gd_2Au_{15-x}Sb_x$, though with centering atoms and various filled interstitial sites. Not

unexpectedly, none of the distorted octahedra within Cs_9Pt_4H are to the extent of appearing as rhombic bipyramids.

The coordination numbers of the atomic positions range from 7 for the (AuSb)6 (outer) site, up to 10 for the (AuSb)5 (inner) site (see Figure A12). The high coordination and preferred Au occupation of the (AuSb)5 site compared with the (AuSb)6 site is consistent with high coordination often found in Au bonding. Because of the complex interactions of the disordered planes with the other (AuSb) sites along the *c* axis, these coordination polyhedra were analyzed to find a simpler representation that may accurately describe the structure.

The (AuSb)2 site is unique in that it connects to all other Wyckoff positions, including both disordered sites. The coordination polyhedra are flexible to the positional changes by forming one of two enantiomorphs depending on which disordered sites are occupied at a given location (see Figure A12). These polyhedra of coordination number 10 may be viewed as either distorted sphenocorona or a distorted, biaugmented rectangular prisms (see Figure A12 or the right side of Figure 3). The coordination polyhedra for the (AuSb)2 sites also allow for a polyhedral stacking sequence that accounts for all atoms, with each polyhedron made up of bonds with realistic atomic distances (Figure 3). Polyhedra display both intra and inter-planar vertex and face sharing, which form a stacking pattern of A, B, A', B'. Layers colored the same (A and A' or B and B') are related through a half unit cell translation, while layers with opposite color (A and B or A' and B') are affected by a 90° roto-inversion.

One may notice that both representatives of this solid solution were found as side products in samples that were loaded with compositions that are more Gd-rich and Sb-poor. All attempts to form the compound at composition were unsuccessful, including multiple synthesis techniques (self-flux, Na-flux, and arc melting). This phase might be metastable or

form only as a side product of the formation of other Au-rich Gd-Au-Sb compounds. Attempts at synthesis with other rare earths or post-transition metals have also been ineffective, implying strong electronic and size restrictions of the components. Nonetheless, there is a noticeable range of *vec*'s available for this phase, ranging from 2.08-2.34 e/a.

$BaAu_{3.6}Ga_{8.4}$, the first representative of **$BaAu_xGa_{12-x}$** (*I*4/*mcm*; *tI*104), was initially detected during our systematic explorations of the gold richer parts of the $Ba(Au_xGa_{12-x})_{1+y}$ solid solution, and has been assumed to be a tetragonal superstructural variant of the $NaZn_{13}$ type.[11] Similar to the $Gd_2Au_{15-x}Sb_x$ structure, $BaAu_xGa_{12-x}$ is most characteristically defined by its anionic site mixing and extensive disorder. In this case, there are five mixed Ga/Au sites ((GaAu)2-6) and two split positions: (GaAu)2/(GaAu)3 and (GaAu)4/(GaAu)5. The detected phase width in $BaAu_xGa_{12-x}$ is not negligible but still restricted within a few at.% of the solid solution similarly to the cubic Au-richer Ba–Au–Ga phases. One may note from Table A6 that the more Ga-rich crystal creates considerable differences in site mixing within the split positions. For example, the (GaAu)4 site switches from a majority of Au occupation to nearly 90% Ga occupied. The (GaAu)5 split position also becomes nearly completely occupied by Ga.

Short (GaAu)2-(GaAu)4 and (GaAu)3-(GaAu)5 distances within a given *a*-*b* plane (2.10(3) Å and 2.38(7) Å respectively) ensure occupation of (GaAu)2 with (GaAu)5 and (GaAu)3 with (GaAu)4. Either combination forms ordered rings similar to the crown conformation of cyclooctane. When comparing these rings to those made up of Zn in the snub cubes of $NaZn_{13}$, the (GaAu)2/(GaAu)5 rings and (GaAu)3/(GaAu)4 rings are less and more distorted from the ideal, respectively (Figure A14). Once any of the disordered positions is occupied, geometrical requirements order the rest of the plane of disordered positions into one

of two net conformations (Figure 4). Moreover, each ring is nested directly above or below a second octagonal ring. (GaAu)5-(GaAu)5 from adjacent rings along the c axis would form unreasonably short distances of 1.74(4) Å, while (GaAu)4-(GaAu)4 sites form exceptionally long distances of 3.607(7) Å. Somewhat long distances are found within the icosahedra of $NaZn_{13}$, but none of such a magnitude are found within the snub cubes. Interplanar (GaAu)2-(GaAu)2 and (AuGa)3-(AuGa)3 distances are short, but to a lesser extreme: 2.60(5) Å and 2.51(7) Å respectively. It is therefore impossible for each disordered position to be greater than 50% occupied without forming a short contact. These interplanar geometries also necessitate ordering such that adjacent disordered nets form opposite conformations. These paired nets make up the center planes of the distorted snub cubes, forming one of two conformations (Figure 5 top), each with their own mirrored enantiomorphs. The distorted snub cubes have parallel square caps as opposed to the antiparallel of a true snub cube. Therefore, the snub cubes within an individual layer are all ordered into one conformation. More regular snub cubes are formed from the atomic planes without disorder (Figure 5 bottom). Both layers of snub cubes combine into an ABA'B stacking sequence (Figure 6). A and A' layers are related by a ¼ unit cell translation along the [110] and centered by opposite enantiomorphs of regular snub cubes. Meanwhile, B layers are composed of the enantiomorphs of one of the two conformations of distorted snub cubes, which is chosen stochastically. Three settings for these disordered snub cubes (which affect the icosahedra formed between layers) have been chosen at convenience in Figure 6. If preferable, one may then choose to view the structure in terms of extensive stacking faults that are statistically random within a higher symmetry derivative of the $NaZn_{13}$ family of structures. By this nature of logic, it may be possible for mechanically induced phase transformations to exist within this structure. Ga is the main component of this

compound, causing the crystals to be noticeably ductile and making crystal selection for x-ray diffraction difficult. However, this property of Ga-rich samples could facilitate such a potential defect induced transition. In general, split position distribution and ordering across planes within both the $Gd_2Au_{15-x}Sb_x$ and $BaAu_xGa_{12-x}$ structures make either phase of potential interest for certain property testing and deeper understanding of structure-property relationships.

Unlike the $Gd_2Au_{15-x}Sb_x$ structure, the $BaAu_xGa_{12-x}$ structure has a clear analogue to a well-known structure: the $NaZn_{13}$ family of structures. This extensive family incorporates various lattice symmetries and space groups, including another recently reported Ba-Au-Ga compound: $BaAu_{7.13}Ga_{5.03}$.[11] Three main features characterize structures within this family: stacks of snub cube layers, icosahedral voids, and tetrahedral stars (TS). The icosahedral voids may be empty, partially occupied (10–17%) or centered depending on compound. The original $NaZn_{13}$ structure is shown on Figure A13 for comparison,[10]. Variation in occupation of the icosahedra allows for compositions to range from cation-anion ratios of 1:12 to 1:13. The recently reported $BaAu_{7.13}Ga_{5.03}$ cubic structure derives from $NaZn_{13}$ by only occupying the center of the icosahedra ~16% of the time. In the case of $BaAu_xGa_{12-x}$ structure, we see both empty distorted octahedra and TS's (Figure 6). The site mixing and disorder within the snub cubes and their stacking, as discussed previously, set this compound structurally slightly apart from other 1:12 and 1:13 structures like $Ce_2Ni_{17}Si_9$[55] and La(Fe, Si)$_{13}$[4] (which share the same *I*4/*mcm* space group), and move it closer to $RbAu_4Ga_{8.6,}$[32] not at least to rather large difference in cation and anion dimensions.

It is interesting to note that by increasing the relative amount of Ga in the system (from $BaAu_{7.13}Ga_{5.03}$ to the new composition $BaAu_{4.36}Ga_{7.64}$), not only does Ga vacate the icosahedral void site, but also a new, complex form of disorder within the snub cube stacking sequence

arises. A compositional structure transformation is noted for the $Ba(Au,Zn)_{13}$ system as well.[33] The structure transitions from the cubic $NaZn_{13}$ type, to a tetragonal P4/*nbm* ordered structure around $BaAu_6Zn_7$ composition. Additional Zn forces the system back into the cubic structure. This existence of the transition is discussed in terms of its ability to maximize heteroatomic gold bonds. Unfortunately, thermodynamic reasoning for its stability remains unknown. While two $NaZn_{13}$ family representatives have now been located with Ba, Au, and Ga, none has yet been located at a 1:13 cation-anion ratio, despite significant testing. DFT analyses of the close relatives $EuAu_{6.21}Ga_{5.79(2)}$ and $EuAu_{6.09}Al_{5.91}$ (tetragonal and orthorhombic) demonstrated similar absolute energy differences and allude to maximization of heteroatomic Au-Ga/Al bonding as the main force of structural stabilization.[11] Emphasis on heteroatomic bonding is also supported by ICOHP data, in which Au-Ga/Al contacts dominate the bonding populations. The large amount of mixed positions in $BaAu_xGa_{12-x}$ suggests in analogy with cubic relatives that the structure tries to avoid the symmetry restrictions and maximize the amount of heteroatomic bonding.

Summary

Two new tetragonal CMAs, $Gd_2Au_{15-x}Sb_x$ and $BaAu_xGa_{12-x}$, with elaborate site mixing and positional disorder have been discovered. Both compounds incorporate a significant degree of positional disorder that is significantly restricted on the local scale due to geometric factors. In $Gd_2Au_{15-x}Sb_x$ this leads to layers of empty perpendicular rhombic bipyramids interspersed with empty disordered octahedra. Only one of the split positions is capable of bonding along the *c* direction, presumably creating somewhat anisotropic electronic and transport properties. An alternative polyhedral description is also included, comprised of an

ABA'B' stacking sequence of the mixed (AuSb)2 coordination polyhedra, which forms enantiomorphs depending on which split sites are occupied. In contrast, $BaAu_xGa_{12-x}$ is a member of the $NaZn_{13}$ family, composed of cation centered snub cubes with empty icosahedra and tetrahedral stars. The empty icosahedra and tetrahedral stars account for the atomic ratio change from 1:13 to 1:12. However, $BaAu_xGa_{12-x}$ is truly set apart from these structures by its two split positions, which again order due to geometric constraints. In this case, they form two conformations of nets made up of crown conformation cyclooctane-like features. Adjacent planes must also adopt opposite conformations due to geometry as well. Combining the crown conformations creates layers of snub cubes that are ordered within layers, but randomized between layers (ABA'B stacking sequence, where the B layers have statistically random ordering). This intricate interaction and ordering of planes from disordered positions within both structures prompts a further understanding of disorder on the properties of CMAs.

Table 1. Crystallographic details and refinement parameters for $Gd_2Au_{11.43}Sb_{3.57}$ and $BaAu_{4.53}Ga_{7.47}$.

Formula	$Gd_2Au_{11.43}Sb_{3.57}$	$BaAu_{4.55}Ga_{7.16}$
Structure type	$Gd_2(Au, Sb)_{15}$	$NaZn_{13}$
MW (g/mol)	3512.50	1550.09
Space group, Z	*I*4/*mmm* (no. 139), 2	*I*4/*mcm* (no. 140), 8
Lattice constants [Å]	$a = b = 7.330(9)$, $c = 14.11(2)$	$a = b = 8.774(1)$, $c = 26.064(4)$
V [Å^3]	758.(2)	2006.5(6)
Diffractometer	Bruker CCD	Bruker CCD
Radiation	Mo-K_α (graphite monochromator)	Mo-K_α (graphite monochromator)
Temperature [K]	293(2)	293(2)
Density (calculated) [g/cm^3]	15.393	10.263
Absorption coefficient μ [mm^{-1}]	156.586	89.400
F (000)	2830	5163
θ range for data collection	3.931° – 31.063°	1.563° – 24.996°
Index ranges	$-10 \le h \le 10$ $-9 \le k \le 9$ $-19 \le l \le 20$	$-10 \le h \le 10$ $-9 \le k \le 6$ $-30 \le l \le 30$
Intensity data collected	2233	5394
# of independent reflections	378 [$R_{int} = 0.0445$]	508 [$R_{int} = 0.0445$]
Completeness to $\theta = 29.996$ °	98.7 %	100%
Type of absorption correction	Empirical	Empirical
Data/Restraints/Parameters	378/ 0/ 27	508/ 0/ 42
Structure solution & refinement	SHELXTL 2014	SHELXTL 2014
Scattering factors	International Tables Vol. C	International Tables Vol. C
Goodness-of-fit (F^2)	1.119	1.119
R_1, ωR_2 [$I_0 > 2\sigma$ (I)]	0.0445; 0.0929	0.0735; 0.1504
R_1, ωR_2 (all data)	0.0741; 0.1024	0.0947; 01602
Largest diff. peak & hole [e·Å^{-3}]	4.943 and -5.830	4.960 and -5.073

Table 2. Atomic coordinates and equivalent isotropic displacement parameters ($Å^2x10^3$) for the $Gd_2Au_{11.43}Sb_{3.57}$ and $BaAu_{4.53}Ga_{7.47}$ crystals. U_{eq} is defined as one third of the trace of the orthogonalized U_{ij} tensor.

Atom	Wyckoff site	Occupation factor	*x*	*y*	*z*	U_{eq}
			$Gd_2Au_{11.43}Sb_{3.57}$			
Gd4	*4d*	1	1/2	0	1/4	0.0095(8)
Au1	*2a*	0.43	0	0	0	0.009 (1)
Sb1	*2a*	0.57	0	0	0	0.009 (1)
Au2	*16m*	0.94	0.2090(1)	0.2090(1)	0.14435(7)	0.0110(3)
Sb2	*16m*	0.06	0.2090(1)	0.2090(1)	0.14435(7)	0.0110(3)
Au3	*4e*	0.37	0	0	0.3056(2)	0.0063(9)
Sb3	*4e*	0.63	0	0	0.3056(2)	0.0063(9)
Au5	*8j*	0.45	0.2944(5)	1/2	0	0.012(1)
Sb5	*8j*	0.05	0.2944(5)	1/2	0	0.012(1)
Au6	*8j*	0.23	0.1186(6)	1/2	0	0.011(1)
Sb6	*8j*	0.27	0.1186(6)	1/2	0	0.011(1)
			$BaAu_{4.53}Ga_{7.47}$			
Ba1	*4a*	1	0	0	1/2	0.011(1)
Ba2	*4c*	1	1/2	1/2	0	0.013(1)
Au1	*16l*	1	0.3322(2)	0.1678(2)	0.19048(7)	0.0109(7)
Au2	*16l*	0.19	0.832(2)	0.668(2)	-0.0498(9)	0.004(8)
Ga2	*16l*	0.31	0.832(2)	0.668(2)	-0.0498(9)	0.004(8)
Au3	*16l*	0.28	0.863(8)	0.637(8)	-0.048(1)	0.04(1)
Ga3	*16l*	0.22	0.863(8)	0.637(8)	-0.048(1)	0.04(1)
Au4	*16l*	0.34	0.6680(5)	0.8320(5)	-0.0692(2)	0.018(2)
Ga4	*16l*	0.16	0.6680(5)	0.8320(5)	-0.0692(2)	0.018(2)
Au5	*16l*	0.09	0.631(1)	0.870(1)	-0.0333(8)	0.052(7)
Ga5	*16l*	0.41	0.631(1)	0.870(1)	-0.0333(8)	0.052(7)
Au6	*32m*	0.14	0.0524(4)	0.1991(4)	0.1280(1)	0.018(1)
Ga6	*32m*	0.86	0.0524(4)	0.1991(4)	0.1280(1)	0.018(1)
Ga7	*16l*	1	0.3780(4)	0.1220(4)	0.2891(2)	0.0117(7)

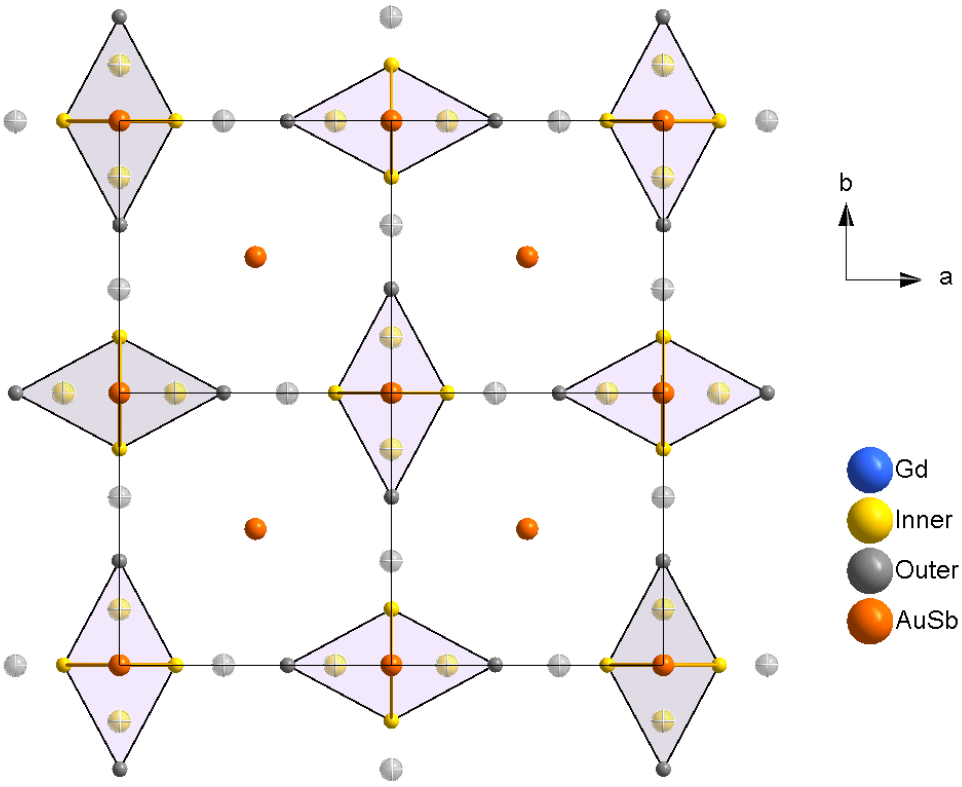

Figure 1. Representation of the disordered plane of $Gd_2(Au, Sb)_{15}$ forming perpendicular rhombuses. Unoccupied disordered positions are translucent.

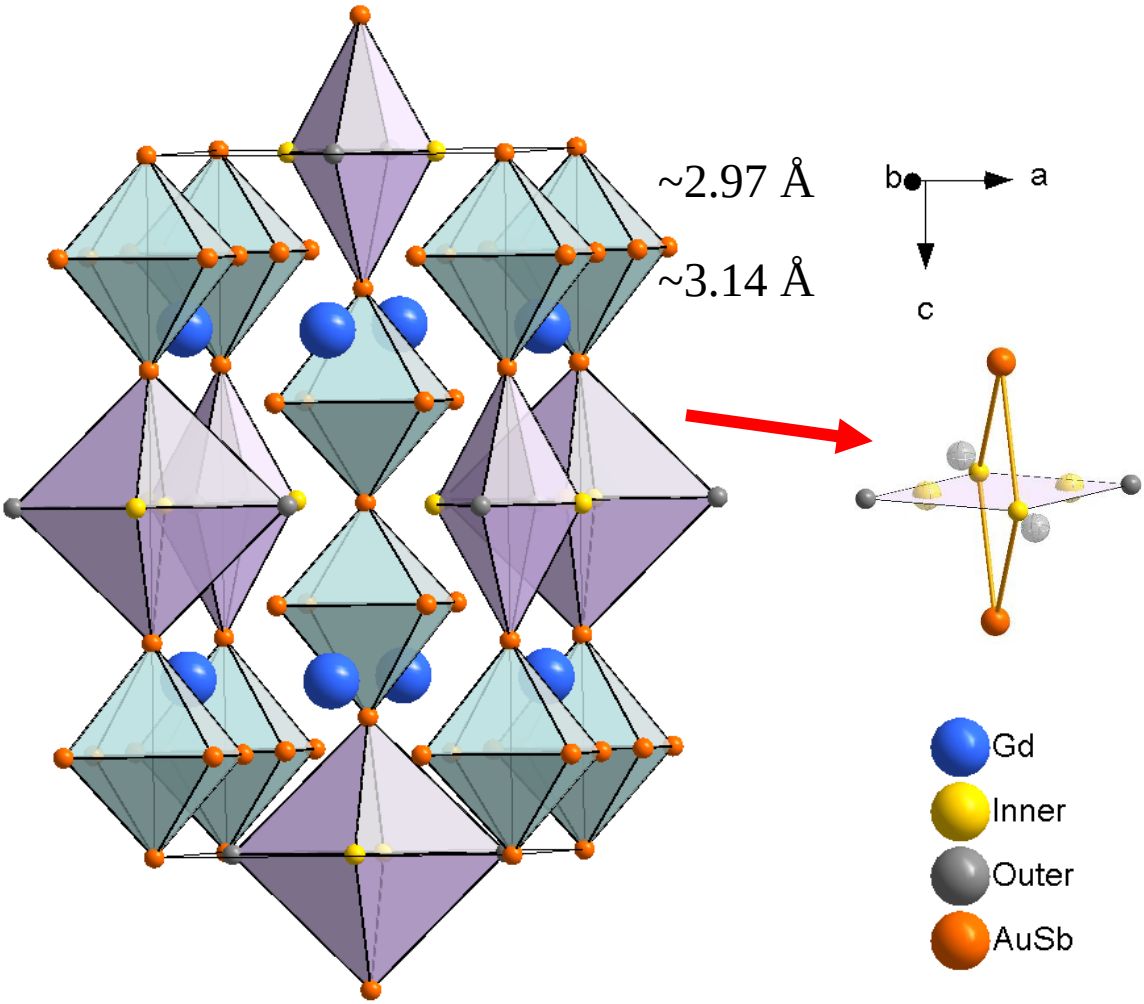

Figure 2. Representation of the structure of $Gd_2(Au, Sb)_{15}$ solved in *I*4/*mmm* as well as distances relating to octahedron distortion and inter-plane bonding. All non-Gd sites are mixed positions including the disordered position, which has been split into two half-occupied sites AuSb5 (inner) and AuSb6 (outer).

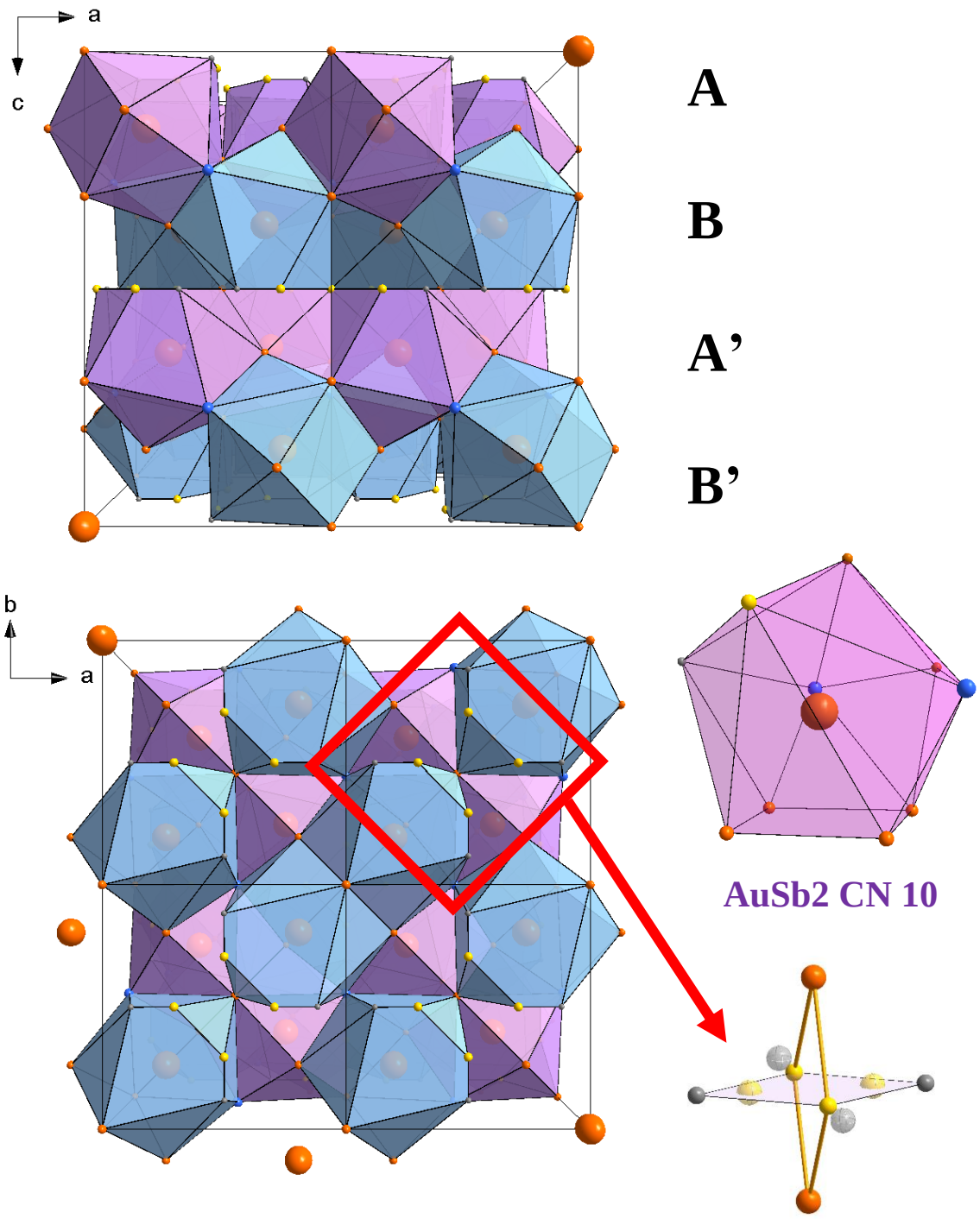

Figure 3. The structure and bonding may be represented by ordered stacking of the AuSb2 coordination polyhedra (colored differently for understanding of packing). All inner and outer positions (regardless of occupation) are depicted in the polyhedra for tracking of this plane.

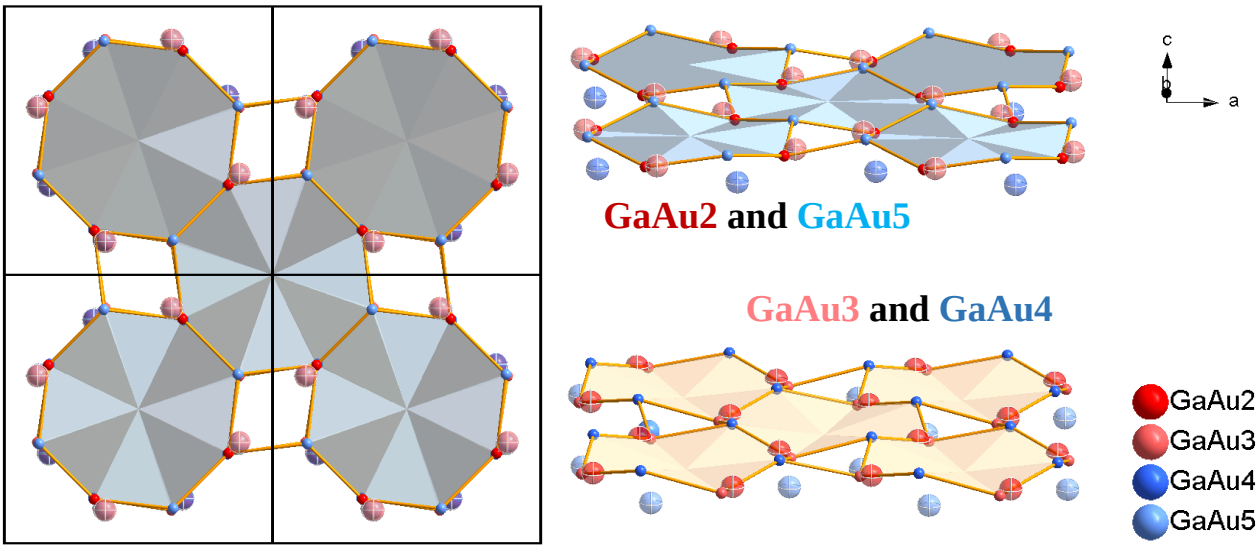

Figure 4. (Left) plane of crown conformation cyclooctane like features made up of heteroatomic disordered positions. (Right) Both net conformations are displayed with occupied sites labeled and unoccupied sites made translucent.

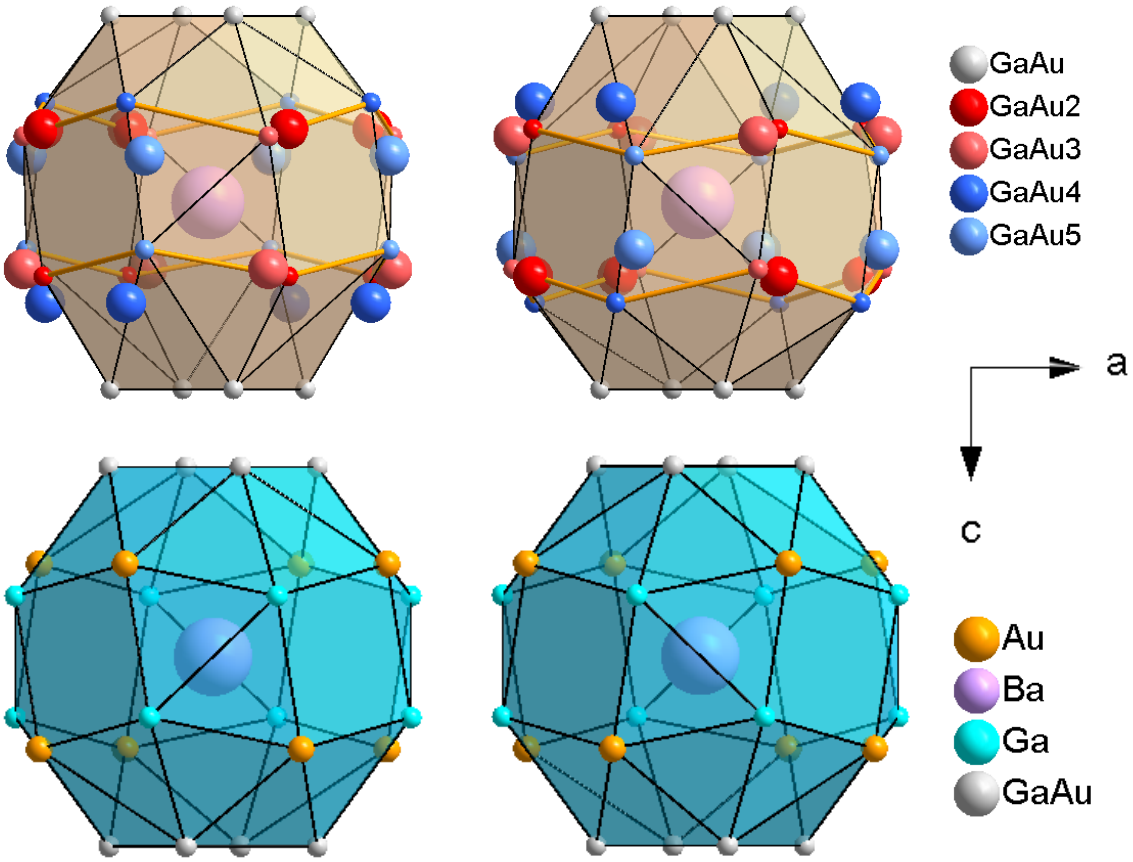

Figure 5. Enantiomorphs of snub cubes formed by disordered planes (top) and regular planes (bottom). Split positions are shaded differently in either red or blue, and unoccupied GaAu sites are noticeably larger for clarity.

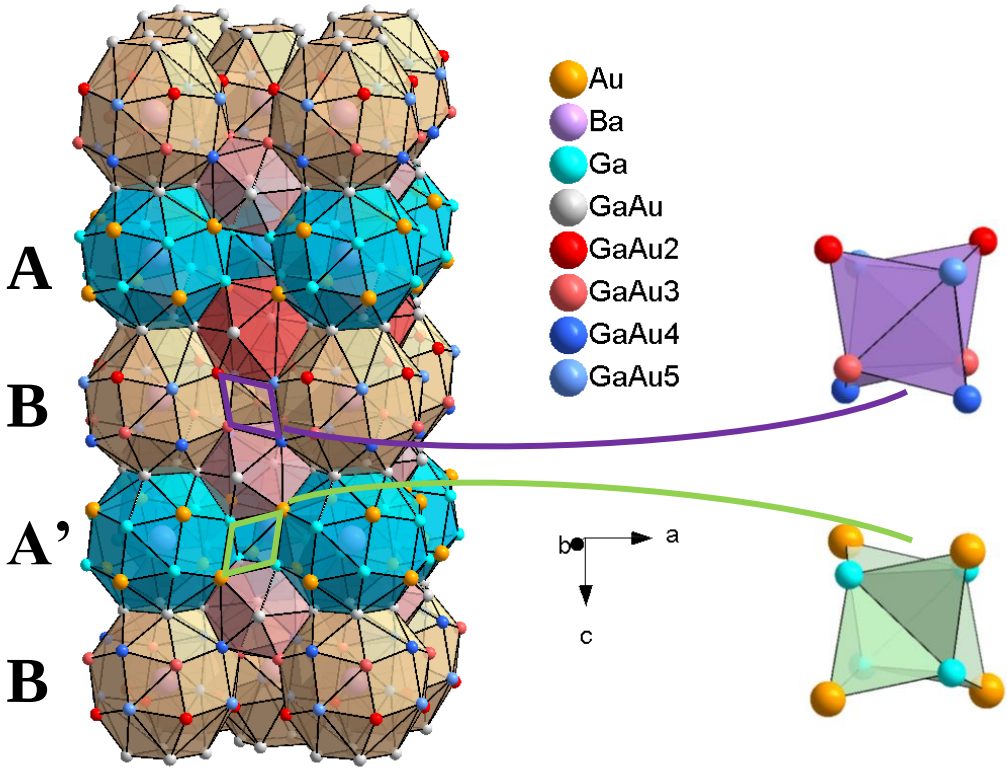

Figure 6. Polyhedral stacking sequence of $BaAu_xGa_{12-x}$. A and A' are offset by ¼ unit cell in the [110], and are therefore centered by opposite enantiomorphs. The conformation of disordered B layers is stochastic in nature, but uniform across individual layers. Ordering for each B layer has been chosen for clarity, also shown in the disordered pattern of the two icosahedra. The two types of tetrahedral stars are removed, but displayed to the right.

Information in Appendix

Table of interatomic distances for $Gd_2Au_{11.43}Sb_{3.57}$ and $BaAu_{4.55}Ga_{7.16}$; coordination polyhedra for the $Gd_2(Au, Sb)_{15}$ structure; polyhedral stacking representation of $NaZn_{13}$ structure for comparison.

Accession codes

CSD numbers 1578678–1578681 contain the supplementary crystallographic data for the compounds described in this paper. These data can be obtained free of charge via www.ccdc.cam.ac.uk/data_request/cif, or by emailing data_request@ccdc.cam.ac.uk, or by contacting The Cambridge Crystallographic Data Centre, 12 Union Road, Cambridge CB2 1EZ, UK; fax: +44 1223 336033.

Acknowledgments

The research was supported by the Office of the Basic Energy Sciences, Materials Sciences Division, U.S. DOE. Ames Laboratory is operated for DOE by Iowa State University under Contract DE-AC02-07CH11358.

Synopsis Image and Information

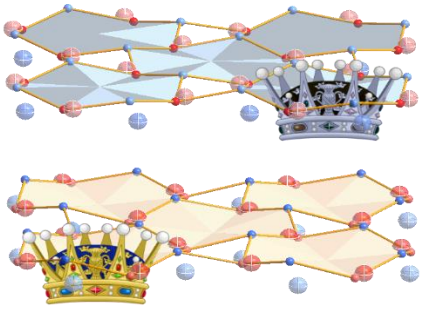

New complex metallic alloys $Ba(Au, Ga)_{12}$ and $Gd_2(Au, Sb)_{15}$ display entire planes of disordered atom sites, forming set planar conformations.

References

1. G. J. Snyder and E. S. Toberer, *Nat Mater*, 2008, **7**, 105-114.
2. K. Kovnir and M. Shatruk, *European Journal of Inorganic Chemistry*, 2011, **2011**, 3955-3962.
3. Y. Mudryk, P. Manfrinetti, V. Smetana, J. Liu, M. L. Fornasini, A. Provino, V. K. Pecharsky, G. J. Miller and K. A. Gschneidner, *J. Alloys Compd.*, 2013, **557**, 252-260.
4. F.-x. Hu, B.-g. Shen, J.-r. Sun, Z.-h. Cheng, G.-h. Rao and X.-x. Zhang, *Appl. Phys. Lett.*, 2001, **78**, 3675-3677.
5. J.-M. Dubois, E. Belin-Ferré and M. Feuerbacher, in *Complex Metallic Alloys*, Wiley-VCH Verlag GmbH & Co. KGaA, 2010, pp. 1-39.
6. J.-M. Dubois, *Chem. Soc. Rev.*, 2012, **41**, 6760-6777.
7. J. Dolinsek, *Chem. Soc. Rev.*, 2012, **41**, 6730-6744.
8. M. Heggen, L. Houben and M. Feuerbacher, *Nat Mater*, 2010, **9**, 332-336.
9. D. C. Schmitt, N. Haldolaarachchige, Y. Xiong, D. P. Young, R. Jin and J. Y. Chan, *J. Am. Chem. Soc.*, 2012, **134**, 5965-5973.
10. K. Nordell and G. Miller, *Inorg. Chem.*, 1999, **38**, 579-590.
11. V. Smetana, S. Steinberg, Y. Mudryk, V. Pecharsky, G. J. Miller and A.-V. Mudring, *Inorg. Chem.*, 2015, **54**, 10296-10308.
12. V. Smetana, M. Rhodehouse, G. Meyer and A. V. Mudring, *Acc. Chem. Res.*, 2017, **Accepted**.
13. V. Smetana, Q. Lin, D. K. Pratt, A. Kreyssig, M. Ramazanoglu, J. D. Corbett, A. I. Goldman and G. J. Miller, *Angew. Chem. Int. Ed.*, 2012, **51**, 12699-12702.
14. H.-D. Sinnen and H.-U. Schuster, *Z. Naturforsch. B*, 1981, **36**, 833.
15. U. Zachwieja and J. Wlodarski, *Z. Anorg. Allg. Chem.*, 1998, **624**, 1443-1446.
16. I. Muts, V. Zaremba, U. Rodewald and R. Pottgen, *Z. Anorg. Allg. Chem.*, 2008, **634**, 56-60.
17. P. Kriegerbeck, A. Brodbeck and J. Strahle, *Z. Naturforsch. B*, 1989, **44**, 237-239.
18. U. Zachwieja, *J. Alloys Compd.*, 1993, **196**, 187-190.
19. A. Palasyuk, Y. Grin and G. J. Miller, *J. Am. Chem. Soc.*, 2014, **136**, 3108-3117.

20. S. Seidel, R.-D. Hoffmann and R. Pöttgen, *Monatsh. Chem.*, 2014, **145**, 1043-1049.
21. V. Smetana, S. Steinberg, N. Card, A. Mudring and G. Miller, *Inorg. Chem.*, 2015, **54**, 1010-1018.
22. Q. Lin, T. Mishra and J. D. Corbett, *J Am. Chem. Soc.*, 2013, **135**, 11023–11031.
23. B. Gerke, R.-D. Hoffmann and R. Pöttgen, *Z. Anorg. Allg. Chem.*, 2013, **639**, 2444-2449.
24. B. Gerke and R. Pottgen, *Z. Naturforsch. B*, 2014, **69**, 121-124.
25. B. Gerke, A. Korthaus, O. Niehaus, F. Haarmann and R. Pöttgen, *Z. Naturforsch. B*, 2016, **71**, 567-577.
26. U. Zachwieja, *J. Alloys Compd.*, 1993, **199**, 115-118.
27. Q. Lin and J. Corbett, *J. Am. Chem. Soc.*, 2007, **129**, 6789-6797.
28. Q. Lin and J. Corbett, *Inorg. Chem.*, 2008, **47**, 7651-7659.
29. V. Smetana, J. D. Corbett and G. J. Miller, *J. Solid State Chem.*, 2013, **207**, 21-28.
30. Y. Morita and A. P. Tsai, *Jpn. J. Appl. Phys.*, 2008, **47**, 7975-7979.
31. T. Hiroto, K. Tokiwa and R. Tamura, *J. Phys.: Condens. Matter*, 2014, **26**, 216004/216001-216004/216007, 216007 pp.
32. V. Smetana, J. D. Corbett and G. J. Miller, *Z. Anorg. Allg. Chem.*, 2014, **640**, 790-796.
33. S. Gupta and J. D. Corbett, *Inorg. Chem.*, 2012, **51**, 2247-2253.
34. V. Smetana, G. J. Miller and J. D. Corbett, *Inorg. Chem.*, 2013, **52**, 12502-12510.
35. V. Smetana, G. J. Miller and J. D. Corbett, *Inorg. Chem.*, 2012, **51**, 7711-7721.
36. A. Palasyuk, Y. Grin and G. J. Miller, *J. Am. Chem. Soc.*, 2014, **136**, 3108-3117.
37. B. Li, S.-J. Kim, G. J. Miller and J. D. Corbett, *Inorg. Chem.*, 2009, **48**, 6573-6583.
38. T. Mishra, Q. Lin and J. D. Corbett, *Inorg. Chem.*, 2013, **52**, 13623-13630.
39. A. Provino, S. Steinberg, V. Smetana, R. Kulkarni, S. Dhar, P. Manfrinetti and A. Mudring, *J. Mat. Chem. C*, 2015, **3**, 8311-8321.
40. A. Provino, S. Steinberg, V. Smetana, U. Paramanik, P. Manfrinetti, S. K. Dhar and A.-V. Mudring, *Cryst. Growth Des.*, 2016, **16**, 5657-5668.
41. G. Gebresenbut, R. Tamura, D. Eklöf and C. Gomez, *J. Phys.: Condens. Mat.*, 2013, **25**, 135402.

42. I. Bigun, S. Steinberg, V. Smetana, Y. Mudryk, Y. Kalychak, L. Havela, V. Pecharsky and A.-V. Mudring, *Chem. Mater.*, 2017, **29**, 2599-2614.
43. T. Fickenscher, U. Rodewald and R. Pottgen, *Z. Kristallogr.*, 2015, **230**, 117-122.
44. P. Chai and J. Corbett, *Inorganic Chemistry*, 2011, **50**, 10949-10955.
45. C. Celania, V. Smetana, A. Provino, P. Manfrinetti and A.-V. Mudring, *Inorg. Chem.*, 2017, **submitted**.
46. M. L. Fornasini, D. Mazzone, A. Provino, M. Michetti, D. Paudyal, K. A. Gschneidner Jr and P. Manfrinetti, *Intermetallics*, 2014, **53**, 169-176.
47. T. Fickenscher, C. Rodewald Ute, O. Niehaus, B. Gerke, S. Haverkamp, H. Eckert and R. Pöttgen, *Z. Naturforsch. B*, 2015, **70**, 425.
48. C. Celania, V. Smetana, A. Provino, V. Pecharsky, P. Manfrinetti and A. Mudring, *Inorg. Chem.*, 2017, **56**, 7247-7256.
49. C. Celania, V. Smetana and A.-V. Mudring, *Acta Crystallogr. Sect. C: Cryst. Struct. Commun.*, 2017, **73**.
50. Stoe & Cie GmbH, *Journal*, 2004.
51. R. H. Blessing, *Acta Crystallogr. A*, 1995, **51**, 33-38.
52. I. Bruker AXS, *Journal*, 1996.
53. G. M. Sheldrick, *Acta Crystallogr. A*, 2008, **64**, 112-122.
54. V. Smetana and A. Mudring, *Angew. Chem. Int. Ed.*, 2016, **55**, 14838-14841.
55. O. I. Bodak, *Kristallografiya*, 1979, **24**, 1280-1282.

CHAPTER 6

GENERAL CONCLUSION

Conclusion

Through the various works described in Chapters 2-5, a great deal of new understanding has been added to the family of *R*-Au-*M* compounds, specifically in the areas of Au-rich phases and group 15 element additions. Incorporating a variety of synthesis techniques, structure analysis, physical property measurement, and electronic structure calculations, these experiments covered a wide swath of scientific inquiry. Efforts to expand our knowledge on ternary compounds have successfully created a series of new R_3Au_9Pn structures, new structural data for the $Y_{14}Au_{51}$ and Y_3Au_4 binary phases, twenty new ternary representatives of the $R_{14}Au_{51}$ structure, as well as two new $Gd_2(Au, Sb)_{15}$ and $Ba(Au, Ga)_{12}$ structures with extensive site mixing and disorder.

The $R_{14}(Au, M)_{51}$ series acts as a nexus connecting many concepts across the various works of this document. The R_3Au_9Pn series shares structural features in stacking of empty fully capped trigonal prisms, allowing for structural comparison between previously unrelated $Gd_{14}Ag_{51}$ and $Cu_{10}Sn_3$ structure types. In fact, both structures often formed simultaneously in samples during exploration. Magnetic testing of the Ho_3Au_9Sb compound yielded interesting magnetic properties, featuring two metamagnetic transitions toward more ferromagnetic ordering. Continued exploration of the ternary $R_{14}Au_{51}$ representatives led to the new structural information gained on the binary $Y_{14}Au_{51}$ phase and the similarly gold-rich Y_3Au_4 phase. A new structural representation of Y_3Au_4 was also created, defined by channels composed of combinations of chair conformation cyclohexane-like features of Au

atoms. The R_{14}(Au, M)$_{51}$ work greatly expanded on the knowledge of Au/M site mixing and the stabilization of binary structures by M additions. Two samples from the R_{14}(Au, M)$_{51}$ series display additional positional disorder, unlike that seen elsewhere in the family of structures. However, the positional disorder of the R_{14}(Au, M)$_{51}$ compounds is outshone by the extensive Au/M mixing and positional disorder of the new Gd_2(Au, Sb)$_{15}$ and Ba(Au, Ga)$_{12}$ phases. Within both compounds nearly all Au sites display Au/M mixing. Similarly, the split positions in both compounds are geometrically constrained so that entire planes become ordered, with the disorder becoming noticeable between layers. While physical property testing has thus far been prioritized solely for the R_3Au_9Pn series, these disordered structures provide an interesting opportunity for testing of electronic and transport properties.

Proposed Future Work

The Au-rich sections of many R-Au-M phase diagrams remain relatively underexplored due to the prevalence in interest in R-rich regions for pursuit of magnetic properties. Of these phases, a series of Mo_5B_2Si type R_5M_2X structures has been reported for R = Y, Gd-Er; M = Ir-Au; and X = Sn, Sb, Pd, Bi with varying success depending on the elemental combinations[29-32]. Of these, an extensive physical property analysis has only been completed on the Ir compounds[30]. Expectedly, the high magnetic moments from the rare earths allow for ferromagnetic transitions in various compounds. However, it is noteworthy that the Gd-based compounds show a magnetocaloric effect via isothermal entropy changes near 120 and 150 K. Preliminary efforts to spread the understanding of this structure type succeeded in the creation of two new Gd-Au-X representatives: X = In, Sn. While pure phase synthesis proves difficult within the Au series, DC measurements have been completed on samples of

Gd_5Au_2Bi, Gd_5Au_2Sn, and Ho_5Au_2Bi. These compounds align with hopes of comparing between *R* size and *X* size while drawing parallels to properties within the Ir compounds (such as evidence of the magnetocaloric effect). It should be noted that compositionally similar Yb_5Sb_3 type phases with Ni have been discovered, also demonstrating the magnetocaloric effect.[33, 34]

Exploration to ascertain new Gd_5Au_2X representatives led to an unexpected discovery of a cubic, Gd-rich Gd-Au-Te phase, the first phase to be reported within this ternary phase field. Preliminary analysis of the structure appears to predict only a small fraction of Te within the structure, mixing into a predominantly Au site. Presumably the excess electrons of Te are critical in stabilizing the structure; however, electronic structure calculations and further experimentation are still required.

At this point, it may become somewhat obvious that *R*-Au-Te phases are under-explored and an area rich for materials discovery. There are only three reported ternary structures ($R_7Au_2Te_2$, $R_5Au_2Te_2$, and $Lu_6Au_1Te_2$), with few representatives, all of which are *R*-rich compositions[35-38]. While Te compounds have some synthesis difficulties, this is not an unknown or insurmountable obstacle, demonstrated by the work reported in this document. Similarly, the *R*-Au-Bi systems contain slightly more reported ternary structures (*R*AuBi, $RAuBi_2$, $R_3Au_3Bi_4$, and as mentioned before, R_5Au_2Bi) as well as the R_3Au_9Bi and $R_{14}(Au, Bi)_{51}$ structures described in this document[39-42]. One may note that there is at least one compound in each main region of the *R*-Au-Bi, making it less fruitful for new discovery. However, because of the prevalence of thermoelectrics with Bi compounds, new compounds have a high probability of return in scientific interest. Another area of opportunity arises by exchanging Au for nearby Pt, which shares many exceptional properties. While the electron

affinity of Pt is not quite as exceptionally high as Au, it still boasts a value on par with the chalcogenides such as Te. Interestingly, there are *no* reported compounds/structures within any of the R-Pt-Te phase fields. The similar affinities may provide an interesting opportunity for comparison or competition when combined with less electronegative components like the rare-earth metals. New compounds, in any case, within the *R*-(Au, Pt)-*M* family add to the understanding of bonding and structure-property relationships within the system and may be useful in guiding synthesis and exploration in the future.

REFERENCES

1. T. Fickenscher, U. Rodewald and R. Pöttgen, *Zeitschrift Für Kristallographie-Crystalline Materials*, 2015, **230**, 117-122.
2. A. Provino, S. Steinberg, V. Smetana, R. Kulkarni, S. Dhar, P. Manfrinetti and A. Mudring, *Journal of Materials Chemistry C*, 2015, **3**, 8311-8321.
3. B. Gerke and R. Pöttgen, *Zeitschrift Für Naturforschung Section B-a Journal of Chemical Sciences*, 2014, **69**, 121-124.
4. G. Gebresenbut, R. Tamura, D. Eklof and C. Gomez, *Journal of Physics-Condensed Matter*, 2013, **25**.
5. V. Smetana, S. Steinberg, N. Card, A. Mudring and G. Miller, *Inorganic Chemistry*, 2015, **54**, 1010-1018.
6. A. Provino, S. Steinberg, V. Smetana, U. Paramanik, P. Manfrinetti, S. K. Dhar and A.-V. Mudring, *Crystal Growth & Design*, 2016, **16**, 5657-5668.
7. K. Pitzer, *Accounts of Chemical Research*, 1979, **12**, 272-276.
8. P. Pyykkö and J. Desclaux, *Accounts of Chemical Research*, 1979, **12**, 276-281.
9. P. Pyykkö, *Chemical Reviews*, 1988, **88**, 563-594.
10. P. Pyykkö, M. Johnson and T. Martinez, *Annual Review of Physical Chemistry, Vol 63*, 2012, **63**, 45-64.
11. P. Schwerdtfeger, R. Bast, M. Gerry, C. Jacob, M. Jansen, V. Kello, A. Mudring, A. Sadlej, T. Saue, T. Sohnel and F. Wagner, *Journal of Chemical Physics*, 2005, **122**.
12. A. Mudring, M. Jansen, J. Daniels, S. Kramer, M. Mehring, J. Ramalho, A. Romero and M. Parrinello, *Angewandte Chemie-International Edition*, 2002, **41**, 120-124.
13. A. Mudring and M. Jansen, *Angewandte Chemie-International Edition*, 2000, **39**, 3066-3067.
14. V. Smetana, Q. Lin, D. Pratt, A. Kreyssig, M. Ramazanoglu, J. Corbett, A. Goldman and G. Miller, *Angewandte Chemie-International Edition*, 2012, **51**, 12699-12702.
15. Q. Lin and J. Corbett, *Journal of the American Chemical Society*, 2007, **129**, 6789-6797.
16. Q. Lin and J. Corbett, *Inorganic Chemistry*, 2008, **47**, 7651-7659.
17. H. Sinnen and H. Schuster, *Zeitschrift Für Naturforschung Section B-a Journal of Chemical Sciences*, 1981, **36**, 833-836.
18. U. Zachwieja and J. Wlodarski, *Zeitschrift Für Anorganische Und Allgemeine Chemie*, 1998, **624**, 1443-1446.

19. I. Muts, V. Zaremba, U. Rodewald and R. Pottgen, *Zeitschrift Für Anorganische Und Allgemeine Chemie*, 2008, **634**, 56-60.

20. P. Kriegerbeck, A. Brodbeck and J. Strahle, *Zeitschrift Für Naturforschung Section B-a Journal of Chemical Sciences*, 1989, **44**, 237-239.

21. U. Zachwieja, *Journal of Alloys and Compounds*, 1993, **196**, 187-190.

22. A. Palasyuk, Y. Grin and G. Miller, *Journal of the American Chemical Society*, 2014, **136**, 3108-3117.

23. U. Zachwieja, *Journal of Alloys and Compounds*, 1993, **199**, 115-118.

24. L. P. Salamakha, O. L. Sologub, A. P. Gonçalves, S. I. Mudryi and M. Almeida, *Journal of Alloys and Compounds*, 2007, **429**, 140-142.

25. Stoe & Cie GmbH, Darmstadt, Germany, 2004.

26. I. Bruker AXS, Madison, Wisconsin, 1996.

27. R. Blessing, *Acta Crystallographica Section a*, 1995, **51**, 33-38.

28. G. Sheldrick, *Acta Crystallographica Section a*, 2008, **64**, 112-122.

29. Y. Mozharivskyj and H. Franzen, *Journal of Alloys and Compounds*, 2001, **327**, 78-81.

30. K. Schafer, C. Schwickert, O. Niehaus, F. Winter and R. Pöttgen, *Solid State Sciences*, 2014, **35**, 66-73.

31. Y. Verbovytsky, K. Łątka and A. W. Pacyna, *Journal of Alloys and Compounds*, 2007, **442**, 337-340.

32. Y. Verbovytsky and K. Łątka, *Journal of Alloys and Compounds*, 2007, **438**, L4-L6.

33. V. Svitlyk, F. Fei and Y. Mozharivskyj, *Journal of Solid State Chemistry*, 2008, **181**, 1080-1086.

34. V. Svitlyk, F. Fei and Y. Mozharivskyj, *Solid State Sciences*, 2009, **11**, 1700-1702.

35. P. Chai and J. Corbett, *Inorganic Chemistry*, 2011, **50**, 10949-10955.

36. P. Chai and J. Corbett, *Inorganic Chemistry*, 2012, **51**, 3548-3556.

37. S. Gupta, P. Maggard and J. Corbett, *European Journal of Inorganic Chemistry*, 2010, 2620-2625.

38. S. Gupta and J. Corbett, *Dalton Transactions*, 2010, **39**, 6074-6079.

39. F. Merlo, M. Pani and M. L. Fornasini, *Journal of the Less Common Metals*, 1990, **166**, 319-327.

40. E. Seibel, L. Schoop, W. Xie, Q. Gibson, J. Webb, M. Fuccillo, J. Krizan and R. Cava, *Journal of the American Chemical Society*, 2015, **137**, 1282-1289.

41. E. Seibel, W. Xie, Q. Gibson and R. Cava, *Journal of Solid State Chemistry*, 2015, **230**, 318-324.

42. E. Seibel, W. Xie, Q. Gibson and R. Cava, *Inorganic Chemistry*, 2016, **55**, 3583-3588.

APPENDIX: SUPPLEMENTARY TABLES AND FIGURES

Table A2. Summary of the thermal synthesis techniques used for each sample including: high-temperature reactions in tube furnaces, annealing in tube furnaces, Differential Thermal Analysis (DTA), and arc melting.

R*$_3$Au$_9$*Pn	**Thermal Treatment**
Gd_3Au_9Sb	1000°C for 3 hrs, annealed at 850°C for 12 hrs
Tb_3Au_9Sb	DTA, annealed at 960°C for 5 days
Dy_3Au_9Sb	1050°C for 5 hrs, annealed at 850 for 72 hrs
Ho_3Au_9Sb	900°C for 10 days
Er_3Au_9Sb	900°C for 7 days
Tm_3Au_9Sb	Arc melted
Y_3Au_9Sb	DTA, annealed at 900°C for 10 days
Gd_3Au_9Bi	Arc melted, annealed at 850°C for 2 days and 700°C for 5 days

Table A2. Anisotropic displacement parameters U_{ij} [Å^2] for Gd_3Au_9Sb.

Atom	***U*$_{11}$**	***U*$_{22}$**	***U*$_{33}$**	***U*$_{12}$**	***U*$_{13}$**	***U*$_{23}$**
Au1	0.00202(17)	0.00202(17)	0.0064(3)	0.000	0.000	0.00101(9)
Au2	0.00436(18)	0.00506(18)	0.00296(18)	-0.00150(12)	-0.00125(13)	0.00292(14)
Au3	0.0028(2)	0.0028(2)	0.0107(5)	0.000	0.000	0.00138(12)
Gd	0.0025(3)	0.0018(3)	0.0013(3)	0.000	0.000	0.0017(2)
Sb	0.0007(4)	0.0007(4)	0.0015(7)	0.000	0.000	0.00037(18)

Table A3. Interatomic distances (Å) for both Y_3Au_4 and $Y_{14}Au_{51}$ samples.

Y_3Au_4			
Au1—Y4^{i}	2.8810 (17)	Au2—Au3	2.9820 (4)
Au1—Au1^{ii}	2.9738 (12)	Au2—Au3^{xiii}	2.9820 (4)
Au1—Y4^{iii}	2.9773 (17)	Au3—Au2^{xiv}	2.9820 (4)
Au1—Au1^{iv}	3.0577 (9)	Au3—Y4	3.0808 (17)

Au1—Au1^{v}	3.0578 (9)	Au3—Y4^{xv}	3.0808 (17)
Au1—Y4^{ii}	3.0596 (17)	Au3—Y4^{xii}	3.0808 (17)
Au1—Y4^{vi}	3.0651 (17)	Au3—Y4^{xvi}	3.0808 (17)
Au1—Y4^{vii}	3.1590 (17)	Au3—Y4^{i}	3.0808 (17)
Au1—Y4^{viii}	3.1688 (18)	Au3—Y4^{xvii}	3.0808 (17)
Au1—Y4^{ix}	3.2754 (17)	Y4—Au1^{xii}	2.8810 (17)
Au2—Y4^{x}	2.9425 (16)	Y4—Au1^{xviii}	2.9773 (17)
Au2—Y4^{xi}	2.9425 (16)	Y4—Au1^{ii}	3.0596 (17)
Au2—Y4^{i}	2.9425 (16)	Y4—Au1^{xix}	3.0651 (17)
Au2—Y4^{ix}	2.9425 (16)	Y4—Au1^{xx}	3.1590 (17)
Au2—Y4^{xii}	2.9425 (16)	Y4—Au1^{xxi}	3.1688 (18)
Au2—Y4	2.9425 (16)	Y4—Au1^{xi}	3.2755 (17)

$Y_{14}Au_{51}$

Au1—Au3^{xxiii}	2.7542 (7)	Au5—Y3^{x}	3.188 (2)
Au1—Au4	2.7769 (7)	Au5—Y3	3.188 (2)
Au1—Au6	2.8654 (6)	Au5—Au5^{x}	3.196 (2)
Au1—Au3^{xii}	2.9686 (7)	Au6—Au7	2.8358 (9)
Au1—Au2^{xii}	2.9735 (7)	Au6—Au1^{xxxv}	2.8653 (6)
Au1—Au1^{xxiv}	2.9933 (9)	Au6—Au1^{xxxvi}	2.8654 (6)
Au1—Y1^{xxv}	3.0393 (14)	Au6—Au3^{xxiii}	2.8818 (6)
Au1—Y1^{xxvi}	3.0429 (14)	Au6—Au3^{xxxvii}	2.8818 (6)
Au1—Au2^{xxvi}	3.0640 (7)	Au6—Au3^{xxvi}	2.8818 (6)
Au1—Y1^{xxiii}	3.1036 (14)	Au6—Y1^{xxiii}	3.0189 (13)
Au1—Y2	3.1532 (7)	Au6—Y1^{xxxviii}	3.0189 (13)
Au2—Au3	2.7337 (7)	Au6—Y1^{xxvi}	3.0189 (13)
Au2—Au5^{xxvii}	2.7381 (9)	Au7—Au6^{xxxix}	2.8358 (9)
Au2—Au5^{xxviii}	2.8229 (10)	Au7—Au3^{xl}	2.8488 (5)
Au2—Au4^{xxix}	2.8630 (6)	Au7—Au3^{xxxvii}	2.8488 (5)
Au2—Au4^{xxviii}	2.8708 (6)	Au7—Au3^{xxiii}	2.8488 (5)
Au2—Au1^{i}	2.9735 (7)	Au7—Au3^{xxxii}	2.8488 (5)
Au2—Au2^{xxvi}	2.9872 (6)	Au7—Au3^{xi}	2.8488 (5)
Au2—Au2^{xxviii}	2.9872 (6)	Au7—Au3^{xxvi}	2.8488 (5)
Au2—Y3	3.0537 (8)	Au7—Y2	3.1572 (18)
Au2—Au1^{xxviii}	3.0639 (7)	Au7—Y2^{xxxix}	3.1572 (18)
Au2—Y2^{xxviii}	3.0723 (13)	Au7—Y2^{xli}	3.1572 (18)
Au2—Y2^{xxvii}	3.2509 (14)	Y1—Au6^{xxxviii}	3.0190 (13)
Au3—Au1^{xxx}	2.7542 (7)	Y1—Au6^{xxx}	3.0190 (13)
Au3—Au3^{xxxi}	2.7692 (9)	Y1—Au1^{i}	3.0393 (14)
Au3—Au7^{xxxii}	2.8489 (5)	Y1—Au1^{xxix}	3.0393 (14)
Au3—Au6^{xxx}	2.8818 (6)	Y1—Au1^{xv}	3.0429 (14)
Au3—Au1^{i}	2.9686 (7)	Y1—Au1^{xxviii}	3.0429 (14)

Au3—Au3^{xxxiii}	3.0024 (10)	Y1—Au1^{xlii}	3.1037 (14)
Au3—Y2^{xxvii}	3.1167 (15)	Y1—Au1^{xxx}	3.1037 (14)
Au3—Y2^{xxx}	3.1852 (17)	Y1—Au4^{xxviii}	3.1174 (16)
Au3—Y2^{xxviii}	3.2096 (16)	Y1—Au4^{xxix}	3.1837 (16)
Au3—Y1	3.2373 (7)	Y1—Au3^{xxiv}	3.2374 (7)
Au4—Au4^{xxvi}	2.6942 (7)	Y2—Au2^{xi}	3.0723 (13)
Au4—Au4^{xxviii}	2.6942 (7)	Y2—Au2^{xxvi}	3.0723 (13)
Au4—Au1^{xxiv}	2.7769 (7)	Y2—Au3^{xxxiv}	3.1167 (15)
Au4—Au2^{xii}	2.8630 (6)	Y2—Au3^{xii}	3.1167 (15)
Au4—Au2^{xxv}	2.8630 (6)	Y2—Au1^{xxxi}	3.1532 (7)
Au4—Au2^{xvi}	2.8709 (6)	Y2—Au3^{xxiii}	3.1852 (16)
Au4—Au2^{xxvi}	2.8709 (6)	Y2—Au3^{xl}	3.1852 (17)
Au4—Y1^{xxvi}	3.1175 (17)	Y2—Au3^{xxvi}	3.2096 (15)
Au4—Y1^{xxv}	3.1837 (16)	Y2—Au3^{xi}	3.2096 (15)
Au4—Y3	3.2463 (15)	Y3—Au2^{i}	3.0537 (8)
Au4—Y3^{xvii}	3.2463 (15)	Y3—Au2^{xliii}	3.0537 (8)
Au5—Au5^{xxviii}	1.5982 (12)	Y3—Au2^{xxvi}	3.0537 (8)
Au5—Au5^{xxvi}	1.5983 (12)	Y3—Au2^{xxviii}	3.0537 (8)
Au5—Au2^{xxxiv}	2.7381 (9)	Y3—Au2^{xii}	3.0537 (8)
Au5—Au2^{xii}	2.7381 (9)	Y3—Au5^{xxxiv}	3.188 (2)
Au5—Au5^{xxvii}	2.768 (2)	Y3—Au5^{x}	3.188 (2)
Au5—Au5^{xxxiv}	2.768 (2)	Y3—Au5^{xxvi}	3.188 (2)
Au5—Y2	2.799 (2)	Y3—Au5^{xxvii}	3.188 (2)
Au5—Au2^{xxvi}	2.8228 (10)	Y3—Au5^{xxviii}	3.188 (2)
Au5—Au2^{xi}	2.8228 (10)		

Symmetry code(s): (i) −*x*+*y*, −*x*, *z*; (ii) −*x*+2/3, −*y*+1/3, −*z*+1/3; (iii) −*y*+2/3, *x*−*y*+1/3, *z*−2/3; (iv) −*x*+*y*+2/3, −*x*+1/3, *z*+1/3; (v) −*y*+1/3, *x*−*y*−1/3, *z*−1/3; (vi) *x*−*y*+2/3, *x*+1/3, −*z*+1/3; (vii) −*y*+2/3, *x*−*y*+1/3, *z*+1/3; (viii) *x*+1/3, *y*−1/3, *z*−1/3; (ix) *y*, −*x*+*y*, −*z*; (x) −*x*, −*y*, −*z*; (xi) *x*−*y*, *x*, −*z*; (xii) −*y*, *x*−*y*, *z*; (xiii) *x*, *y*, *z*−1; (xiv) *x*, *y*, *z*+1; (xv) *y*, −*x*+*y*, −*z*+1; (xvi) *x*−*y*, *x*, −*z*+1; (xvii) −*x*, −*y*, −*z*+1; (xviii) −*x*+*y*+1/3, −*x*+2/3, *z*+2/3; (xix) *y*−1/3, −*x*+*y*+1/3, −*z*+1/3; (xx) −*x*+*y*+1/3, −*x*+2/3, *z*−1/3; (xxi) *x*−1/3, *y*+1/3, *z*+1/3; (xxii) −*x*+1/3, −*y*+2/3, −*z*+2/3; (xxiii) *y*, −*x*+*y*+1, *z*; (xxiv) *x*, *y*, −*z*+1; (xxv) −*y*, *x*−*y*, −*z*+1; (xxvi) *x*−*y*, *x*, *z*; (xxvii) −*x*+*y*, −*x*, −*z*; (xxviii) *y*, −*x*+*y*, *z*; (xxix) −*x*+*y*, −*x*, −*z*+1; (xxx) *x*−*y*+1, *x*, *z*; (xxxi) *x*, *y*, −*z*; (xxxii) −*x*+1, −*y*+1, −*z*; (xxxiii) −*x*+1, −*y*, *z*; (xxxiv) −*y*, *x*−*y*, −*z*; (xxxv) −*y*+1, *x*−*y*+1, *z*; (xxxvi) −*x*+*y*, −*x*+1, *z*; (xxxvii) −*x*+1, −*y*+1, *z*; (xxxviii) −*x*+1, −*y*+1, −*z*+1; (xxxix) −*x*+*y*, −*x*+1, −*z*; (xl) *y*, −*x*+*y*+1, −*z*; (xli) −*y*+1, *x*−*y*+1, −*z*; (xlii) *x*−*y*+1, *x*, −*z*+1; (xliii) −*x*, −*y*, *z*.

Table A4. EDS compositional data gathered from the several samples from the regions outlined in red within Figure A9. Atomic percentages are within 1% accuracy, and support projected elemental compositions based on single crystal refinement.

Sample	*M* atm%	*R* atm%	Au atm%
Ho-Au-Ge	8.78	21.39	69.82
Ho-Au-Sb	9.04	22.48	68.48
Nd-Au-Ga	8.81	21.72	69.48
Gd-Au-Sn	6.25	27.91	65.85
Lu-Au-Ga	24.5	21.37	54.13
La-Au-Bi	2.22	21.34	76.44
Sm-Au-Bi	2.13	20.96	76.91
Pr-Au-Sb	4.25	19.25	76.5

Table A5. Lattice parameter data obtained by powder X-ray diffraction peaks**.**

Sample	Lattice parameters [Å] *a* [Å]	*c* [Å]	V_{obs} [Å^3]
$Nd_{14}Au_{45.6}Ga_{5.4}$	12.6888(2)	9.2184(3)	1285.37(4)
$Gd_{14}Au_{46.9}Sn_{4.1}$	12.6958(1)	9.1960(1)	1283.7(1)
$Ho_{14}Au_{45.3}Ge_{5.7}$	12.4888(2)	9.0812(3)	1226.64(4)
$Ho_{14}Au_{45.1}Sb_{5.9}$	12.6192(1)	9.1869(1)	1267.0(1)
$Lu_{14}Au_{35.3}Ga_{15.7}$	12.3136(2)	8.9967(3)	1181.35(4)

Table A6. Atomic coordinates and equivalent isotropic displacement parameters ($Å^2x10^3$) for the $Gd_2Au_{10.32}Sb_{4.68}$ and $BaAu_{3.58}Ga_{8.42}$ crystals. U_{eq} is defined as one third of the trace of the orthogonalized U_{ij} tensor.

$Gd_2Au_{10.32}Sb_{4.68}$						
Gd4	*4d*	1	1/2	0	1/4	0.0095(8)
Au1	*2a*	0.403	0	0	0	0.009(1)
Sb1	*2a*	0.597	0	0	0	0.009(1)
Au2	*16m*	0.898	0.20857(9)	0.20857(9)	0.14447(6)	0.0110(3)
Sb2	*16m*	0.102	0.20857(9)	0.20857(9)	0.14447(6)	0.0110(3)
Au3	*4e*	0.405	0	0	0.3055(1)	0.0063(9)
Sb3	*4e*	0.595	0	0	0.3055(1)	0.0063(9)
Au5	*8j*	0.431	0.2941(4)	1/2	0	0.012(1)
Sb5	*8j*	0.069	0.2941(4)	1/2	0	0.012(1)
Au6	*8j*	0.184	0.1179(5)	1/2	0	0.011(1)
Sb6	*8j*	0.316	0.1179(5)	1/2	0	0.011(1)
$BaAu_{3.58}Ga_{8.42}$						
Ba1	*4a*	1	0	0	0.25	0.015(1)
Ba2	*4c*	1	0.5	0.5	0	0.019(1)
Au1	*16l*	1	0.3324(2)	0.1676(2)	0.19023(7)	0.0121(8)
Au2	*16l*	0.3(1)	0.836(3)	0.664(3)	-0.051(1)	0.010(6)
Ga2	*16l*	0.2(2)	0.836(3)	0.664(3)	-0.051(1)	0.010(6)
Au3	*16l*	0.05(2)	0.871(9)	0.629(9)	-0.044(1)	0.03(1)
Ga3	*16l*	0.45(2)	0.871(9)	0.629(9)	-0.044(1)	0.03(1)
Au4	*16l*	0.25(3)	0.6678(6)	0.8322(6)	-0.0693(3)	0.019(3)
Ga4	*16l*	0.25(3)	0.6678(6)	0.8322(6)	-0.0693(3)	0.019(3)
Au5	*16l*	0.01(3)	0.634(1)	0.866(1)	-0.0342(9)	0.037(9)
Ga5	*16l*	0.49(3)	0.634(1)	0.866(1)	-0.0342(9)	0.037(9)
Au6	*32m*	0.09(2)	0.0535(4)	0.2006(4)	0.1286(1)	0.016(2)
Ga6	*32m*	0.91(2)	0.0535(4)	0.2006(4)	0.1286(1)	0.016(2)
Ga7	*16l*	1	0.3789(4)	0.1211(4)	0.2889(2)	0.0121(8)

Table A7. Interatomic distance data for $Gd_2Au_{11.43}Sb_{3.57}$, $Gd_2Au_{10.32}Sb_{4.68}$, and $BaAu_{4.53}Ga_{7.47}$.

$Gd_2Au_{11.43}Sb_{3.57}$			
Au1—Sb2^{i}	2.973 (3)	Au5—Au6	1.289 (5)
Au1—Au2^{i}	2.973 (3)	Au5—Sb5^{xii}	2.131 (5)
Au1—Sb2^{ii}	2.973 (3)	Au5—Au5^{xii}	2.131 (5)
Au1—Sb2^{iii}	2.973 (3)	Au5—Sb5^{viii}	2.131 (5)
Au1—Au2^{iv}	2.973 (3)	Au5—Au5^{viii}	2.131 (5)
Au1—Au2^{v}	2.973 (3)	Au5—Sb5^{xiii}	3.013 (8)
Au1—Sb2^{v}	2.973 (3)	Au5—Au5^{xiii}	3.013 (8)
Au1—Sb2^{iv}	2.973 (3)	Au5—Sb2^{vii}	3.015 (3)
Au1—Au2^{iii}	2.973 (3)	Au5—Au2^{vii}	3.015 (3)
Au1—Au2^{ii}	2.973 (3)	Au6—Sb6^{xiv}	1.738 (9)
Au1—Au2^{vi}	2.973 (3)	Au6—Au6^{xiv}	1.738 (9)
Au1—Sb2^{vii}	2.973 (3)	Au6—Sb2^{xv}	3.023 (3)
Au2—Sb5^{viii}	3.015 (3)	Au6—Au2^{xv}	3.023 (3)
Au2—Au5^{viii}	3.015 (3)	Au6—Au2^{vii}	3.023 (3)
Au2—Au5	3.015 (3)	Au6—Sb2^{vii}	3.023 (3)
Au2—Gd4	3.020 (3)	Au6—Au2^{xii}	3.023 (3)
Au2—Gd4^{ix}	3.020 (3)	Au6—Sb2^{xii}	3.023 (3)
Au2—Au6	3.023 (3)	Au3—Sb2^{ix}	3.098 (4)
Au2—Sb6^{viii}	3.023 (3)	Au3—Au2^{ix}	3.098 (4)
Au2—Au6^{viii}	3.023 (3)	Au3—Sb2^{xvi}	3.098 (4)
Gd4—Sb2^{iii}	3.020 (3)	Au3—Au2^{xvi}	3.098 (4)
Gd4—Sb2^{x}	3.020 (3)	Au3—Sb2^{xi}	3.098 (4)
Gd4—Au2^{iii}	3.020 (3)	Au3—Au2^{xvii}	3.098 (4)
Gd4—Au2^{x}	3.020 (3)	Au3—Sb2^{xvii}	3.098 (4)
Gd4—Sb2^{xi}	3.020 (3)	Au3—Au2^{xi}	3.098 (4)
Gd4—Au2^{viii}	3.020 (3)	Au3—Sb5^{xvii}	3.128 (4)
Gd4—Au2^{ix}	3.020 (3)	Au3—Sb5^{ix}	3.128 (4)
Gd4—Au2^{xi}	3.020 (3)	Au3—Au5^{xvii}	3.128 (4)
Gd4—Sb2^{ix}	3.020 (3)	Au3—Au5^{ix}	3.128 (4)
Gd4—Sb2^{viii}	3.020 (3)		
$Gd_2Au_{10.32}Sb_{4.68}$			
Au1—Au2	2.9607 (14)	Gd4—Au2^{xix}	3.009 (2)
Au1—Sb2^{i}	2.9607 (14)	Au5—Au6	1.287 (5)
Au1—Au2^{i}	2.9607 (14)	Au5—Sb5^{xii}	2.128 (4)
Au1—Sb2^{ii}	2.9607 (14)	Au5—Au5^{xii}	2.128 (4)
Au1—Au2^{v}	2.9607 (14)	Au5—Sb5^{viii}	2.128 (4)
Au1—Sb2^{iii}	2.9607 (14)	Au5—Au5^{viii}	2.128 (4)
Au1—Sb2^{v}	2.9607 (14)	Au5—Au2^{vii}	3.008 (2)

Au1—Au2^{iii}	2.9607 (14)	Au5—Sb2^{vii}	3.008 (2)
Au1—Au2^{ii}	2.9607 (14)	Au5—Au2^{xv}	3.008 (2)
Au1—Au2^{iv}	2.9607 (14)	Au5—Sb2^{xv}	3.008 (2)
Au1—Sb2^{iv}	2.9607 (14)	Au3—Sb2^{ix}	3.092 (2)
Au2—Sb5^{viii}	3.0075 (10)	Au3—Au2^{ix}	3.092 (2)
Au2—Au5^{viii}	3.0075 (10)	Au3—Sb2^{xvi}	3.092 (2)
Au2—Au5	3.008 (2)	Au3—Au2^{xvi}	3.092 (2)
Au2—Gd4	3.0092 (12)	Au3—Sb2^{xi}	3.092 (2)
Au2—Gd4^{ix}	3.009 (2)	Au3—Au2^{xvii}	3.092 (2)
Au2—Sb6^{viii}	3.0155 (11)	Au3—Sb2^{xvii}	3.092 (2)
Au2—Au6^{viii}	3.0155 (11)	Au3—Au2^{xi}	3.092 (2)
Au2—Au6	3.016 (2)	Au3—Sb5^{xvii}	3.119 (2)
Gd4—Sb2^{iii}	3.0092 (12)	Au3—Sb5^{ix}	3.119 (2)
Gd4—Sb2^{x}	3.009 (2)	Au3—Au5^{xvii}	3.119 (2)
Gd4—Au2^{iii}	3.0092 (12)	Au3—Au5^{ix}	3.119 (2)
Gd4—Au2^{x}	3.009 (2)	Au6—Sb6^{xiv}	1.723 (7)
Gd4—Sb2^{xi}	3.009 (2)	Au6—Au6^{xiv}	1.723 (7)
Gd4—Au2^{viii}	3.0092 (12)	Au6—Sb5^{xiv}	3.011 (4)
Gd4—Sb2^{viii}	3.0092 (12)	Au6—Au5^{xiv}	3.011 (4)
Gd4—Sb2^{ix}	3.009 (2)	Au6—Au2^{xv}	3.016 (2)
Gd4—Au2^{ix}	3.009 (2)	Au6—Sb2^{xv}	3.016 (2)
Gd4—Au2^{xi}	3.009 (2)	Au6—Sb2^{vii}	3.016 (2)
Gd4—Au2^{xviii}	3.0092 (12)	Au6—Au2^{vii}	3.016 (2)

$BaAu_{4.53}Ga_{7.47}$

Au1—Ga8^{x}	2.629 (4)	Ga4—Au4^{vii}	2.553 (17)
Au1—Ga8^{xi}	2.629 (4)	Ga4—Au5	2.65 (2)
Au1—Ga8	2.632 (6)	Ga4—Au5^{xv}	2.658 (14)
Au1—Ga8^{ix}	2.662 (6)	Ga4—Au5^{xxv}	2.658 (14)
Au1—Ga6^{iii}	2.783 (3)	Ga4—Ga6^{xxiv}	2.724 (17)
Au1—Au6^{iii}	2.783 (3)	Ga4—Au6^{xxiv}	2.724 (17)
Au1—Ga6^{xx}	2.783 (3)	Ga4—Ga6^{xiii}	2.724 (17)
Au1—Au6^{xx}	2.783 (3)	Ga4—Au6^{xiii}	2.724 (17)
Au1—Au6	2.959 (4)	Au5—Ga5	1.064 (14)
Au1—Au6^{xxi}	2.959 (4)	Au5—Ga4^{xxvi}	2.658 (14)
Au1—Ga6^{xxi}	2.959 (4)	Au5—Ga4^{viii}	2.658 (14)
Ba2—Au1^{vi}	3.6152 (10)	Au5—Ga5^{vii}	2.674 (15)
Ba2—Au1^{ix}	3.6152 (10)	Au5—Ga6^{xxvii}	2.733 (5)
Ba2—Au1^{xi}	3.6152 (10)	Au5—Au6^{xxvii}	2.733 (5)
Ba2—Au1^{iii}	3.6152 (10)	Au5—Ga6^{xxviii}	2.733 (5)
Ba2—Au1^{xvi}	3.6152 (10)	Au5—Au6^{xxviii}	2.733 (5)
Ba2—Au1^{xvii}	3.6152 (10)	Au5—Ga6^{xxiv}	2.919 (6)

Ba2—Au1^{iv}	3.6152 (10)	Au5—Au6^{xxiv}	2.919 (6)
Ba2—Ga8	3.631 (3)	Ga5—Ga5^{vii}	1.68 (3)
Ba2—Ga8^{xvi}	3.631 (3)	Ga5—Ga4^{viii}	2.253 (17)
Ba2—Ga8^{iv}	3.631 (3)	Ga5—Ga4^{xxvi}	2.253 (17)
Ba2—Ga8^{ix}	3.631 (3)	Ga5—Au4^{viii}	2.635 (11)
Ba3—Au4	3.535 (3)	Ga5—Au4^{xxvi}	2.635 (11)
Ba3—Au4^{vii}	3.535 (3)	Ga5—Au5^{vii}	2.674 (15)
Ba3—Au4^{xxii}	3.535 (3)	Ga5—Ga4^{xxix}	3.01 (2)
Ba3—Au4^{xxiii}	3.535 (3)	Ga5—Ga4^{xxiii}	3.01 (2)
Ba3—Au4^{xv}	3.535 (3)	Ga5—Ba3^{xxx}	3.547 (6)
Ba3—Au4^{xiii}	3.535 (3)	Au6—Au4^{xiii}	2.543 (6)
Ba3—Au4^{xii}	3.535 (3)	Au6—Ga6^{iv}	2.556 (5)
Ba3—Au4^{viii}	3.535 (3)	Au6—Au6^{iv}	2.556 (5)
Ba3—Ga5^{vii}	3.547 (6)	Au6—Ga6^{iii}	2.556 (5)
Ba3—Ga5^{xxii}	3.547 (6)	Au6—Au6^{iii}	2.556 (5)
Ba3—Ga5^{xiii}	3.547 (6)	Au6—Ga4^{xiii}	2.723 (17)
Ba3—Ga5^{xii}	3.547 (6)	Au6—Au5^{xxxi}	2.733 (5)
Au4—Ga4	0.509 (16)	Au6—Ga8^{ix}	2.739 (6)
Au4—Au5	2.144 (10)	Au6—Au1^{iv}	2.783 (3)
Au4—Ga6^{xxiv}	2.543 (6)	Au6—Au5^{xiii}	2.919 (6)
Au4—Au6^{xxiv}	2.543 (6)	Au6—Au6^{xxi}	3.083 (7)
Au4—Ga6^{xiii}	2.543 (6)	Ga8—Au1^{x}	2.629 (4)
Au4—Au6^{xiii}	2.543 (6)	Ga8—Au1^{xi}	2.629 (4)
Au4—Ga4^{vii}	2.553 (17)	Ga8—Au1^{ix}	2.662 (6)
Au4—Ga5	2.610 (16)	Ga8—Ga6^{ix}	2.739 (6)
Au4—Ga5^{xxv}	2.635 (11)	Ga8—Au6^{ix}	2.739 (6)
Au4—Ga5^{xv}	2.635 (11)	Ga8—Ga6^{xxxii}	2.739 (6)
Au4—Au4^{vii}	2.640 (13)	Ga8—Au6^{xxxii}	2.739 (6)
Au4—Au5^{xv}	2.946 (7)	Ga8—Ga8^{xi}	2.955 (10)
Ga4—Ga5^{xxv}	2.253 (17)	Ga8—Ga8^{x}	2.955 (10)
Ga4—Ga5^{xv}	2.253 (17)	Ga8—Ba2^{ix}	3.631 (3)
Ga4—Ga4^{vii}	2.37 (4)		

$BaAu_{3.58}Ga_{8.42}$

Ba1—Au1^{i}	3.619 (3)	Au3—Ga5^{xvii}	2.32 (8)
Ba1—Au1^{ii}	3.619 (3)	Au3—Au5^{xvii}	2.32 (8)
Ba1—Au1^{iii}	3.619 (3)	Au3—Ga5^{xviii}	2.32 (8)
Ba1—Au1^{iv}	3.619 (3)	Au3—Au5^{xviii}	2.32 (8)
Ba1—Au1^{v}	3.619 (3)	Au3—Ga2^{viii}	2.53 (4)
Ba1—Au1^{vi}	3.619 (3)	Au3—Au2^{viii}	2.53 (4)

Ba1—Au1^{vii}	3.619 (3)	Au3—Au4	2.60 (12)
Ba1—Au1	3.620 (3)	Au3—Ga4^{xviii}	2.71 (7)
Ba1—Ga7^{v}	3.634 (4)	Au3—Au4^{xviii}	2.71 (7)
Ba1—Ga7	3.634 (4)	Au4—Au5	1.008 (19)
Ba1—Ga7^{vi}	3.634 (4)	Au4—Ga3^{xix}	2.71 (7)
Ba1—Ga7^{i}	3.634 (4)	Au4—Au3^{xix}	2.71 (7)
Ba2—Au5	3.534 (8)	Au4—Ga3^{xii}	2.71 (7)
Ba2—Ga5^{viii}	3.534 (8)	Au4—Au3^{xii}	2.71 (7)
Ba2—Ga5^{ix}	3.534 (8)	Au4—Ga5^{viii}	2.74 (3)
Ba2—Au5^{viii}	3.534 (8)	Au4—Au5^{viii}	2.74 (3)
Ba2—Au5^{ix}	3.534 (8)	Au5—Ga5^{viii}	1.79 (5)
Ba2—Ga5^{x}	3.534 (8)	Au5—Au5^{viii}	1.79 (5)
Ba2—Au5^{x}	3.534 (8)	Au5—Ga3^{xii}	2.32 (8)
Ba2—Ga5^{xi}	3.534 (8)	Au5—Au3^{xii}	2.32 (8)
Ba2—Ga5^{xii}	3.534 (8)	Au5—Ga3^{xix}	2.32 (8)
Ba2—Au5^{xi}	3.534 (8)	Au5—Au3^{xix}	2.32 (8)
Ba2—Au5^{xii}	3.534 (8)	Au5—Au2^{xii}	2.66 (3)
Au1—Ga7^{xiii}	2.621 (4)	Au5—Ga2^{xii}	2.66 (3)
Au1—Ga7^{iii}	2.621 (4)	Au6—Ga2^{x}	2.54 (3)
Au1—Ga7	2.643 (6)	Au6—Au2^{x}	2.54 (3)
Au1—Ga7^{ii}	2.678 (6)	Au6—Ga6^{vii}	2.575 (5)
Au1—Ga6^{iv}	2.773 (4)	Au6—Au6^{vii}	2.575 (5)
Au1—Au6^{iv}	2.773 (4)	Au6—Ga6^{iv}	2.575 (5)
Au1—Ga6^{xiv}	2.773 (4)	Au6—Au6^{iv}	2.575 (5)
Au1—Au6^{xiv}	2.773 (4)	Au6—Ga7^{ii}	2.727 (6)
Au1—Ga6^{xv}	2.943 (4)	Au6—Ga4^{xx}	2.740 (6)
Au1—Au6^{xv}	2.943 (4)	Au6—Au4^{xx}	2.740 (6)
Au1—Au6	2.943 (4)	Au6—Au3^{x}	2.74 (4)
Au2—Au4	2.14 (4)	Au6—Ga3^{x}	2.74 (4)
Au2—Ga3^{viii}	2.53 (4)	Au6—Au1^{vii}	2.773 (4)
Au2—Au3^{viii}	2.53 (4)	Ga7—Au1^{xiii}	2.621 (4)
Au2—Ga6^{xvi}	2.54 (3)	Ga7—Au1^{iii}	2.621 (4)
Au2—Au6^{xvi}	2.54 (3)	Ga7—Au1^{ii}	2.678 (6)
Au2—Ga6^{x}	2.54 (3)	Ga7—Ga6^{ii}	2.727 (6)
Au2—Au6^{x}	2.54 (3)	Ga7—Au6^{ii}	2.727 (6)
Au2—Au5	2.54 (3)	Ga7—Ga6^{xxi}	2.727 (6)

Au2—Ga5^{xvii}	2.66 (3)	Ga7—Au6^{xxi}	2.727 (6)
Au2—Au5^{xvii}	2.66 (3)	Ga7—Ga7^{iii}	2.941 (10)
Au3—Ga3^{viii}	2.32 (7)	Ga7—Ga7^{xiii}	2.941 (10)
Au3—Au3^{viii}	2.32 (7)	Ga7—Ga7^{xxii}	3.003 (11)

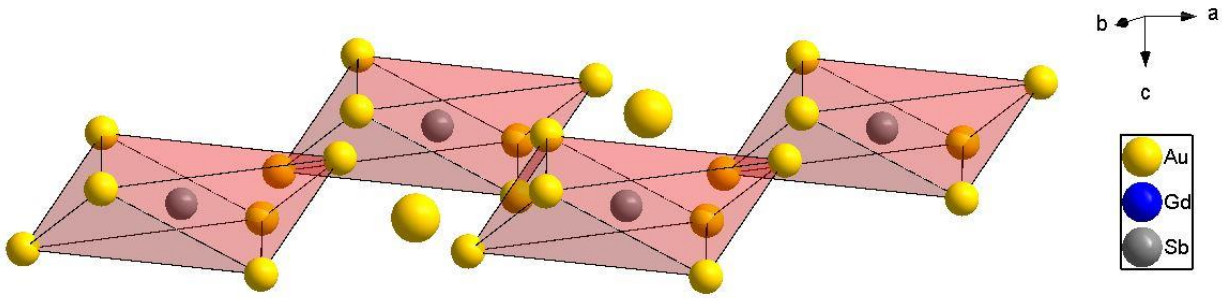

Figure A1. View of the isolated Sb@Au_6 trigonal prisms in Gd_3Au_9Sb. The unbound (slightly larger for differentiation) Au atoms represent the caps of the Au@Au_8 clusters in neighboring layers.

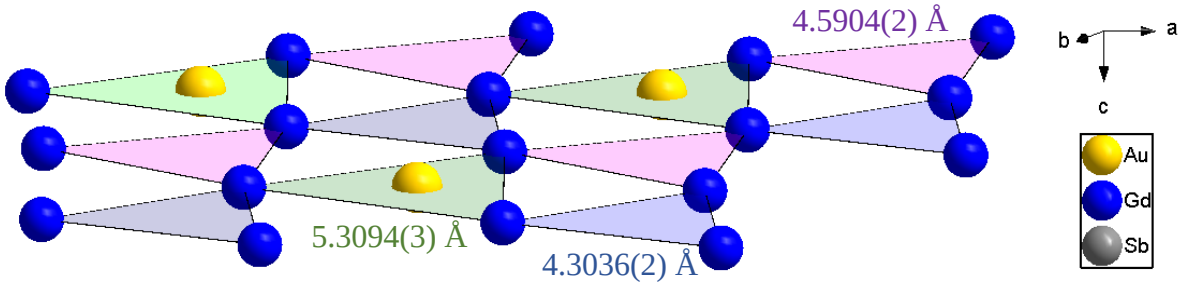

Figure A2. A view of the Gd trigonal planes in Gd_3Au_9Sb and interatomic atomic distances within each triangle. The green planes are centered by the central atom of the Au@Au_8 clusters.

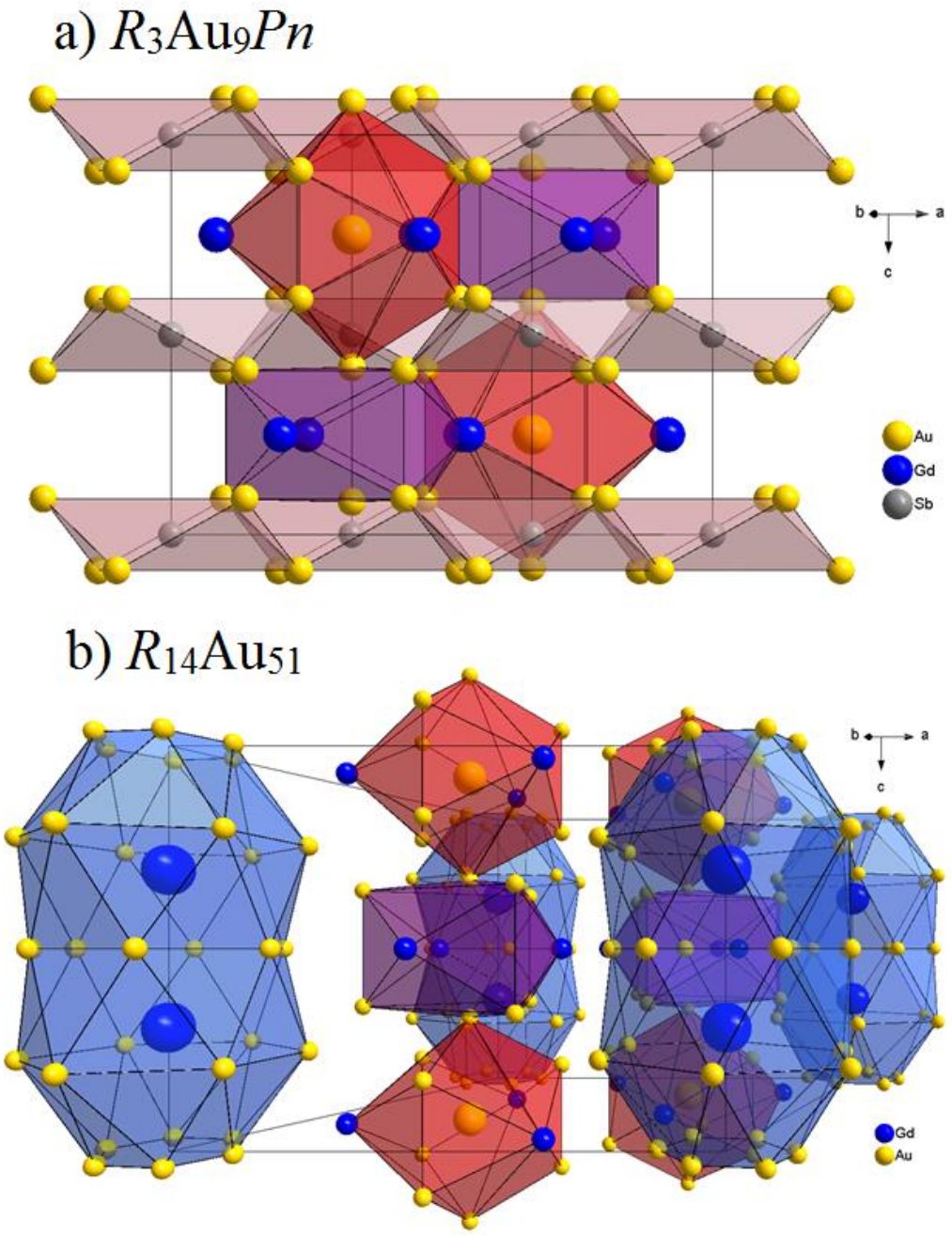

Figure A3. Comparison of coordination polyhedral observed in R_3Au_9Pn (a) and $R_{14}Au_{51}$ (b). The red and purple polyhedra appear isostructural and are not present in the $R_3Au_7Sn_3$ structure, demonstrating a previously unrecognized relationship between $R_{14}Au_{51}$ and $Cu_{10}Sn_3$ type structures.

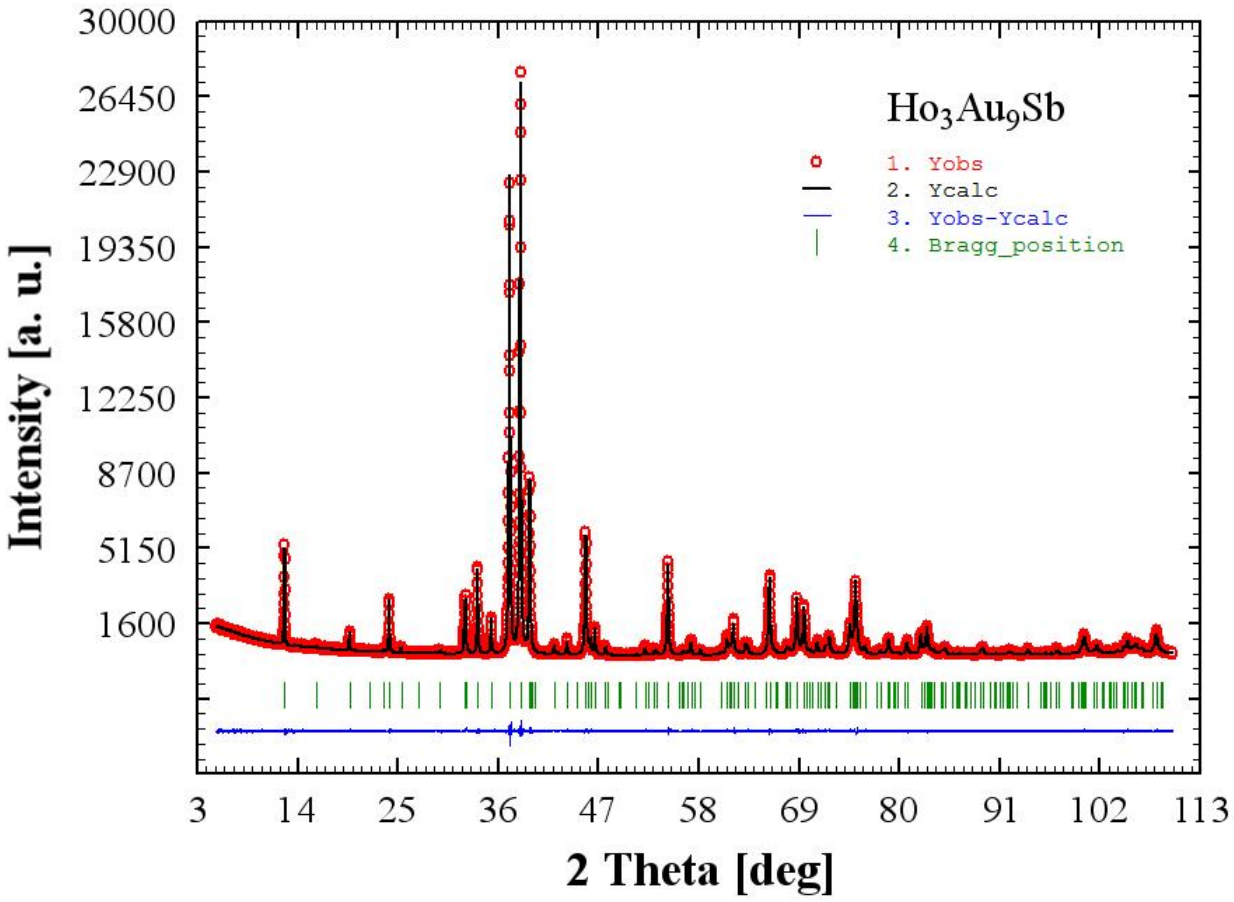

Figure A4: PXRD pattern of single phase Ho_3Au_9Sb used for magnetic testing.

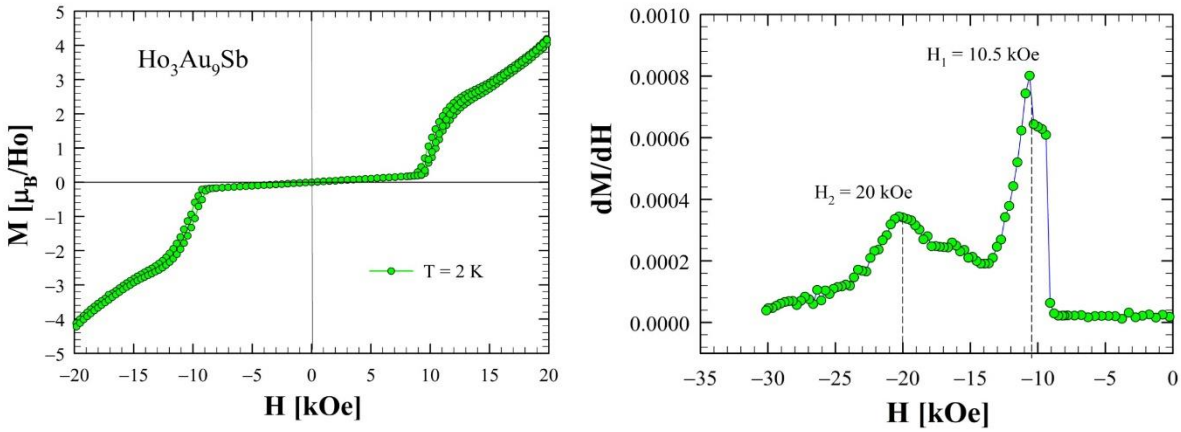

Figure A5. (left) A magnification of the isothermal magnetization in between ± 20 kOe showing magnetic hysteresis after the AFM region. (right) The derivative of the same isothermal magnetization curve showing peak positions used for determination of critical field values.

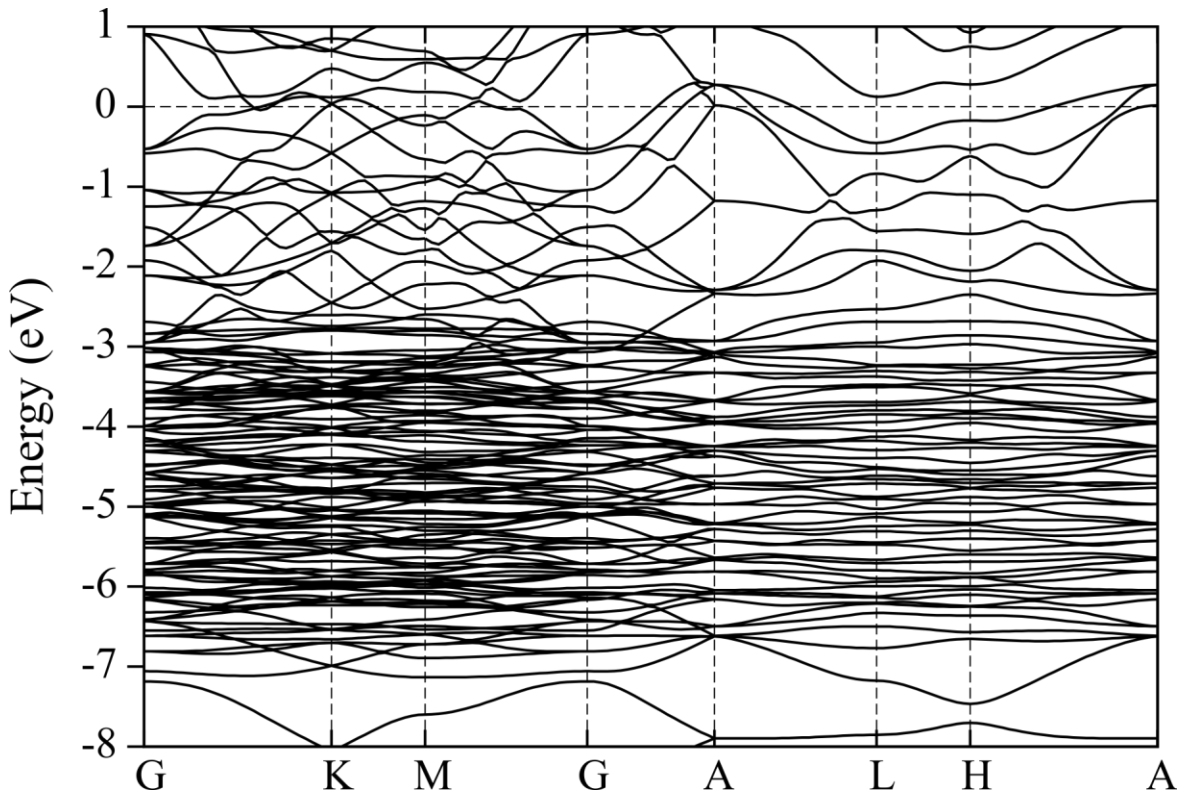

Figure A6. Band structure plot for Y_3Au_9Sb.

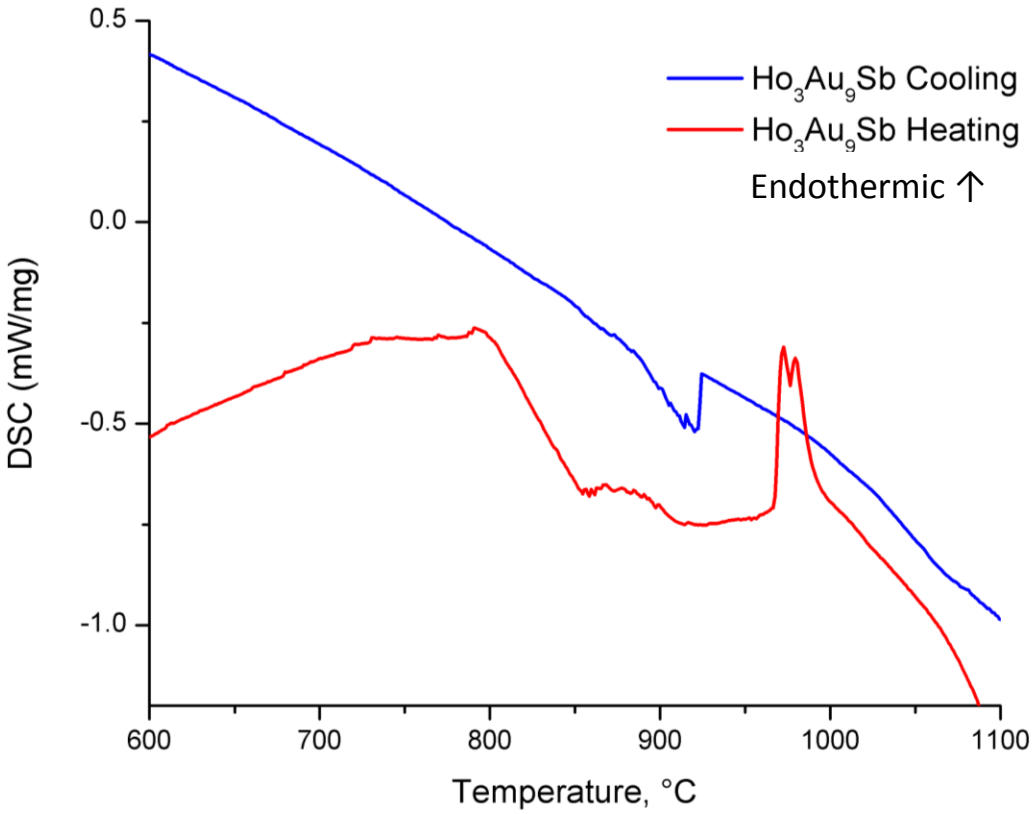

Figure A7. DSC plot for the Ho_3Au_9Sb sample recorded on heating and cooling at 20°C/min for both measurements.

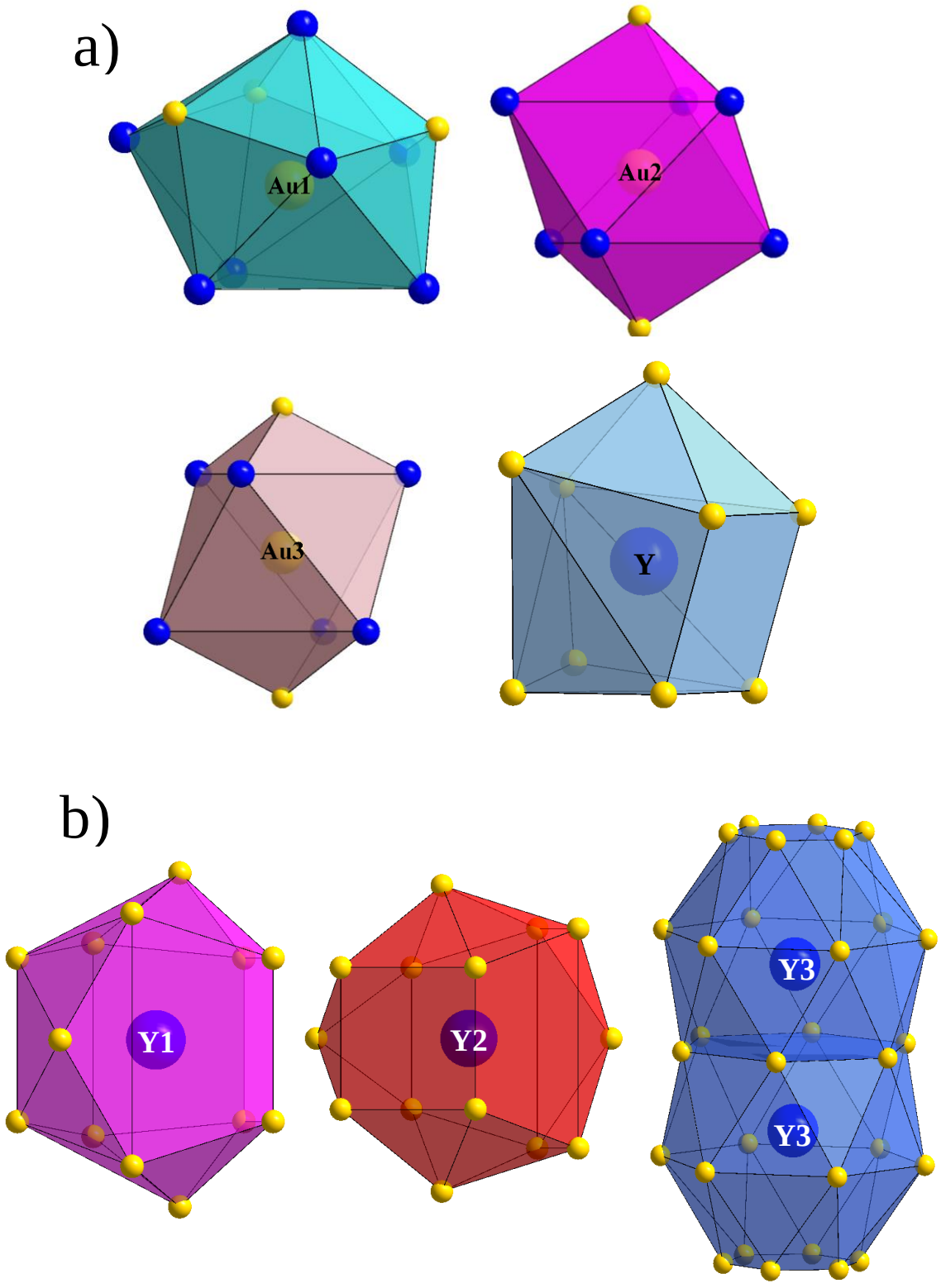

Figure A8. The coordination polyhedra for all crystallographic sites in Y_3Au_4 (a) as well as the coordination polyhedra for the Y sites in $Y_{14}Au_{51}$ (b).

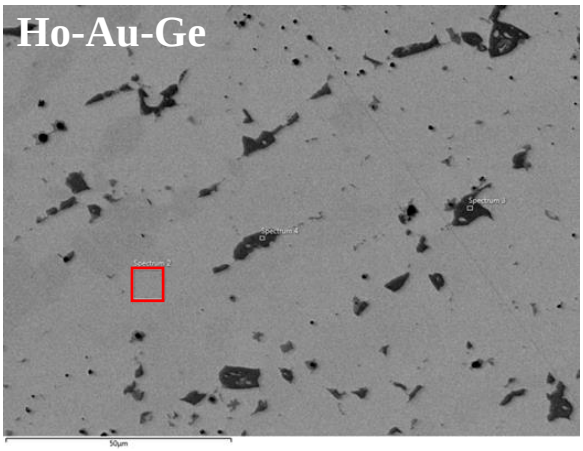
Ho-Au-Ge

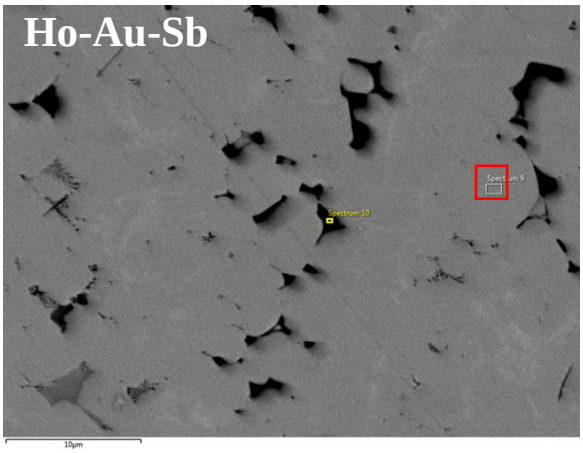
Ho-Au-Sb

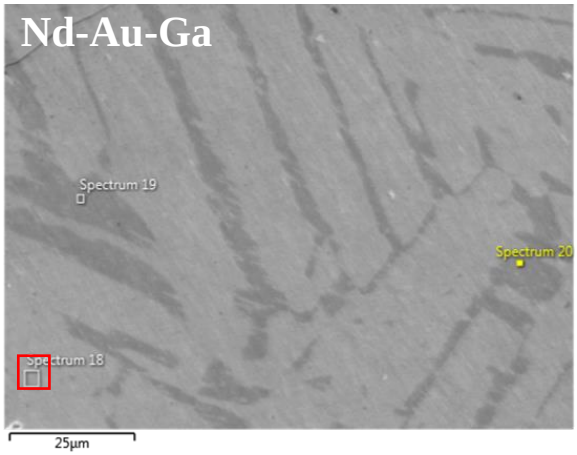
Nd-Au-Ga
Spectrum 19
Spectrum 20
Spectrum 18
25µm

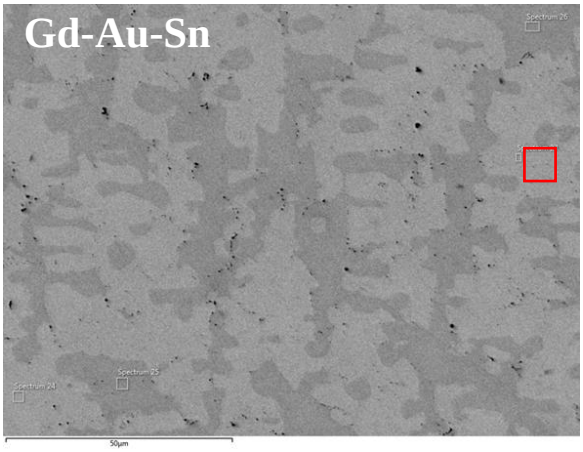
Gd-Au-Sn

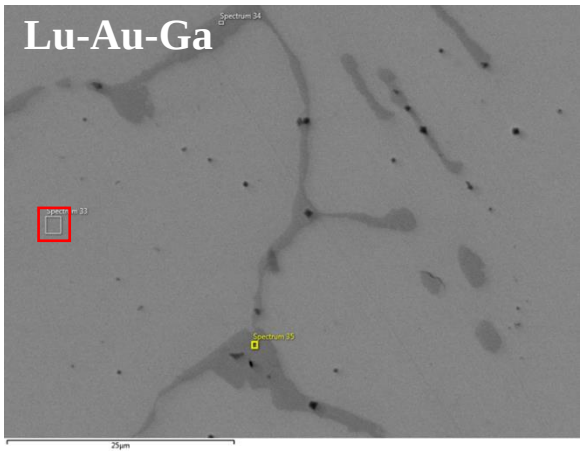
Lu-Au-Ga

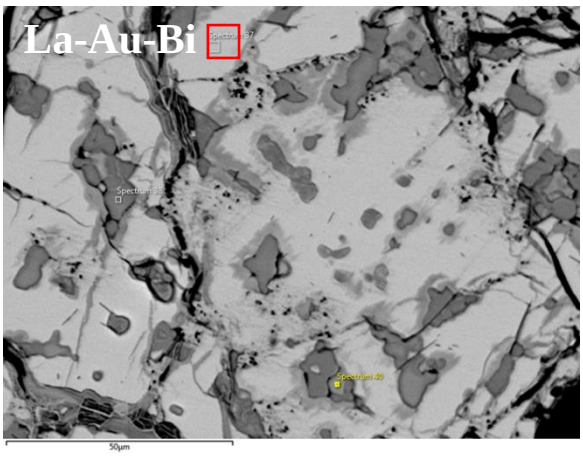
La-Au-Bi

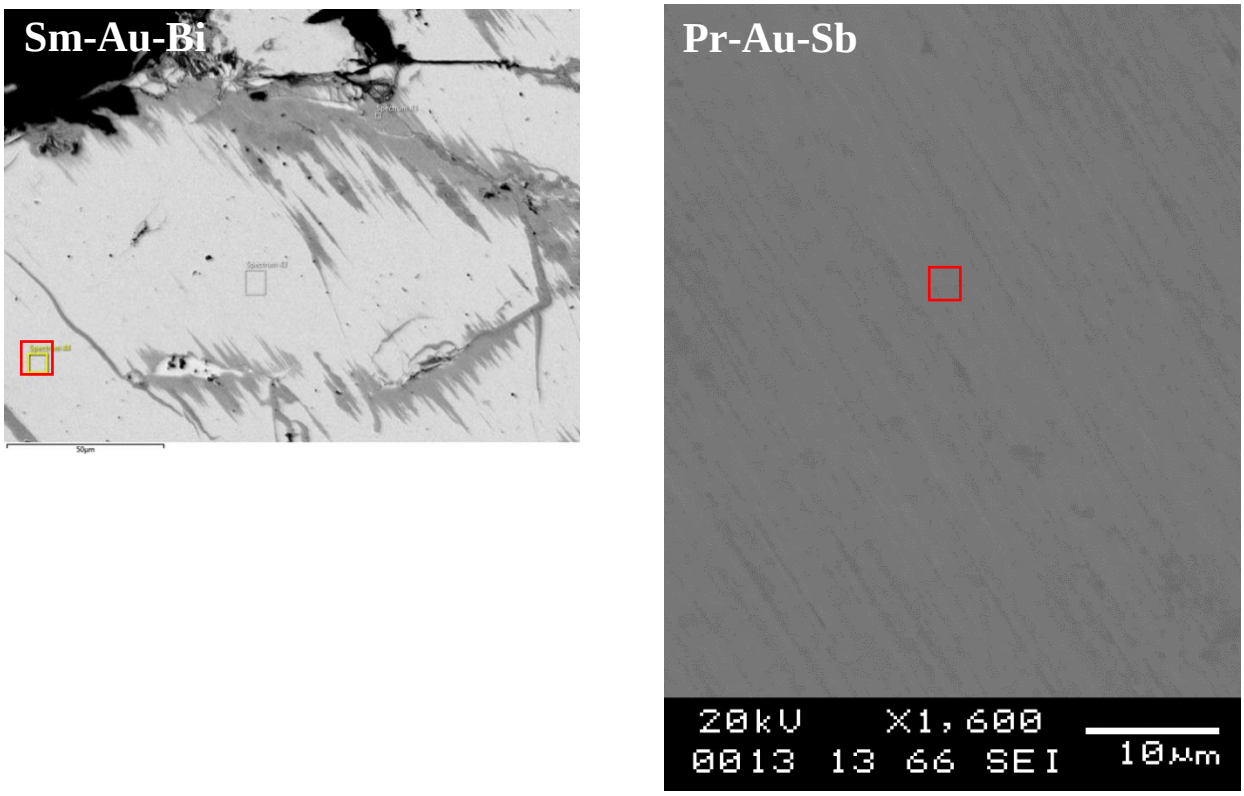

Figure A9. SEM micrographs of various samples used for EDS analysis. Regions used for EDS data from Table A4 are outlined in red for each sample.

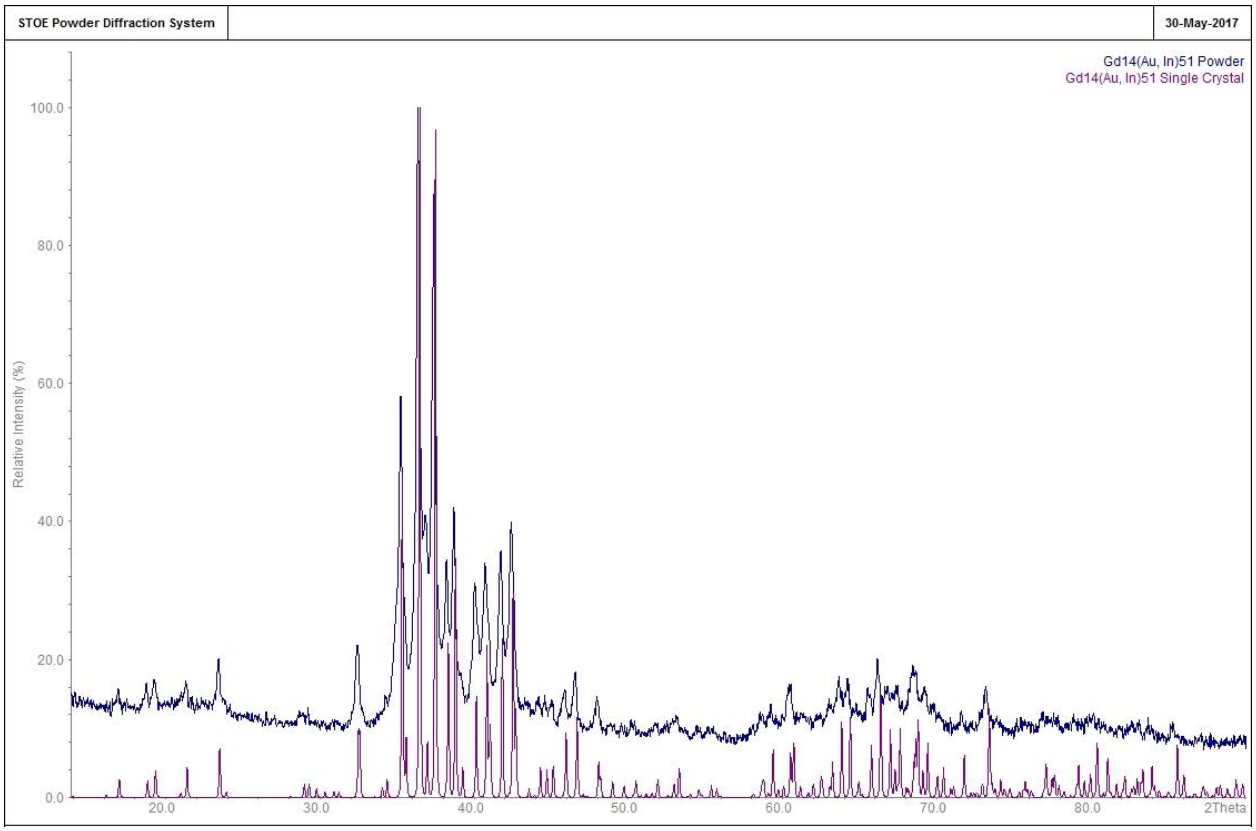

Figure A10. Comparison of powder X-ray diffraction data and theoretical peaks from corresponding single crystal X-ray diffraction data from Gd-Au-In sample.

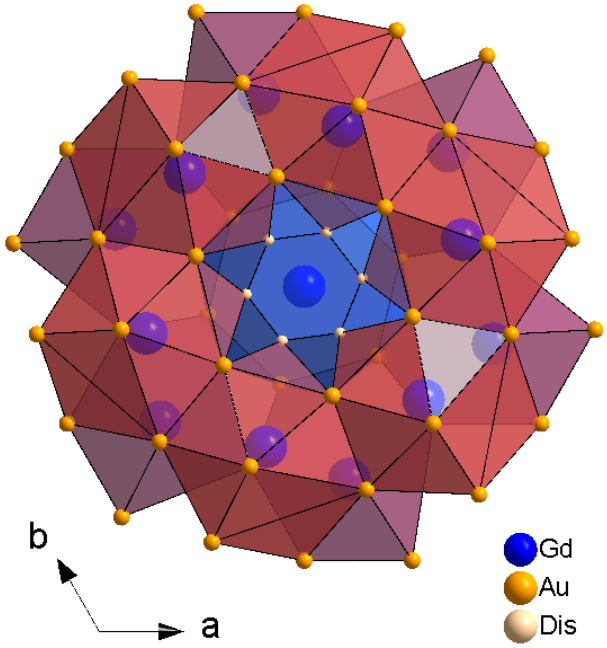

Figure A11. Alternate perspective of rare earth coordination polyhedra stacking scheme showing polyhedral “wheels” of the slab layers surrounding the columns of face-sharing double R2 coordination polyhedra.

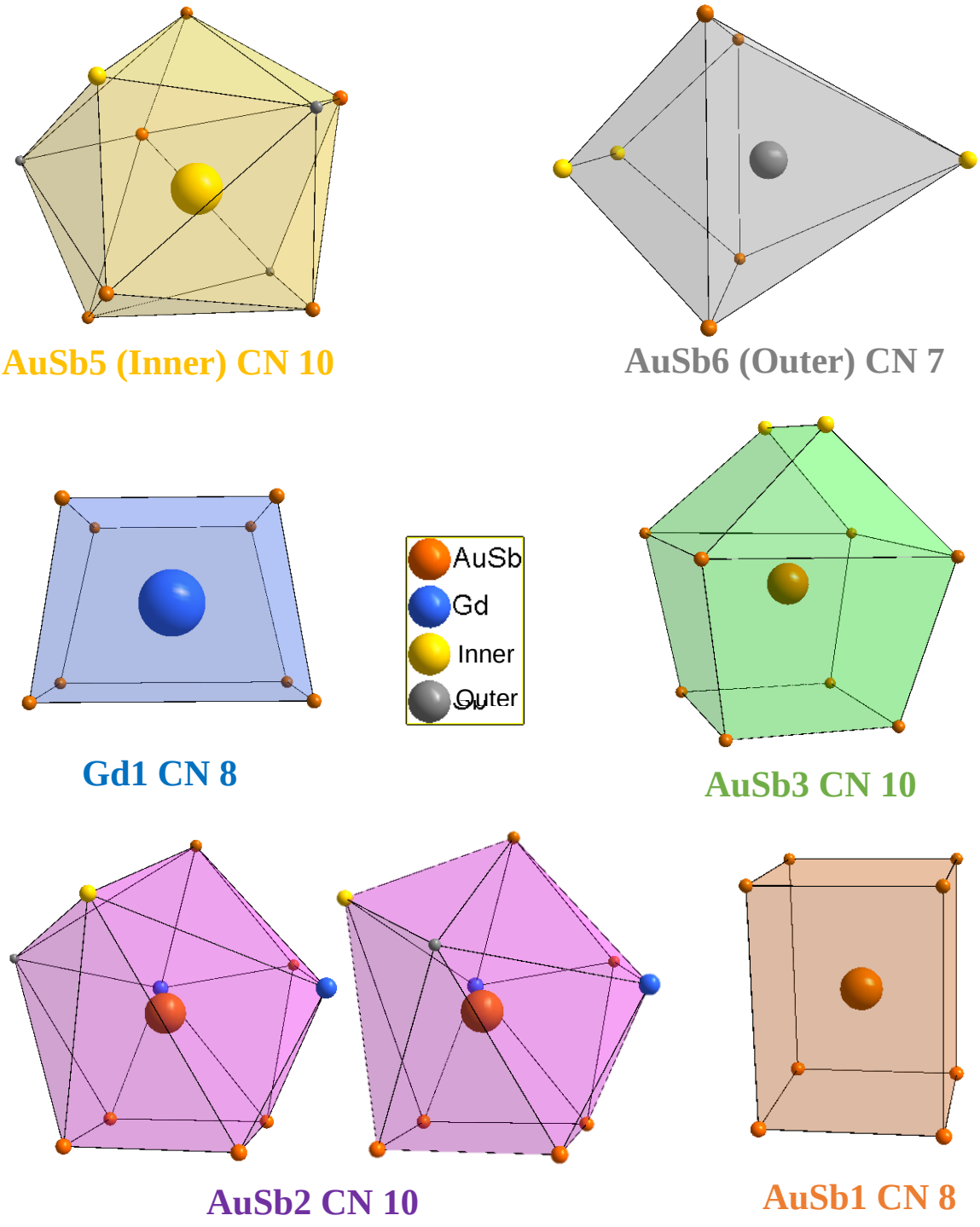

Figure A12. Coordination polyhedra for each site are illustrated above. For clarity, disordered positions that would be too close to the central atom to also be occupied have been removed from the top two polyhedra. The AuSb2 polyhedra form enantiomorphs depending on the inner and outer site fillings.

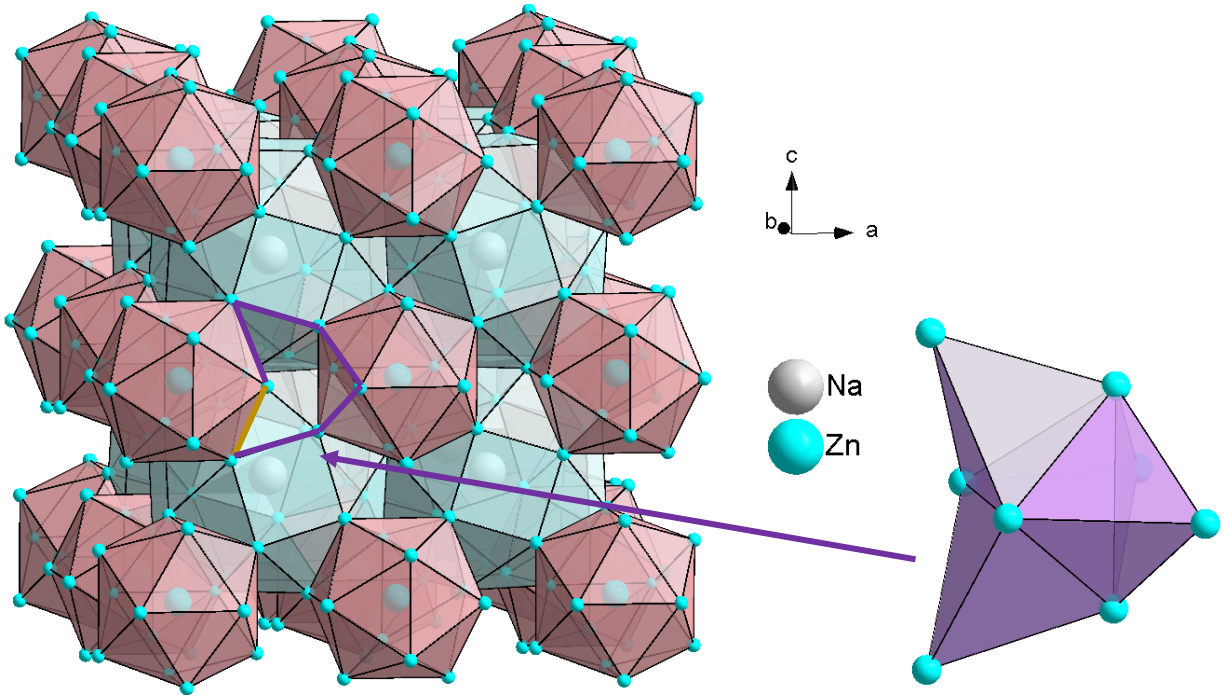

Figure A13. Polyhedral representation of $NaZn_{13}$ structure. Na-centered snub cubes are surrounded by Zn-filled icosahedra, and tetrahedral stars (outlined and pulled aside for clarity).

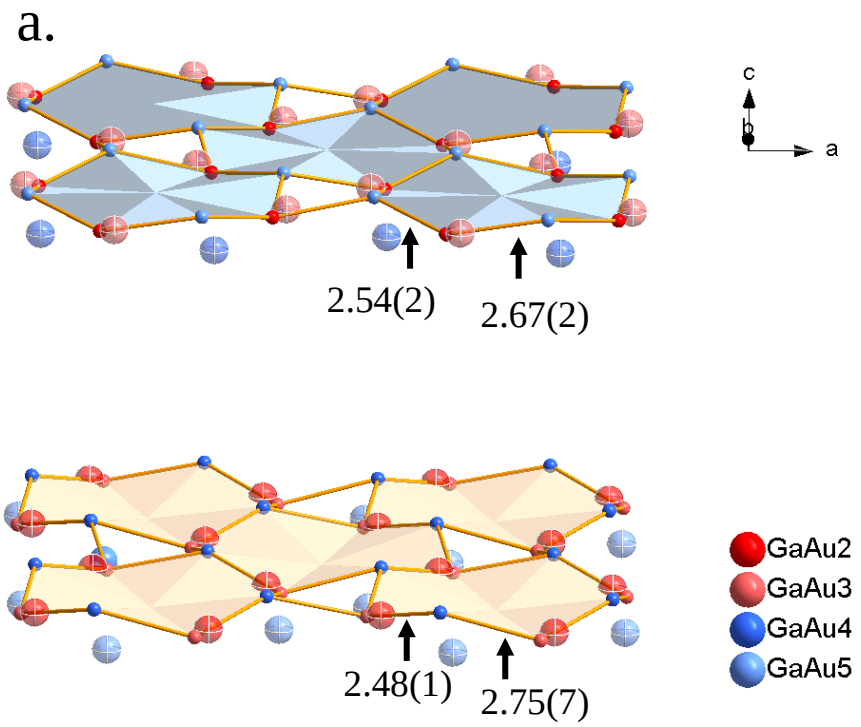

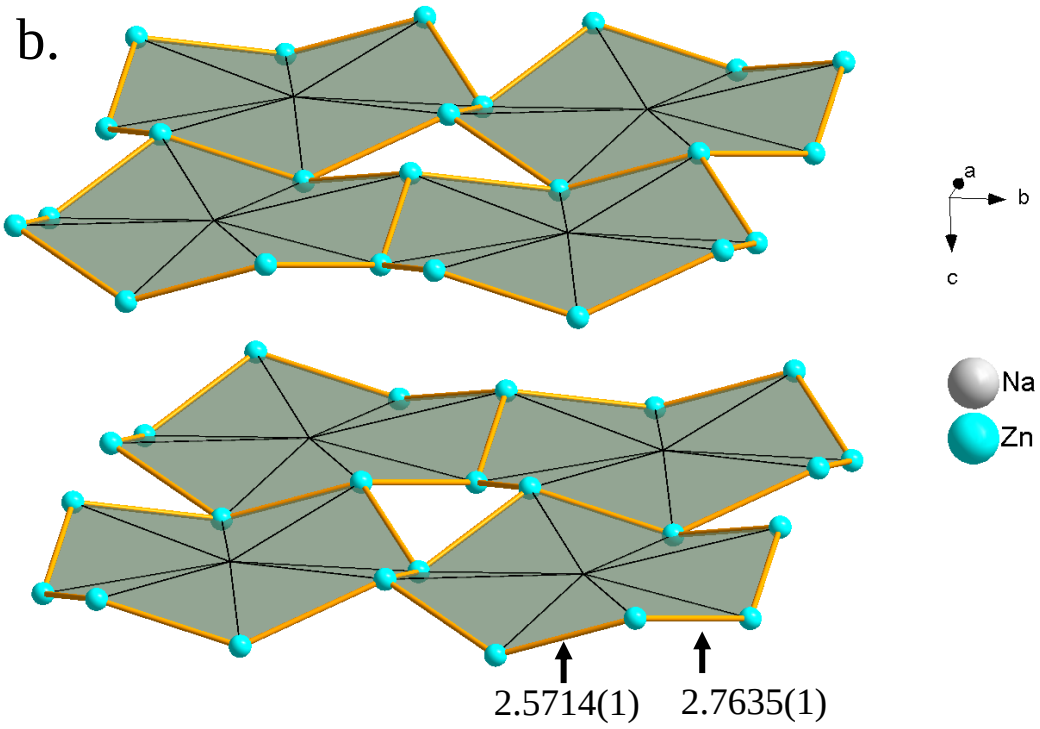

Figure A14. Octagonal nets in $BaAu_xGa_{12-x}$ (*a.*) and $NaZn_{13}$ (*b.*) with atomic distances labeled to show distortion within the layers. The disordered nets made up of (GaAu)2 and (GaAu)5 sites, and (GaAu)3 and (GaAu)4 sites are less and more distorted (respectively) than the nets in $NaZn_{13}$.